NOVEL ADSORBENT SYNTHESIS, DIFFUSION IN NANOPOROUS MATERIALS, AND ADSORPTION SYSTEM OPTIMIZATION

By

Thomas Grant Glover

Dissertation
Submitted to the Faculty of the
Graduate School of Vanderbilt University
in partial fulfillment of the requirements
for the degree of

DOCTOR OF PHILOSOPHY

in

Chemical Engineering

May, 2008
Nashville, Tennessee

Approved:

Professor M. Douglas LeVan

Professor Kenneth A. Debelak

Professor G. Kane Jennings

Professor Scott A. Guelcher

Professor Eugene J. LeBoeuf

NOVEL ADSORBENT SYNTHESIS, DIFFUSION IN NANOPOROUS MATERIALS, AND ADSORPTION SYSTEM OPTIMIZATION

THOMAS GRANT GLOVER

Dissertation under the direction of M. Douglas LeVan

This research focuses three specific topics related to gas-phase adsorption: the synthesis and characterization of a novel carbon-silica composite adsorbent material, the diffusion of condensable vapors in single adsorbent particles, and an examination of pulse inputs and layered-bed optimization.

The first segment of the work details the synthesis of a carbon-silica composite (CSC) adsorbent derived from MCM-41 and polyfurfuryl alcohol. The novel material has a high surface area, and a narrow pore size distribution. Materials were also prepared using different furfuryl alcohol solvents and were polymerized and carbonized at different pressures. The surface area of the materials is affected by both solvent selection and the pressure at which carbonization takes place. The novel material is unique because the carbon pores are created from templating rather than from an activation process.

The next segment extends a concentration-swing frequency response method to examine mass transfer rates and concentration dependence for adsorption of condensable vapors in adsorbent particles. The adsorption kinetics of water and hexane in BPL activated carbon and the adsorption of water in silica gel are determined at several different concentrations. The mechanism that best describes the adsorption of water in BPL activated carbon is nanopore diffusion, and both models can be used to describe the diffusion of hexane in BPL activated carbon. The diffusion of water in silica gel is best characterized by the Glueckauf linear driving force model.

In the final segment of this work a mathematical model is developed to examine the sensitivity of fixed beds with respect to system parameters. The impact of mass and energy transfer effects and adsorbent layer thicknesses are determined by calculating the derivatives of the outlet concentration and outlet temperature. The adsorption of hexane on BPL activated carbon is contrasted with the adsorption of nitrogen on carbon molecular sieve, and combined mass and energy effects are considered by studying the adsorption of nitrogen on BPL activated carbon. The sensitivity data are then applied to determine the optimum bed layering of a two-layer, two-bed PSA system.

To Betsy

ACKNOWLEDGEMENTS

I would first like to acknowledge my advisor Professor M. Douglas LeVan. It is only with his patience and guidance that I have been able to complete this process, and I am grateful for all of the opportunities that he has provided me. Through his actions he has shown me how research should be done, and it has been a privilege to study under his guidance.

I am also grateful to the many professors who have assisted me in my studies. These include the members of my committee Professors Kane Jennings, Scott Guelcher, Ken Debelak, and Gene LeBoeuf, as well as Professor Charles Lukehart for his assistance with the X-ray diffractometer.

I would like to graciously acknowledge Vanderbilt University and the U.S. Army Edgewood Chemical and Biological Center for funding this research. I would like to thank Chris Karwacki, Leonard Buettner, Tara Sewell, Greg Peterson, and John Mahle for their recommendations and suggestions. I appreciate the opportunity they have afforded me to learn about the applications of my research, and I have thoroughly enjoyed talking with the ECBC team. I would also like to thank David Friday of Hunter Manufacturing Company for many beneficial discussions about adsorption research.

The staff of Vanderbilt University also deserves to be recognized for their contributions to this work. I would like to thank Mark Holmes for his assistance in the laboratory, Robin Midgett for the use of his hand truck and the wiring of laboratory equipment, and Mary Gilleran for her assistance. I would also like to thank Margarita Talavera for many enjoyable discussions and for her advice.

I wish thank the LeVan research group for their assistance. In particular I would like to thank Krista Walton for her assistance at the beginning of my work, Yu Wang for her patience with my questions regarding frequency response, Bryan

Schindler for helping me in the laboratory, answering questions about Fortran, discussing research problems, and providing excellent company during the course of my studies. I would also like to acknowledge Joe Moate, Jian Liu, and Amanda Furtado for many research oriented discussions.

It is also necessary that I acknowledge my family for supporting me during this process. I will be forever grateful to my parents who showed me that with continual hard work and high expectations I can accomplish any goal. I would like to thank my dad for working a seemingly endless number of math homework problems in grade school and my mom for teaching me to always strive for my personal best. I would also like to acknowledge my brother Bryan for showing me what is possible when dreams of space exploration are coupled with scientific curiosity.

I would also like to acknowledge Wayne Abts for teaching me how to keep cars running even when everyone around you says they cannot be fixed, thanks Wayne. I would also like to acknowledge Joannie Morrison for the wonderful family memories and the numerous things she has done to make this possible. To all of Betsy's families I am thankful.

Finally, none of this would be possible with out the continual support of my wife Betsy. There is no reasonable way I can describe how she has helped me over the last few years. She is my strength, motivation, and encouragement and I will be forever grateful for her help.

TABLE OF CONTENTS

LIST OF TABLES

LIST OF FIGURES

CHAPTER I

INTRODUCTION

Separations often account for a major portion of production costs in chemical industries. For adsorption, the quality of the separation is directly related to the thermodynamics and kinetics of the process. Thus, in order to make efficient use of adsorption as a separations tool it is necessary to understand not only the operation of adsorption systems, but also how equilibrium and mass transport interact with the adsorbent on a fundamental level.

There are several examples in industry that illustrate various types of separations that are possible with a proper understanding of the design adsorption systems. Examples include the separation of air using zeolites or carbon molecular sieves, and the recovery of hydrogen from streams containing CO, CH_4, and CO_2 by using activated carbons and different zeolite layers.[1]

While the list of current applications of adsorption is extensive, Yang[1] states that future applications of adsorption are limited by the availability of new and better sorbents. The development of LiX zeolite provides an illustration of the necessity to develop novel adsorbent materials. Prior to LiX, air separation was performed using NaX and 5A zeolites; however, with the advent of LiX the production of oxygen from air was increased 1.4–2.7 times and power consumption was reduced up to 27 percent.[1] Thus, continued research into novel materials is important because they have the potential to increase the efficiency of current separation devices and present solutions to separations and filtration problems that cannot be addressed by current adsorption technology.

Frequently, during the design of adsorption systems the selection of the adsorbent material is motivated by its equilibrium capacity, while the kinetics of the adsorption process are considered secondary to the isotherm.[1] However, if the selected material has slow kinetics it may not be useful in industrial adsorption systems. For example, carbogenic molecular sieves developed by Foley *et al.*[2] adsorb several different gases such as CO_2 and C_4H_{10}, but the total capacity of the material is rarely reached because several hours are required to allow the gas to diffuse into the material. On the other hand, carbogenic molecular sieves can be applied as a separations device because the narrow pore size of the material limits the adsorption of large molecules. Therefore, it is necessary to consider the kinetics of an adsorbent material in concert with its equilibrium capacity when selecting a material for adsorption systems.

In addition to selecting the proper adsorbent, gains in the efficiency of an adsorption separation can also be acquired by developing an efficient adsorption cycle. Of particular interest is the utilization of multilayered adsorbent beds which allow the adsorbent system to target materials in the feed stream at different times during the separation process. For example, the separation of CH_4 from a feed stream of N_2 and CO_2 has been investigated by using a layered bed of 13X zeolite and a carbon molecular sieve.[3–7] In this example, the CO_2 can be removed by the layer of 13X zeolite, and CH_4 and N_2 can be separated kinetically with the carbon molecular sieve. Thus, understanding how the bed should be layered is critical to designing an effective separation process.

Building on the ideas presented above, this research explores several key aspects of adsorption systems including novel nanoporous materials design, adsorption kinetics, and adsorption system optimization. In the first section of the work, the synthesis of a novel nanoporous adsorbent material is discussed. The foundation for the material is MCM-41, a novel mesoporous silica that has attracted considerable attention in research literature.[8–11] The novel carbon-silica composite material discussed in this work is templated from MCM-41 by impregnating the silica framework with furfuryl alcohol. The first segment of this work details the synthesis and characterization of our novel carbon-silica composite material. The work is further extended in a subsequent chapter that details the sensitivity of the material to various processing conditions including furfuryl alcohol solvent selection and carbonization pressure. This work is distinctive as it approaches the synthesis of a carbon adsorbent via a nanoscale assembly mechanism and not by a chemical or physical activation.

The second section of research, while fundamental, moves away from novel nanoporous material synthesis and examines mass transport behavior in single adsorbent particles. Understanding the interaction of condensable vapors, and in particular water and organics, with adsorbents is of vital importance in adsorption beds used for solvent recovery, air purification, and protective filters found in buildings and gas masks. Recently, FR has been applied to several different systems to characterize the diffusion of gas in nanoporous adsorbents.[13–20] In this study, a concentration-swing frequency response apparatus is used to investigate the diffusion of water and hexane in BPL activated carbon and the diffusion water in silica gel. In each case, the mass transport mechanism is identified, and the applicability of the Darken relationship is evaluated.

Finally, the third segment of the research explores the design of adsorption systems. In order to design efficient adsorption systems, it is necessary to understand what physical parameters, such as mass and energy transport coefficients, particle sizes, adsorbent layer thicknesses, feed temperature and pressure, govern the system behavior. Using sensitivity analysis to explore these concerns provides a fundamental understanding of the adsorption system which, in turn, yields a computationally efficient adsorption model. In this work, a model has been developed that examines the sensitivity of a fixed bed adsorption process with respect to various mass and energy transport parameters. The model is applied first to an example that considers the adsorption of a low concentration pulse of hexane on activated carbon. These results are then contrasted with an example that details the adsorption of nitrogen on carbon molecular sieve, and finally joint mass and energy effects are considered by examining the adsorption of a pulse of nitrogen in BPL activated carbon. The model is then applied to optimize a layered pressure swing adsorption system by determining the appropriate layer thicknesses.

The last segment of this work provides a summary of the key findings of each chapter, and provides a brief discussion of future work that could stem from these results.

References

[1] Yang R.T., Adsorbents Fundamentals and Applications, John Wiley & Sons, Hoboken, 2003.

[2] Foley H.C., Carbogenic molecular sieves: Synthesis, properties and applications. *Micro. Mater.* 1995, 4, 407-433.

[3] Cavenati S., Grande C.A., Rodrigues A.E., Separation of $CH_4/CO_2/N_2$ mixtures by layered pressure swing adsorption for upgrade of natural gas. *Ind. Eng. Chem. Res.* 2006, 61, 3893-3906.

[4] Cavenati S., Grande C. A., Rodrigues A. E., Layered Pressure Swing Adsorption for Methane Recovery from $CH_4/CO_2/N_2$ Streams. *Adsorption* 2005, 11, 549-554.

[5] Cavenati S., Grande C. A., Rodrigues A. E., Upgrade of Methane from Landfill Gas by Pressure Swing Adsorption. *Energy and Fuels* 2005, 19, 2545-2555.

[6] Cavenati S., Grande C. A., Rodrigues A. E., Adsorption Equilibrium of Methane, Carbon Dioxide, and Nitrogen on Zeolite 13X at High Pressures. *J. Chem. Eng. Data* 2004, 49, 1095-1101.

[7] Cavenati S., Grande C. A., Rodrigues A. E., Separation of Methane and Nitrogen by Adsorption on Carbon Molecular Sieve. *Sep. Sci. and Tech.* 2005, 40, 2721-2743.

[8] Kresge C.T, Leonowicz M.E., Roth, W.J., Vartuli J.C., and Beck J.S., Ordered Mesoporous Molecular-Sieves Synthesized by a Liquid-Crystal Template Mechanism. *Nature* 1992, 359, 710-712.

[9] Beck J.S., Vartuli J.C., Roth, W.J., Leonowicz M.E., Kresge C.T, Schmitt K.D., Chu C.T-W, Olson D.H., Sheppard E.W., McCullen S.B., Higgins J.B. and

Schlenker J.L., A New Family of Mesoporous Molecular Sieves Prepared with Liquid Crystal Templates. *J. Am. Chem. Soc.* 1992, 114, 10834-10843.

[10] Ciesla U., Schuth F., Ordered mesoporous materials. *Micro. Meso. Mater.* 27, 1999, 131-149.

[11] Sakintuna B., and Yurum Y., Templated Porous Carbons: A Review Article. *Ind. Eng. Chem. Res.* 2005, 44, 2893-2902.

[12] Marlin T.E., Process Control Designing Processes and Control Systems for Dynamic Performance, 2nd ed. McGraw-Hill, Boston, 2000.

[13] Yu Wang, PhD Thesis, Vanderbilt University, 2005.

[14] Brian Kenneth Sward, PhD Thesis, University of Virginia, 2001.

[15] Sward B.K., LeVan M.D., Frequency response method for measuring mass transfer rates in adsorbents via pressure perturbation. *Adsorption*

[16] Wang Y., LeVan M.D., Investigation of mixture diffusion in nanoporous adsorbents via the pressure-swing frequency response method. 1. Theoretical treatment. *Ind. Eng. Chem. Res.* 2005, 44, 3692-3701.

[17] Wang Y., LeVan M.D., Investigation of mixture diffusion in nanoporous adsorbents via the pressure-swing frequency response method. 2. Oxygen and nitrogen in a carbon molecular sieve. *Ind. Eng. Chem. Res.* 2005, 44, 4745-4752.

[18] Wang Y., LeVan M.D., New developments in flow-through apparatus for measurement of adsorption mass-transfer rates by frequency response method. *Adsorption* 2005, 11, 409-414.

[19] Wang Y., Sward B.K., LeVan M.D., New frequency response method for measuring adsorption rates via pressure modulation: Application to oxygen and nitrogen in carbon molecular sieve. *Ind. Eng. Chem. Res.* 2003, 42, 4213-4222.

[20] Wang Y., LeVan M.D., Nanopore Diffusion Rates for Adsorption Determined by Pressure-Swing and Concentration-Swing Frequency Response and Comparison with Darken's Equation. *Ind. Eng. Chem. Res.*, in press.

CHAPTER II

CARBON-SILICA COMPOSITE ADSORBENT: CHARACTERIZATION AND ADSORPTION OF LIGHT GASES

2.1 Introduction

In 1992, Kresge *et al.*[1] published the first work on a family of mesoporous materials referred to as M41S. The work sparked a surge into the research of mesoporous materials. Beck *et al.*[2] in a related paper studied in more detail MCM-41, a member of the M41S family. These two papers have provided the foundation for the examination of mesoporous silicas and in particular MCM-41 for use as, among other things, a catalyst, adsorbent, and a molecular sieve.

Davis *et al.*[3,4] synthesized MCM-41 and examined the liquid crystal templating synthesis mechanism. They characterized their MCM-41 via X-ray diffraction (XRD), temperature-programmed XRD, infrared spectra, Raman spectra, thermogravimetric analysis (TGA), ^{14}N NMR, and N_2 measurements. The use of XRD and liquid N_2 adsorption are the most commonly used means to characterize MCM-41. Using ^{14}N NMR they found that randomly ordered rod-like micelles interact with silica to form micelle-supported silica rods. The micelle supported rods then assemble into the hexagonal order associated with MCM-41.

Reports have also been published on the optimum synthesis conditions required to produce high quality MCM-41. For example, Park *et al.*[5] performed a series of experiments to determine the optimum reaction gel composition for the preparation of MCM-41 and monitored the progression of the reaction by measuring the pH of the reaction gel. They concluded that the optimum molar ratios of the reagents in the reaction gel should be SiO_2:20 CTACl:0.18 TMAOH:25 H_2O.

Optimizing the long-range order of MCM-41 has also been examined in relation to the pH of the synthesis gel. The pH of the solution decreases as the reaction proceeds. Ryoo and Kim[6] found that the long range XRD order of the MCM-41 was increased by periodically titrating the reaction gel with acetic acid. Expanding on the work of Ryoo and Kim, Edler and White[7] determined that using H_2SO_4 and titrating to a pH of 9-10 provided a highly ordered MCM-41 material. Further papers examined the effects of acid-titrated MCM-41 preparations by examining the material's stability and wall structure.[8,9]

In addition to pH, studies have examined a wide variety of MCM-41 characteristics in relation to synthesis conditions. For example, Huo *et al.*[10] studied the relation between templating surfactants, synthesis conditions, and post synthesis treatments on the resulting silica mesophase. Other work has examined post synthesis treatments and organic swelling agents as a route to pore size expansion,[11–14] while others have focused on the quantification of the phase composition of MCM-41.[15] The evolution of MCM-41 material during the calcination process has been examined to determine how the micelle template is removed from MCM-41.[16] The aging, thermal, and hydrothermal stability of MCM-41 have been studied[17–20] and attempts have been made to improve the stability of MCM-41.[21]

Several other authors have characterized the pore structure of MCM-41. Zhu *et al.*[22] applied an extension of the micropore analysis method (MP method) and found results consistent with the dimensions obtained with XRD. Kruk *et al.*[23,24] have characterized a wide variety of different size MCM-41 materials via XRD and N_2 adsorption isotherms. During their investigation they found that by modifying the Kelvin equation and applying the Barrett-Joyner-Halenda (BJH)[25] method, accurate pore size distribution (PSD) predictions of MCM-41 materials could be determined.[11] The application of the BJH method with the modified Kelvin equation is frequently referred to as the Kruk-Jaroniec-Sayari or KJS method.[15] Choma *et al.*[26] compared the KJS method of determining the PSD of MCM-41 to BJH, Dollimore and Heal (DH), and Broekhoff and deBoer (BdB) methods. They found that the KJS method provides a reliable estimate of the pore size of mesoporous materials.

The ability to synthesize a controllable mesoporous silica material led to the use of the M41S materials as templates for the synthesis of mesoporous carbons. Sakintuna and Yurum[27] provide a review of templated porous carbons. In their review the synthesis of porous carbons is divided into five steps: (i) synthesis of the inorganic template, (ii) impregnation of the template with an organic template such as polyfurfuryl alcohol, phenol, formaldehyde, or acrylonitrile, (iii) polymerization of the precursor (iv) carbonization of the organic material, and (v) removal of the inorganic template.

Ryoo *et al.*[28] used MCM-48, another member of the mesoporous silica family M41S, as a silica support in the production a mesoporous carbon termed CMK-1. The material has two PSDs, one centered in the nanoporous region with pores ranging from 5-8 Å and one centered in the mesoporous region with pores near 30 Å.

Kruk *et al.*[29] also studied MCM-48 silica as a template for mesoporous carbons by synthesizing a variety of MCM-48 samples and impregnating them with sucrose in the presence of sulfuric acid. In order to provide a comparison, they also impregnated MCM-41 with sucrose and MCM-48 with polyfurfuryl alcohol. However, in order for the impregnation of MCM-48 with polyfurfuryl alcohol to take place it was necessary to convert the pure silica MCM-48 sample into an aluminosilicate via a postsynthesis alumination method.[30,31] They found that the templating of MCM-41 and MCM-48 showed that after the removal of the silica template CMK-1 retains long-range order and mesoporosity. The authors point out that upon the removal of the MCM-41 template the resulting carbon loses all long-range order and is completely nanoporous.

The work of Kruk *et al.*[29] is consistent with previous results published by Lee *et al.*,[32] which showed that after the removal of the MCM-41 silica template, the resulting carbon structure was nanoporous. The impregnation procedure of Lee *et al.* is different from the work of Kruk *et al.* Lee *et al.* first incorporate phenol inside the pores of MCM-41 and then statically heat the phenol MCM-41 composite in the presence of formaldehyde to polymerize the phenol and formaldehyde. The resulting carbon composite material is then heated under N_2 to carbonize the phenol resin. The predominant pore size of the carbon acquired after the removal of the silica template is 6 Å. The nanoporous nature of the resulting carbon is attributed to the carbonization of the phenol resin and not to an activation process occurring as a result of the carbon being contained inside the pores of MCM-41.[32] Kruk et al., however, state that the use of the MCM-41 template was responsible for the development of the adsorption properties of the nanoporous structure of the sucrose-based carbon.

Joo *et al.*[33] used SBA-15,[34] a mesoporous silica with hexagonal channels connected radially by various nanopores and mesopores, to synthesize the mesoporous carbon CMK-5. Unlike carbons templated from MCM-41, CMK-5 maintains its long range structural ordering after removal of the SBA-15 silica template.[35] Kruk *et al.*[36] used polyfurfuryl alcohol to impregnate an aluminated SBA-15 and formed CMK-5 by carbonizing the polymer under vacuum and CMK-3 by carbonizing the polymer under N_2. Various other carbon materials templated from silicas each with different molecular symmetry have been reported and their related papers have been briefly summarized by Kruk *et al.*[36] in their work on carbon nanopipes. Briefly, according to Kruk *et al.* , CMK-4[37] has been templated from FDU-5,[38,39] cubic carbon CMK-2[40] has been templated from SBA-1,[41] and CMK-3,[35,42] a carbon with hexagonal symmetry, has been synthesized from SBA-15.

The use of polyfurfuryl alcohol (PFA) in the production of nanocarbons and nanocomposites has been extensive. A review of progress in this area is available from Wang and Yao.[43] Some of the applications mentioned by Wang and Yao are the carbonization of PFA in the pores of Zeolite Y[44] and incorporation of PFA into lamellae of montmorillonite (MONT), taeniolite (TAEN), saponite (SAPO), and smectite.[45–51] Bandosz *et al.*[49] reported that PFA-based carbons templated on TAEN showed nanopores between 3.6 Å and 6 Å and, because of the presence of nanopores, the templated carbon demonstrated a molecular sieving effect. The preparation of nanopores via impregnation of activated carbon with PFA has been explored by Moreira *et al.*[52] and Soares *et al.*[53] and is mentioned by Wang and Yao.[43] Nanoporous-based sieving was also seen when PFA was placed on stainless steel supports and pyrolized to create a nanoporous carbon membrane.[54,55] The nanopores that were created from PFA to form the membrane had a PSD of 4.5-5.5 Å.[54,55]

Foley *et al.*[56–61] has completed extensive work with PFA and the production of carbogenic molecular sieves (CMS). They show that the adsorption of N_2 at 77 K is difficult to measure due to the high diffusion resistance of nitrogen into PFA-derived CMS. CO_2 and C_4H_{10} uptake data are provided to illustrate the effects of diffusion resistances found in PFA-derived CMS. The work shows that increasing the carbonization temperature and soak time increases the diffusional resistance of the material. N_2 adsorption studies on CMS derived from PFA containing polyethylene glycol (PEG) show that the PEG/PFA samples exhibit faster diffusion of nitrogen into the material when compared to the pure PFA carbon. The pore size calculated by the Horvath-Kawazoe[62] method for PEG/PFA-derived CMS is 5.5 Å.[61] In a review article the inability to calculate a PSD using N_2 isotherms is addressed. Foley shows that by using the Horvath-Kawazoe (HK) equation and the physical parameters for CH_3Cl that the PSD of PFA-derived CMS is centered at 5.5 Å.[63]

While the studies listed above are extensive, absent from the literature is an examination of the nanoporous carbon composites that contain both carbon and the silica template. Emphasis has been placed on synthesizing pure carbon materials. However, having an ordered, pure carbon material may not be necessary if the silica template can be lined or coated with carbon. One particular carbon composite of interest is PFA carbon supported by MCM-41. This particular composite material has not been studied in the literature. While PFA derived carbon, templated MCM-

41 carbon, and MCM-41 carbon composites are dominated by nanoporosity, only the composite material has a regular repeating structure.

Furthermore, very little work has been reported in the templating of an ordered nanoporous carbon. Developing a nanoporous carbon lining in a silica template becomes increasingly difficult as the size of the silica pore decreases because it is more difficult to suppress the formation of carbon in the entire volume of the template.[36] However, a well ordered nanoporous material could easily find applications as an adsorbent or a catalyst support. Developing a carbon-silica composite material provides a logical step in the development of a well ordered nanoporous carbon. Furthermore, understanding the type of nanoporosity present in the composite material is important for its application.

The purpose of this work is to synthesize a novel carbon silica composite (CSC) material by impregnating MCM-41 with PFA and to characterize the material to understand the nature of the resulting nanoporosity. The synthesis of this material is depicted conceptually in Figure 2.1, which shows a nanoporous carbon within the pores of mesoporous MCM-41. Synthesis conditions are discussed in relation to material size and quality. Results show the use of MCM-41 as a template to design an adsorbent material with a PSD similar to CMS. The parent MCM-41 material and CSC are characterized by N_2 adsorption, thermogravimetric analysis (TGA), and XRD. The properties of CSC are contrasted with the properties of a carbon prepared from PFA as a control. Additionally, adsorption isotherms for N_2, CO_2, CH_4, and C_2H_6 are presented for both the parent MCM-41 and CSC.

2.2 Experimental Section

Materials and Instrumentation

Tetramethylammonium hydroxide pentahydrate (TMAOH) (97%), tetramethylammonium silicate solution (TMASi) (99.99%, 15-20 wt % in water), sulfuric

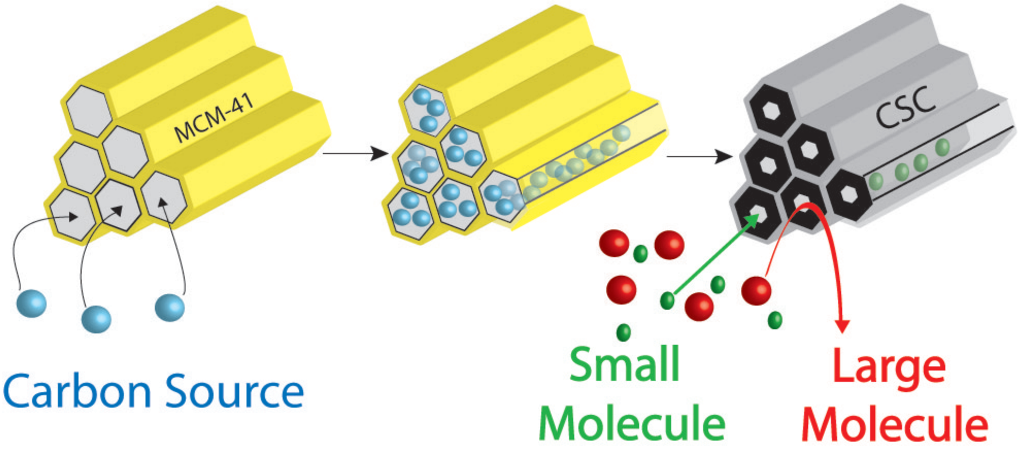

Figure 2.1: Conceptual depiction of CSC creation

acid (95.0-98.0%), polyfurfuryl alcohol (99%), benzene (99%), and aluminum chloride hydrate (99.999%) were all purchased from Sigma Aldrich. Hexadecyltrimethylammonium chloride (CTAC) (25%) in water solution was purchased from Pfaltz and Bauer. An ammonium hydroxide (29 wt %) water solution and Cab-O-Sil M5 were purchased from Fisher Scientific.

Adsorption isotherms were measured using the gravimetric apparatus described by Walton et al.[64] Cryogenic adsorption measurements were made with a Micromeritics ASAP 2010. X-Ray diffraction data were gathered using a Scintag X_1 θ/θ automated powder diffractometer with Cu target, a Peltier-cooled solid-state detector, and a zero background Si(510) support, and a copper X-ray tube as the radiation source.

Synthesis Method for MCM-41

The synthesis procedure was based on the work of Davis[3,4] and Edler and White.[7] A nominal 30 Å MCM-41 material was synthesized by combining 2.4 g 29 wt % ammonium hydroxide and 21.2 g of 29 wt % CTAC to form solution A. Then, 3.04 g of TMAOH was dissolved in 20 g of 10 wt % solution of TMASi to form solution B. The two solutions were then combined with stirring, and 4.5g of Cab-O-Sil M5, a fumed silica, was added to form the reaction gel. The reaction gel was then stirred at room temperature for 20 minutes. Next, the resulting gel was heated in a Teflon-lined autoclave at 80 °C for 3 days. The reaction vessel was removed from the oven after the initial 24 hours, allowed to cool to room temperature, the pH was adjusted to 10 using sulfuric acid, and the vessel was placed back in the oven. The solid product was recovered by vacuum filtration, washed with deionized water, and allowed to dry at ambient temperature. Finally, the dry solid was heated in air at 1 °C per minute to 540 °C and maintained at 540 °C for 10 hours.

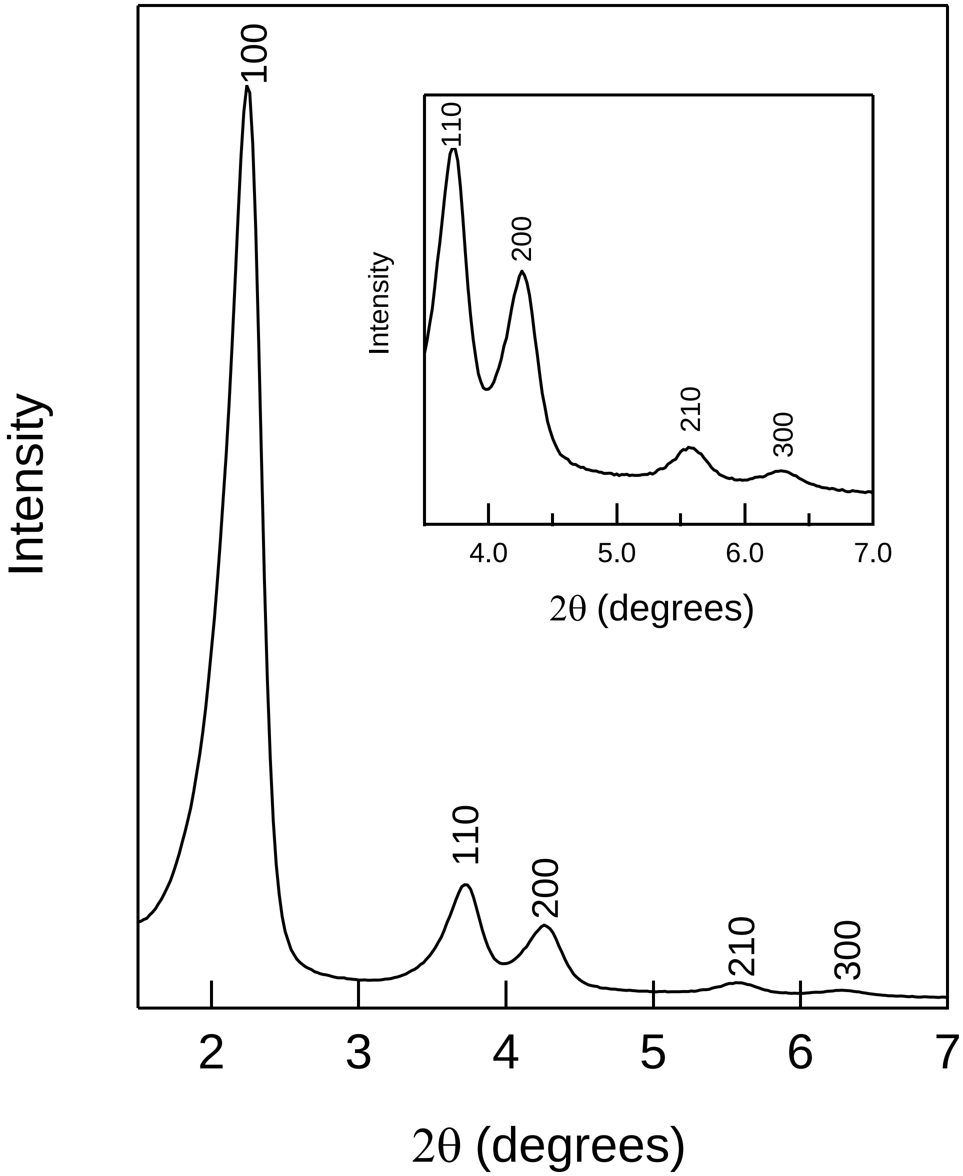

Figure 2.2: XRD pattern of parent MCM-41.

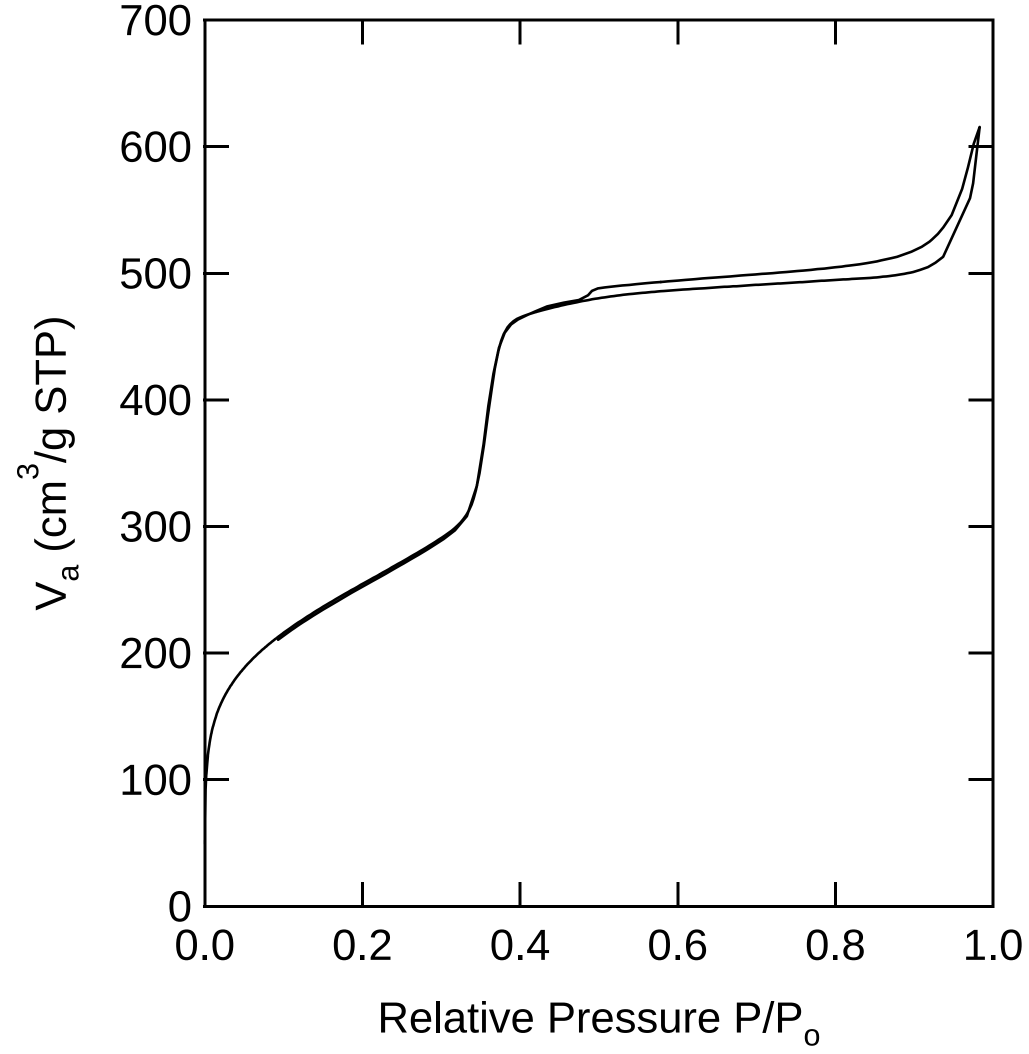

Figure 2.3: Nitrogen adsorption isotherm of parent MCM-41.

Synthesis Method for CSC

The impregnation of MCM-41 was performed following the work of Kyotani,[45] Ryoo et. al.,[30] and Kruk *et al.*[29] MCM-41 was first impregnated with aluminum by mixing MCM-41 with an aqueous solution of aluminum chloride. The solution was stirred for 3 hours, and the products was then recovered by vacuum filtration, dried in a convection oven, and calcined in air at 540 °C. The aluminated MCM-41 was placed in a Teflon-lined autoclave containing an 80% furfuryl alcohol in benzene solution. The impregnation solution was stirred for three days at room temperature. After stirring, the solution was statically heated for 24 hours at 80 °C. The product was recovered via vacuum filtration and placed in a reaction vessel, which was then heated at 1 °C per minute to 150 °C and maintained at 150 °C for 6 hours under N_2. Then the sample was heated at 5 °C per minute to 600 °C and maintained at 600 °C under N_2 for 3 hours.

The MCM-41 material was impregnated with furfuryl alcohol in excess. By weight the MCM-41 material comprised only 2% of the total weight of the solution. Impregnation in this manner was performed to ensure that the MCM-41 was sufficiently loaded and that the loading was not a function of the quantity of furfuryl alcohol present in the solution. Washing steps were not performed on the impregnated material after it was filtered from the PFA-benzene solution in order to prevent removing the PFA from the pores of the MCM-41.

2.3 Results and Discussion

Characterization

The MCM-41 parent material was characterized by XRD and adsorption isotherms prior to being impregnated with PFA. The XRD results show a highly ordered MCM-41 material as illustrated in Figure 2.2. A high degree of structural regularity is indicated by five distinct sharp peaks corresponding to five orders of X-ray diffraction.

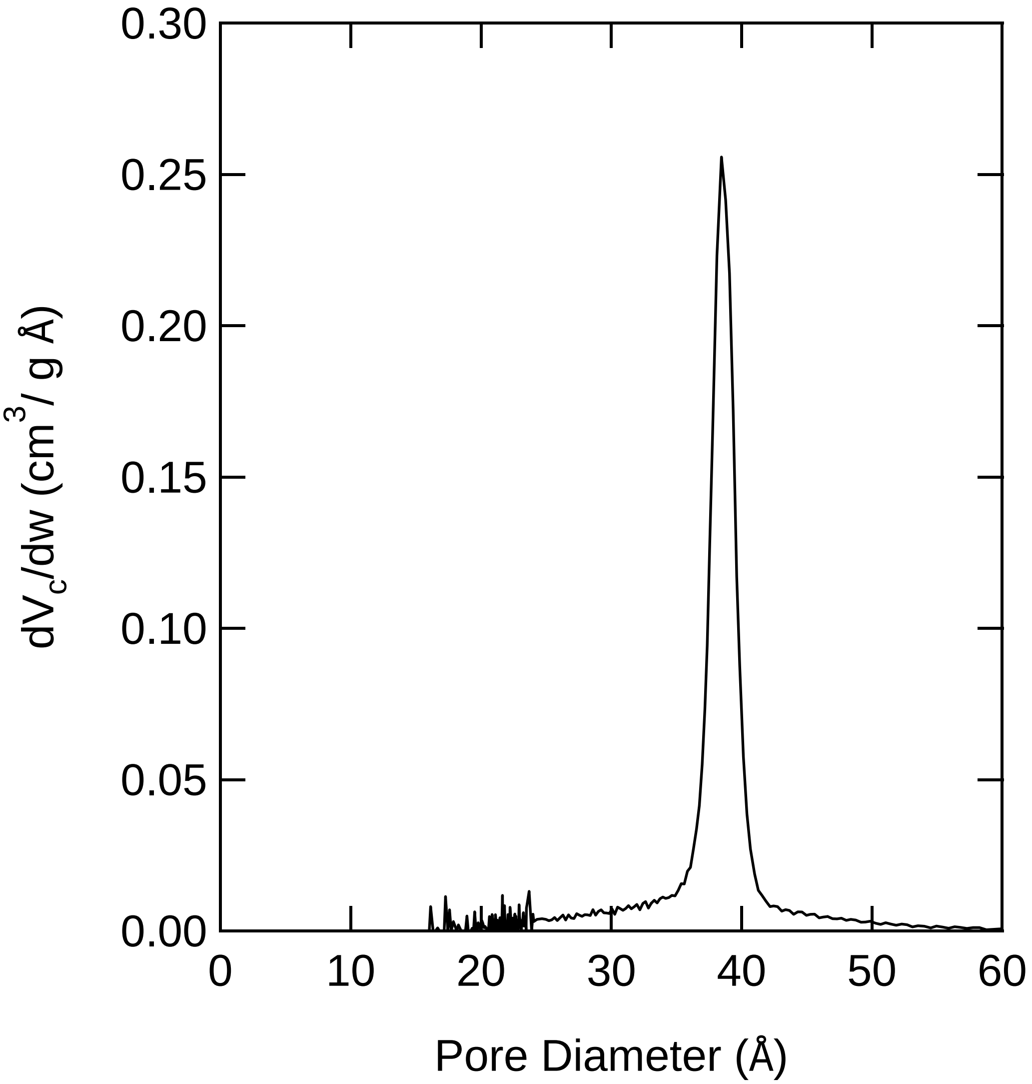

Figure 2.4: Pore size distribution via KJS method for parent MCM-41.

The MCM-41 material was also characterized using N_2 adsorption at 77 K in order to determine an average PSD. Figure 2.3 shows the MCM-41 N_2 adsorption isotherm, which is Type IV according to the IUPAC classification. For convenience, Kruk *et al.*[24] define primary mesopores as the pores that are defined by the MCM-41 channels. They also define secondary mesopores as large mesopores and small macropores (from about 5 to 200-400 nm) in which capillary condensation takes place at relative pressures higher than in primary mesopores but less than the saturation vapor pressure. The sharp rise near 0.4 P/P_o corresponds to condensation in the primary mesopores. As the size of the primary mesopores increases the capillary condensation step shifts to higher relative pressures and hysteresis becomes more pronounced. With MCM-41 materials that have a larger pore size the hysteresis loop continues into lower relative pressures beyond the primary mesopore condensation step. Several authors[23, 24, 65] have discussed the phenomenon of hysteresis in MCM-41. As the pore size of MCM-41 is further reduced, the capillary condensation step occurs at lower relative pressures and the hysteresis in the secondary mesopores is less pronounced.[23]

The PSD of MCM-41 materials was calculated using the KJS method.[11] Figure 2.4 shows the result for the parent MCM-41. The PSD shows a large developed peak near 38 Å. The PSD is consistent with data presented by others for a surfactant 16 carbon atoms in length.[23]

Using the N_2 adsorption data, a standard adsorption plot (alpha plot) was generated for the parent MCM-41 using LiChrospher Si-1000 Silica[66] as a silica reference. The results are presented in Figure 2.5. The solid lines seen on Figure 2.5 illustrate the data that were used in the calculation of the material properties. Using the method outlined by Do,[67] the alpha plot was used to calculate total surface area, external surface area, nanopore surface area, and nanopore volume. The results are summarized in Table 2.1.

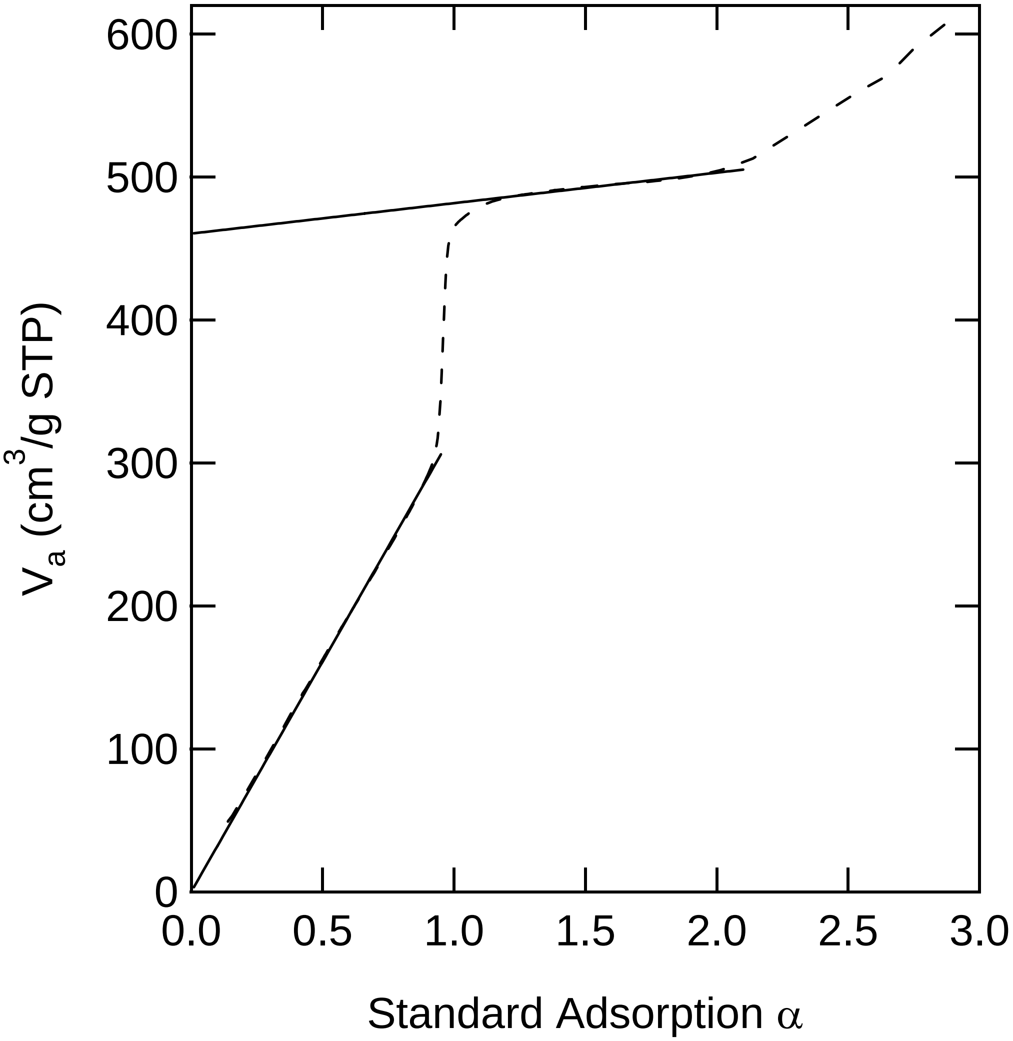

Figure 2.5: Standard adsorption plot for parent MCM-41.

After impregnating the parent MCM-41 material with PFA and carbonizing it inside the pores, the resulting CSC material was characterized with XRD, N_2 adsorption measurements, and TGA. The results are shown in Figures 2.6 through 2.10. Figure 2.6 shows that CSC maintains its long-range order. The peaks that are present in the base MCM-41 material are also present in CSC. Silica carbon composites of this type are known to maintain crystallinity so long as the silica template is not removed.[29,32] The XRD pattern is diminished in both intensity and the number of visible diffraction peaks due to the impregnation.

By examining the N_2 adsorption isotherm shape seen in Figure 2.7, it can be seen that CSC is dominated by nanoporosity. The PSD is centered at approximately 5 Å when calculated using the HK method as illustrated in Figure 2.8. When examined in detail, the PSD shows a narrow distribution of nanopores between 4.6 Å and 5.25 Å. There is no noticeable sign of mesoporosity present in the PSD with the exception of one data point at 20 Å, which represents only a small fraction of the total pore volume. The work presented here is consistent with the work of Shiflett *et al.*[54,55] concerning membranes formed with PFA. Shiflett *et al.* found the PSD to be centered between 4.5 Å and 5.5 Å.

To further examine the porosity of CSC, alpha plots were calculated using the N_2 adsorption data and nongraphitized carbon black (Cabot BP 280) as a reference material.[69] Figure 2.9 is consistent with a nanoporous material as illustrated by the deviations from linearity in the low pressure region. Using the alpha plot total surface area, external surface area, nanopore surface area, and nanopore volume were calculated and are summarized in Table 2.1.

A PFA carbon was also prepared as a control using the same conditions that were used to prepare CSC. Nitrogen adsorption experiments using the control were not possible due to the strong diffusion resistances of the material. Also, the control material contained no crystal order in the 0-7 2-theta range. The results of the control

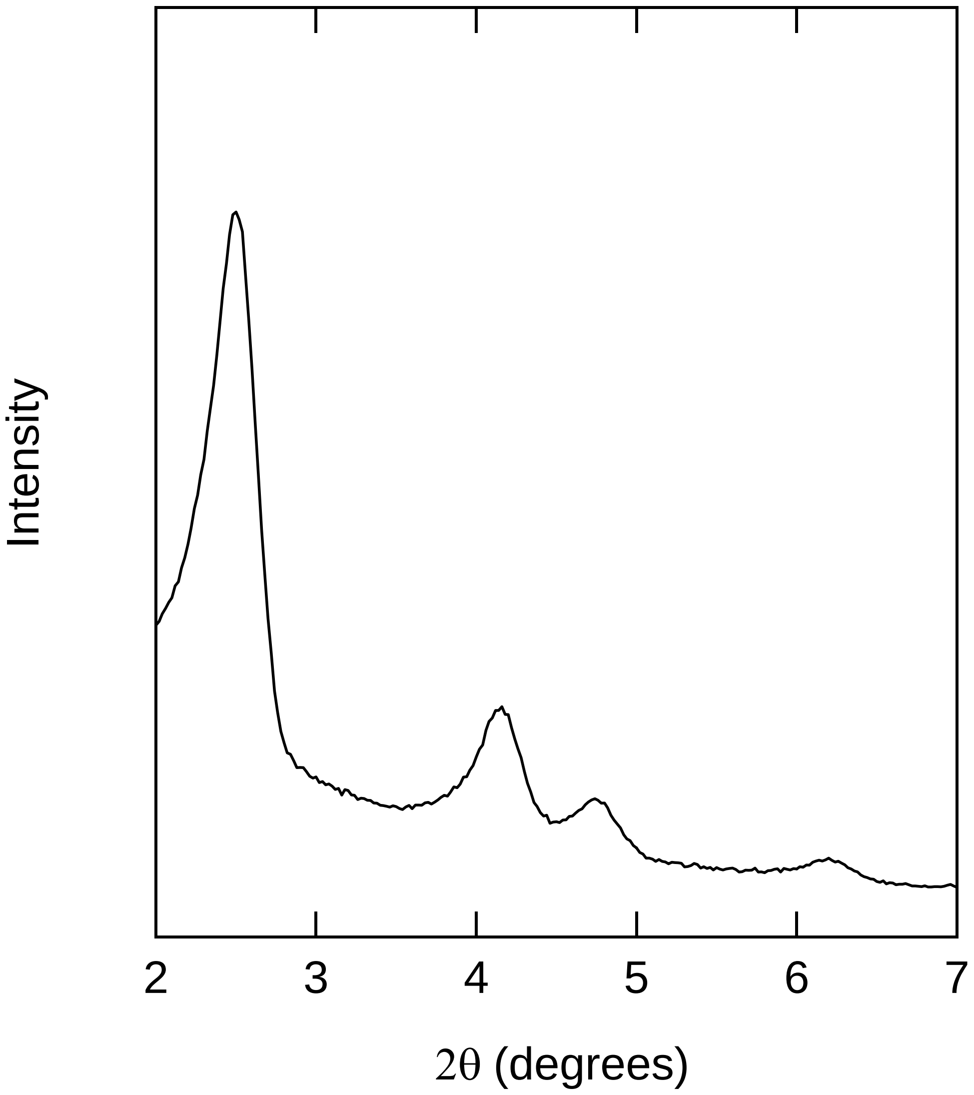

Figure 2.6: XRD pattern for CSC.

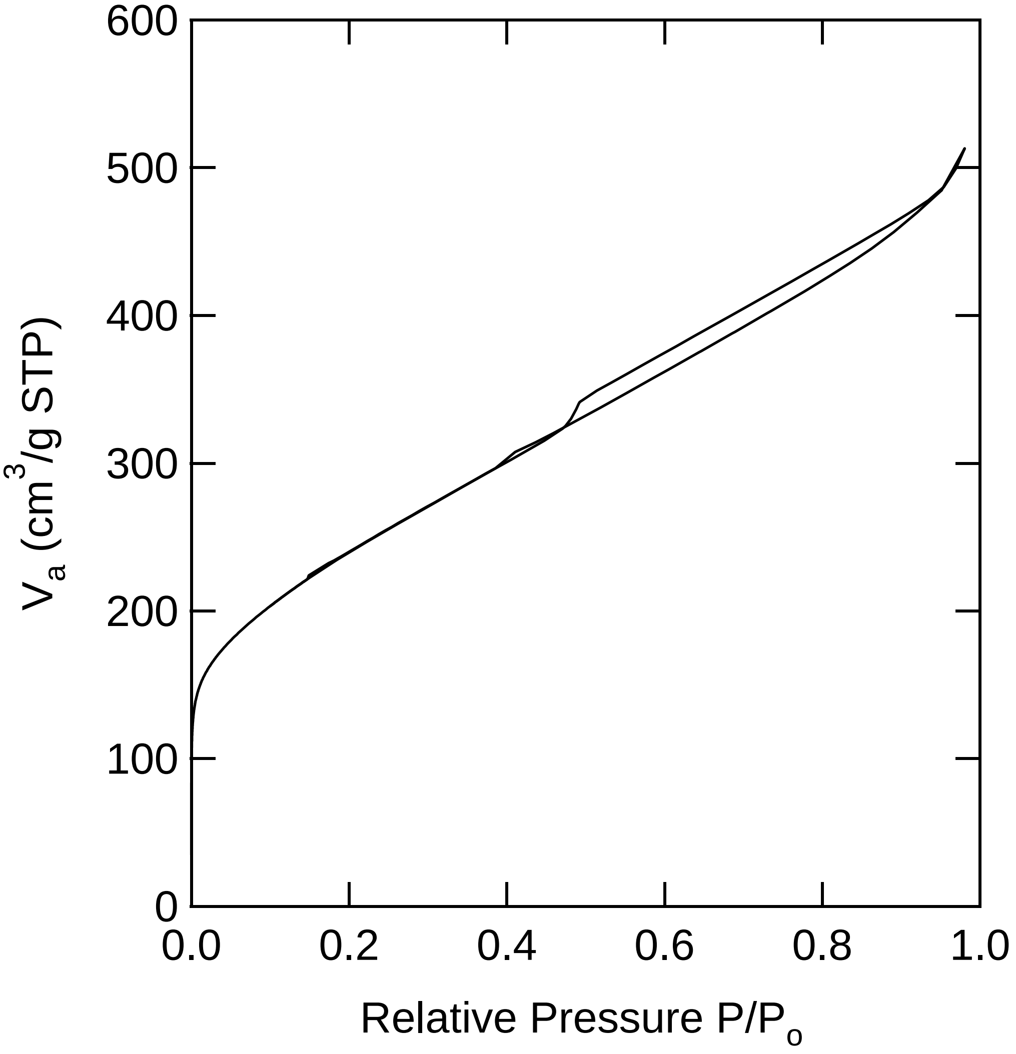

Figure 2.7: Nitrogen adsorption isotherm for CSC.

experiment are consistent with the work of Foley *et al.*[56–61] in that the nanoporosity of the material is readily detectable with N_2 adsorption experiments when the diffusional path of the N_2 is reduced with the introduction of larger mesopores. Therefore, the MCM-41 material acts in a similar manner as the PEG introduced into the carbogenic molecular sieves of Foley et al. The PSD of PEG/PFA-CMS materials is centered at 5.5 Å,[61] which is consistent with the 5.0 Å PSD found in CSC.

To provide an estimate of the total amount of carbon loaded into the pores of the MCM-41 material, a TGA experiment was performed. The samples were heated from room temperature in air at 5 °C per minute to 600 °C with an air flow rate of 10 ml per min. The sample was maintained at 600 °C for 5 hours. The final dwell temperature of 600 °C was selected for several reasons. First, Chen *et al.*[3] showed that calcined MCM-41 has a noticeable weight loss above 600 °C due to condensation of silanol groups. Also, the samples were synthesized near 600 °C, with template burn off at 540 °C and carbonization at 600 °C. Therefore, a TGA dwell temperature of 600 °C is consistent with the synthesis conditions. At higher temperatures there is also a greater potential of damage to the structure. The selected dwell temperature ensured that besides the carbon burn off there were no other coupled weight loss effects.

To verify that the TGA heating conditions would remove only the carbon from the CSC, the parent MCM-41 was examined. Figure 2.10 shows both the parent MCM-41 and CSC along with the temperature profile used during the TGA experiment. The parent MCM-41 shows a total weight loss of approximately 6.5 wt %. The weight loss is the result of the loss of adsorbed water, condensation of silanol groups, as well as the removal of any residual organic synthesis template. The TGA experiment for the parent material shows that only a small amount of weight is lost during the heating cycle.

CSC shows a 37 wt % loss during the experiment. The bulk of the weight

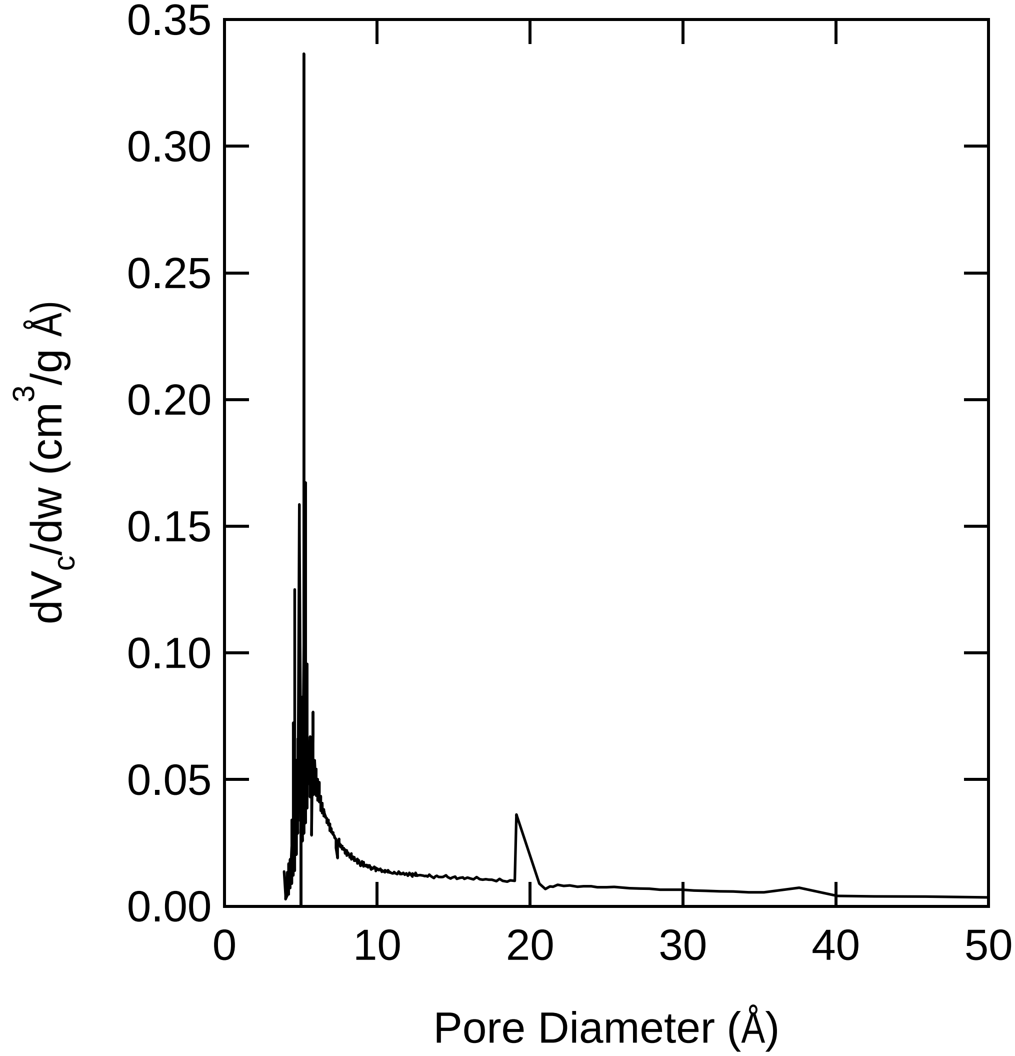

Figure 2.8: Pore size distribution via HK method for CSC.

loss in the TGA experiments can be attributed to carbon contained in the pores of the material. However, during the impregnation of the parent MCM-41 some carbon is deposited on the surface of the material and is also removed during the TGA experiment.

To place perspective on the weight loss of the impregnated material seen during the TGA experiment, the theoretical maximum loading was calculated using the liquid density of furfuryl alcohol (1.135 g/cc), its molecular weight (98.1), the total gas volume adsorbed by the sample (615.5 cm^3/g STP), and a conversion factor to convert N_2 gas volume to liquid volume. It was assumed that the entire pore volume of the solid was filled with PFA and that none of the carbon from the PFA was lost. The maximum theoretical loading for the parent MCM-41 was determined to be 39 wt %. While the weight loss seen in the TGA experiment for CSC is below the theoretical maximum, it would still be reasonable to assume that some of the carbon resides on the surface of the parent material.

Furthermore, the carbon in CSC could reside in the pores as either a porous lining, a non-porous lining, a non-porous filling, or a porous filling. A significant reduction in surface area would be expected from a non-porous lining or non-porous pore filling. However, the surface area and pore volume of the composite material was only slightly reduced. Therefore, it is reasonable that the carbon contained in the pores of CSC is porous and is present as either a porous lining or a porous filling. In the case of a porous lining the carbon may be filling the vast majority of the pore volume of the MCM-41 host. Therefore, the CSC material does not display strong signs of mesoporosity.

Furthermore, the results show that the MCM-41 channels have an effect on the porosity of PFA-derived carbon. The PFA control carbon has a very strong diffusion limitation that is not present in the CSC. Recent work shows that carbons derived from PFA maintain a blend of mesopores and nanopores but that processing the

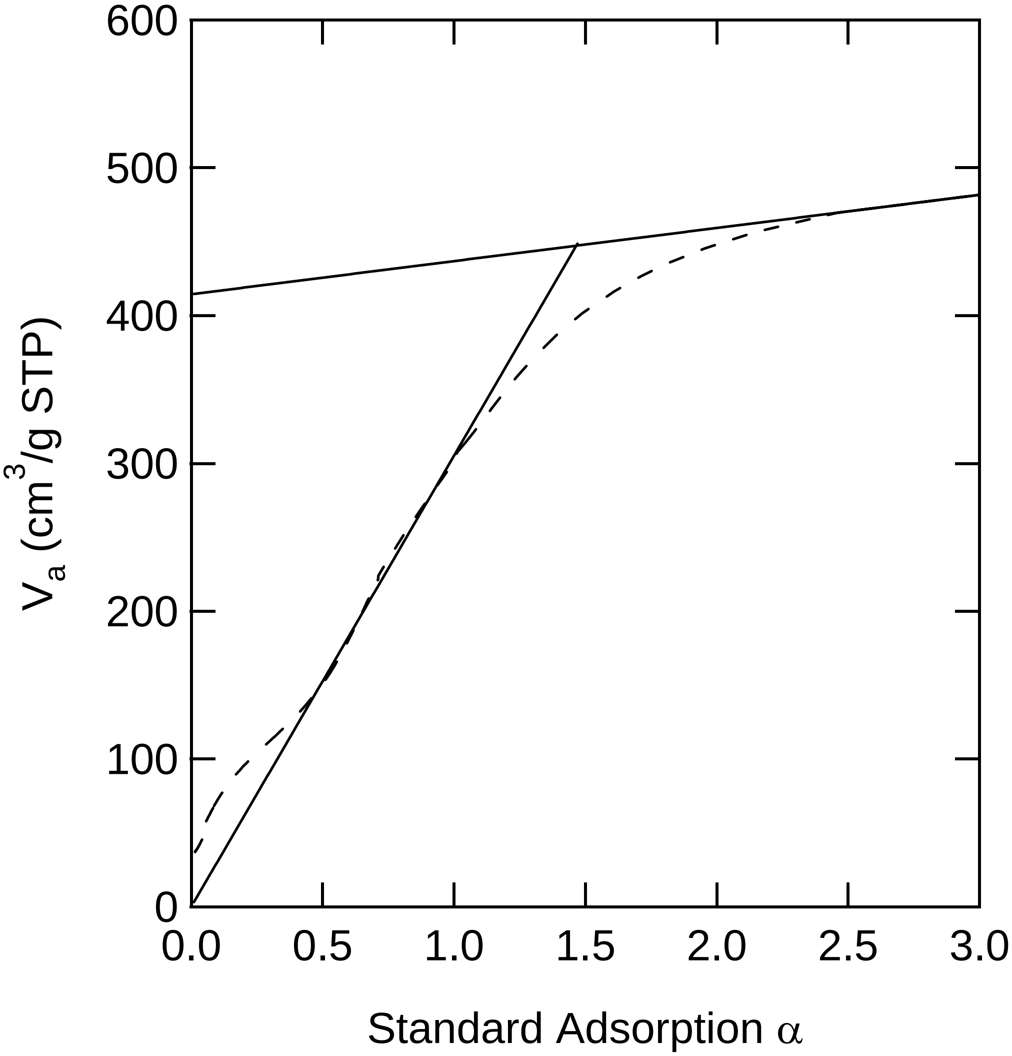

Figure 2.9: Standard adsorption plot for CSC.

Table 2.1: Physical properties of MCM-41 and impregnated MCM-41.

Sample	Parent MCM-41	Impregnated MCM-41
S_{BET} (m^2/g)	910	850
C_{BET}	116	166
S_α (m^2/g)	800	835
S_{ext} (m^2/g)	92.7	97.7
S_{meso} (m^2/g)	710	–
V_{meso} (cm^3/g)	0.713	–
S_{nano} (m^2/g)	–	740
V_{nano} (cm^3/g)	–	0.642
V_{max} (cm^3/g)	0.952	0.794
d_{HK} (Å)	32.5	5.25
d_{KJS}(Å)	38.0	–

material above 400°C collapses the mesopores.[68] However, in the case of the CSC the mesopores of the MCM-41 do not collapse during the processing of the material and thus provide a means of increasing the diffusion rates of gases within the material.

The surface area has also been examined on a per carbon basis. By using the carbon loading data from the TGA experiment, the surface area was scaled to reflect adsorption based only on the weight of the carbon contained in CSC. When considered on a per carbon basis, CSC has a surface area of 2290 m^2/g. The per carbon basis surface area is more than twice the surface area of traditional activated carbons. However, there may be residual patches of MCM-41 that are not lined with carbon but are contributing to the adsorption.

By maintaining the MCM-41 silica template in CSC, an ordered, templated nanoporous carbon is obtained. CSC is unique when compared to templated mesoporous carbons that have been extracted from silica structures. Specifically, a 5 Å pore, high surface area, and regular structure are distinctive relative to other templated carbons. The surface area of CSC is also substantially higher than the surface area of pure PFA carbons and PEG-modified PFA carbons.[61] The unique structure of CSC is well suited for applications requiring an ordered nanoporous carbon. To the best of our knowledge, CSC is the only nanoporous carbon templated material with such distinctive physical properties.

Adsorption Isotherms

Several isotherms were measured to understand how the carbon impregnated into MCM-41 affects adsorption equilibria. Room temperature isotherms of N_2, CO_2, CH_4, and C_2H_6 were measured for the parent MCM-41, CSC, and the control. Adsorption equilibria data for the PFA control carbon were compared to similar data taken by others.[61] The isotherms for CSC are also presented on a per weight of carbon basis and are compared to isotherms for BPL activated carbon. The results of these experiments are illustrated in Figures 2.11-2.14. The experimental data were fit to either a Langmuir isotherm

$$n = \frac{n^s KP}{1 + KP} \tag{2.1}$$

where n^s is the monolayer capacity and K is the equilibrium constant or a Toth isotherm

$$P = \left[\frac{b}{(n/n_s)^{-t} - 1} \right]^{1/t} \tag{2.2}$$

where b and t are constants and n_s is the saturation loading. The values of parameters for these equations are presented in Tables 2.2 and 2.3.

The saturation values presented in Tables 2.2 and 2.3 provide a reliable fit to the data measured. Because the isotherm data were measured at low pressure, the Henry's law constants for the adsorption can be calculated as the product of the saturation loading and the equilibrium constant K. It should be noted, however, that more accurate saturation loadings could be obtained if the adsorption isotherms covered a broader range of pressures. The saturation loadings of MCM-41 are higher than the other materials because of the large open pore structure of the material. Measuring the adsorption isotherms at a broader range of pressures would reduce these values and more accurately reflect the true saturation loading.

The isotherms of the parent MCM-41 are consistent with the data reported by He and Seaton.[70] The data show limited adsorption of N_2 and CH_4 because of the large pores of MCM-41 relative to the 3.0 Å and 4.0 Å diameters of N_2 and CH_4, respectively. Also, methane is non-polar and N_2 has only a slight quadrapole moment, thus limiting its adsorption on a silica surface. CO_2, however, has a strong quadrapole moment and interacts electrostatically with the silica surface, thus promoting adsorption. C_2H_6 has the largest kinetic diameter of gases examined and therefore adsorbs more effectively than the smaller N_2 and CH_4.

As is evident in Figure 2.13, CSC shows an appreciable increase in adsorption for all of the light gases studied. The increase in adsorption is primarily due to a

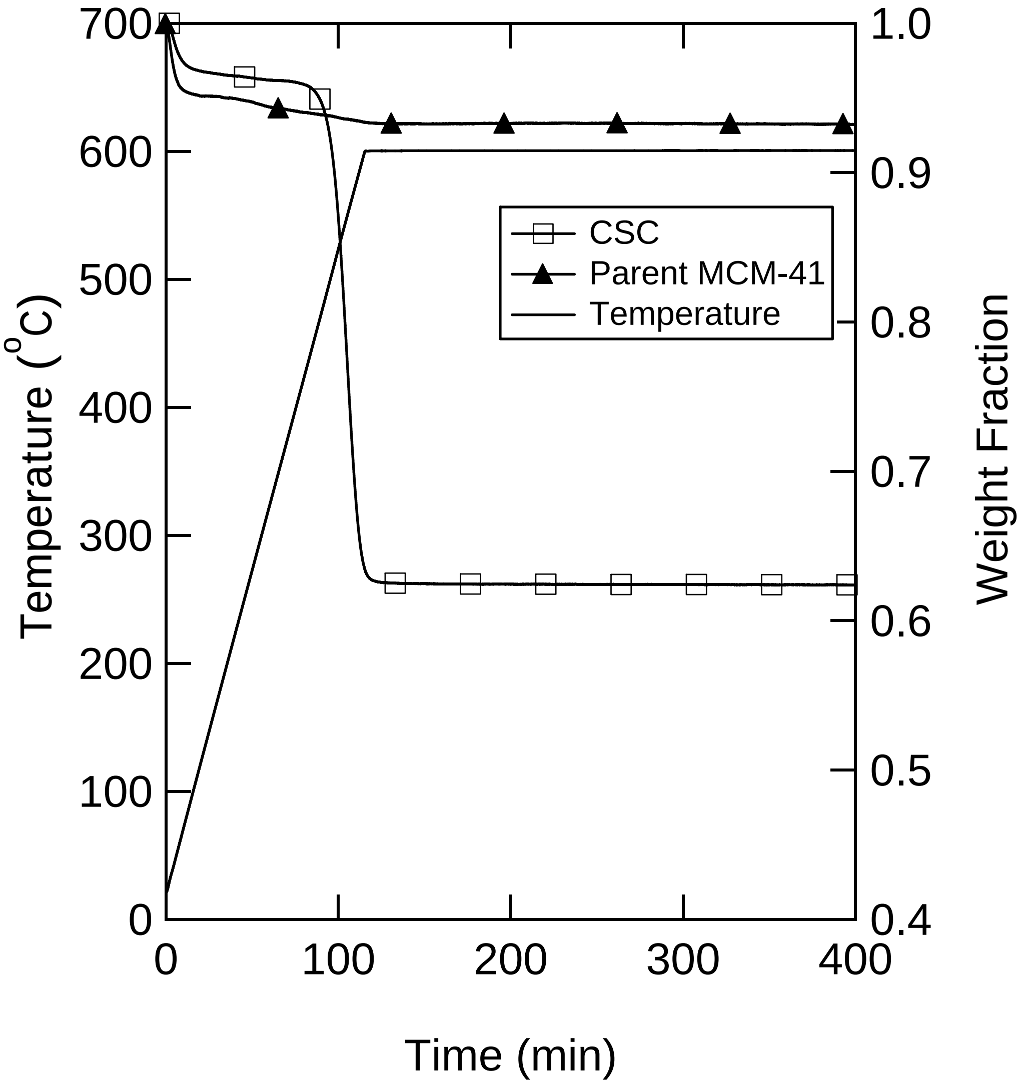

Figure 2.10: TGA results for both parent MCM-41 and CSC.

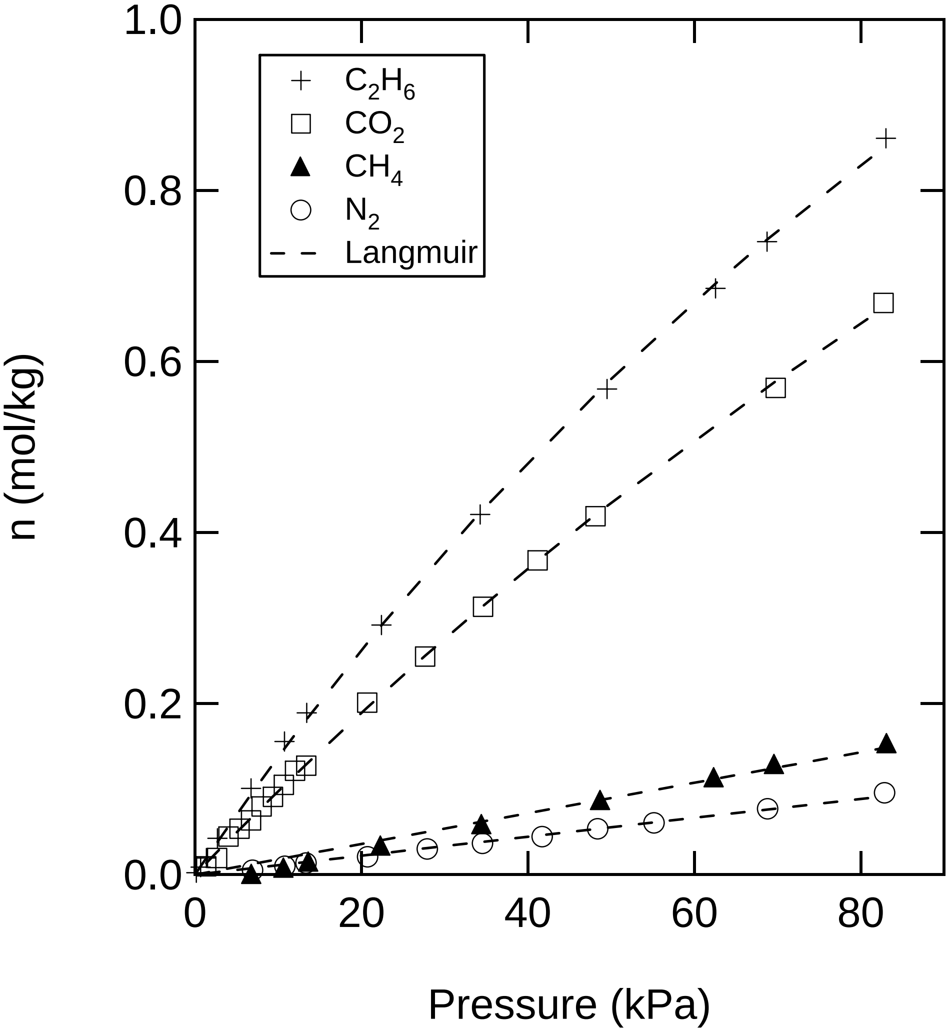

Figure 2.11: Adsorption isotherms for parent MCM-41.

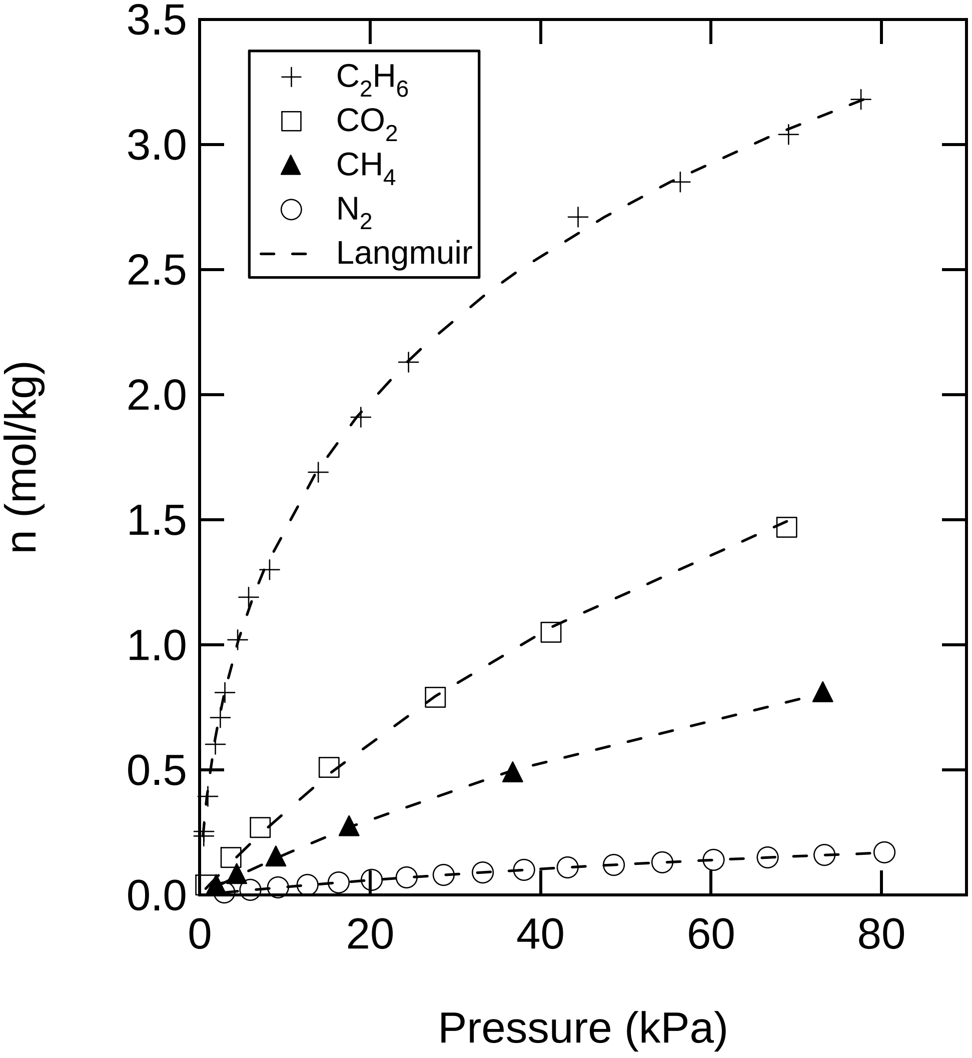

Figure 2.12: Adsorption isotherms for BPL activated carbon.

Table 2.2: Parameters used in Langmuir isotherms.

Adsorbent / Gas	n^s (mol/kg)	$K \times 10^3$ (kPa^{-1})
CSC		
CO_2	2.62	9.30
CH_4	0.96	13.96
N_2	1.43	1.53
Parent MCM-41		
C_2H_6	2.95	4.88
CO_2	3.27	3.06
CH_4	32.3	0.056
N_2	20.5	0.054
BPL activated carbon		
CO_2	3.64	10.1
CH_4	2.15	8.23
PFA control		
CO_2	2.08	29.6

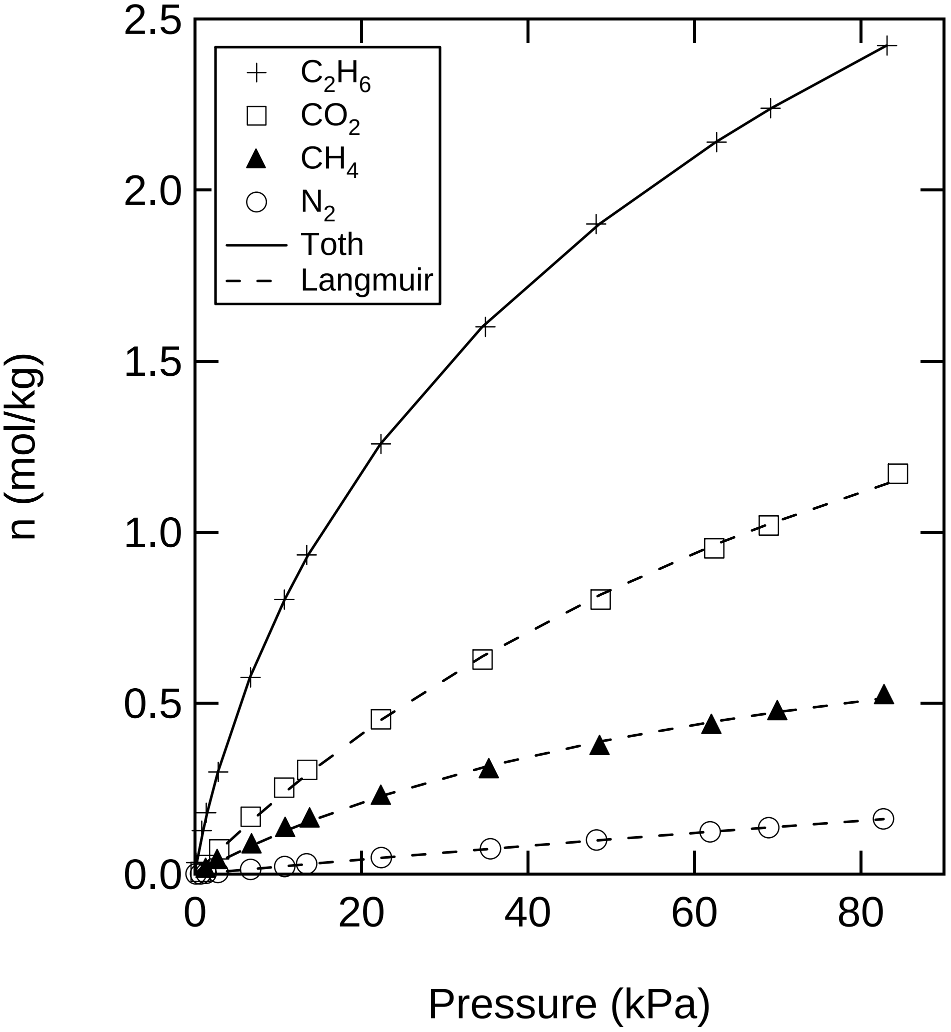

Figure 2.13: Adsorption isotherms for CSC.

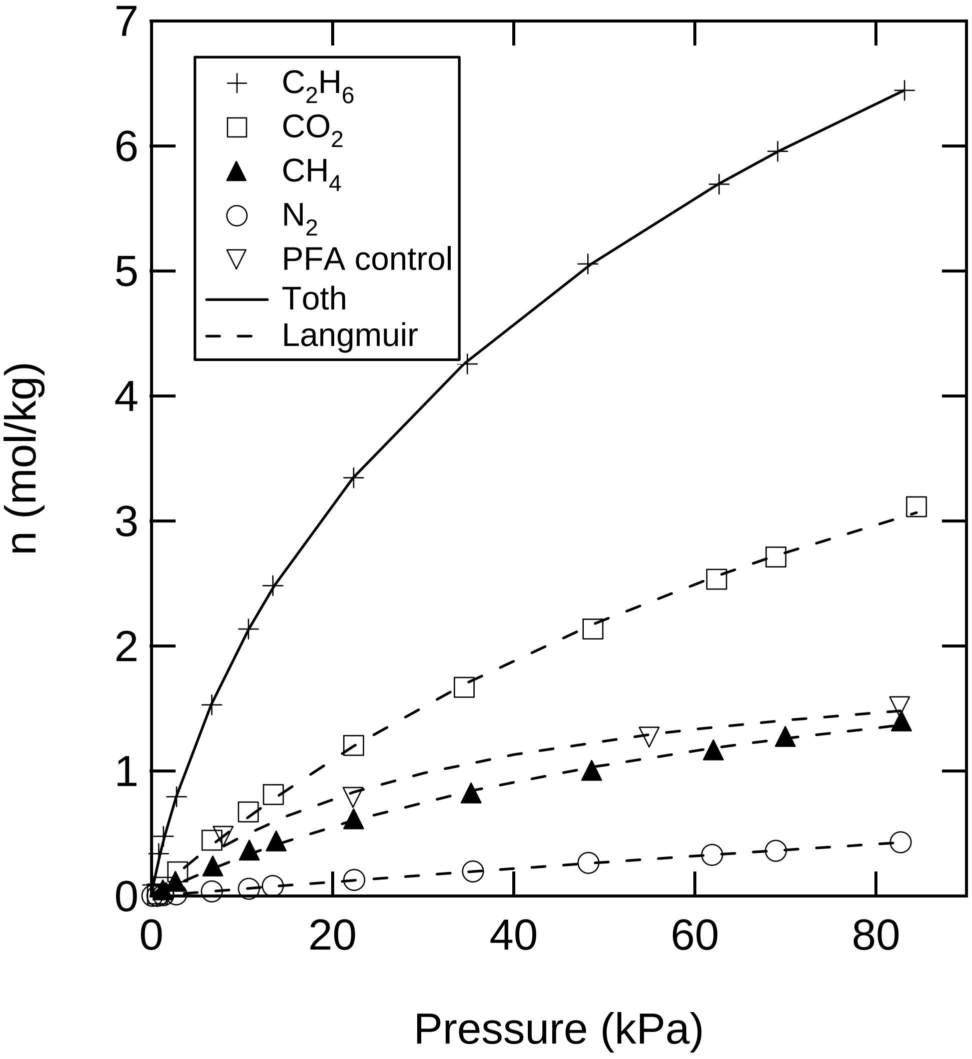

Figure 2.14: Adsorption isotherms for CSC on per carbon basis and for control.

decrease in the pore diameter. By decreasing the pore diameter, the molecules in the pores of the material experience a stronger attractive potential from the pore wall and are therefore more readily adsorbed. For example, the increase in the adsorption of both N_2 and CH_4 relative to pure MCM-41 is due to the smaller pore size of the impregnated material. The carbon surface of the pore walls of CSC is also different than pure MCM-41 and helps to promote the adsorption of straight chain hydrocarbons such as C_2H_6. However, the carbon surface does not promote the adsorption of charged species such as CO_2.

CSC behaves similarly to BPL activated carbon as illustrated by the adsorption isotherms presented in Figure 2.12. The similar adsorption patterns seen between CSC and BPL shows that the adsorbate is interacting with a carbon surface. The isotherm for N_2 on BPL presented in Figure 2.12 was reproduced using

$$P = n \exp[k_o + (k_1/T) + (k_2 n/T)] \tag{2.3}$$

from the work of Mahle *et al.*[71] with T in K, n in mol/kg, and P in kPa and where $k_o = 22.75$, $k_1 = -5101$, and $k_2 = 922$. The adsorption data for CO_2, CH_4, and C_2H_6 were used as presented elsewhere.[72–74] The BPL carbon shows a greater total volume adsorbed for each of the gases considered relative to the impregnated material.

Using the total carbon loading gathered via the TGA experiments, the isotherm data for CSC were scaled to show adsorption equilibria on a per weight carbon only basis. The isotherms for CSC on a per weight of carbon basis are presented in Figure 2.14. The per carbon basis isotherms for CSC shows a greater total adsorption for each of the gases studied when compared to BPL carbon.

Also presented in Figure 2.14 is the adsorption isotherm for CO_2 on the PFA control carbon. The isotherm for the control carbon is consistent with the uptake data of Lafyatis et al.[61] for CO_2. Isotherm data for other gases on the control material were not gathered due to the extensive amount of time required to reach equilibrium. The uptake of CO_2 on the PFA control carbon was substantially slower

Table 2.3: Toth isotherm parameters for C_2H_6.

Adsorbent	n_s (mol/kg)	b (kPa)^t	t
CSC	7.65	5.91	0.474
BPL activated carbon	11.74	1.52	0.282

than the uptake of CO_2 by CSC. While CSC took only minutes to equilibrate, the PFA control carbon required several hours to reach equilibrium. The faster uptake of CO_2 by CSC relative to the control carbon is consistent with the uptake data for the PEG/PFA-CMS materials of Foley et al.[56–61] The decrease in time required for CSC to reach equilibrium provides further evidence of the MCM-41 decreasing the diffusional path of the PFA carbon.

2.4 Conclusions

The impregnation of MCM-41 with polyfurfuryl alcohol and the subsequent carbonization of the silica polymer composite results in a carbon-silica composite (CSC) material that has a high surface area, approximately 850 m^2/g, and is dominated by nanoporosity with pore sizes of approximately 5 Å. CSC has a Type I isotherm and shows a crystal order that is the same as the parent MCM-41 material. The MCM-41 structure shortens the adsorbate diffusional path, and therefore the material behaves similarly to the PEG/PFA-derived CMS of Foley et al.[56–61] The shorter diffusional path allows CSC to reach equilibrium faster than carbon derived from pure polyfurfuryl alcohol for the gases N_2, CH_4, C_2H_6, and CO_2. The decreased pore size of CSC provides for better adsorption of gases studied relative to the parent MCM-41. The narrow 5 Å pores and the regular order of CSC are good incentives for its application as an adsorbent for specific applications.

References

[1] Kresge, C.T; Leonowicz, M.E.; Roth, W.J.; Vartuli, J.C.; Beck, J.S. *Nature* 359, (1992), 710.

[2] Beck, J.S.; Vartuli, J.C.; Roth, W.J.; Leonowicz, M.E.; Kresge, C.T.; Schmitt, K.D.; Chu, C.T-W.; Olson, D.H.; Sheppard, E.W.; McCullen, S.B.; Higgins, J.B.; Schlenker, J.L. *J. Am. Chem. Soc.* 114, (1992), 10834.

[3] Chen, C.Y.; Li, X.H.; Davis, M.E. *Micro. Mater.* 2, (1993), 17.

[4] Chen, C.Y.; Burkett, S.L.; Li, H.X.; Davis, M.E. *Micro. Mater.* 2, (1993), 27.

[5] Park, D.H.; Cheng, C.F.; Klinowski, J. *Bull. Korean Chem. Soc.* 18, (1997), 379.

[6] Ryoo, R.; Kim, J.M. *J. Chem. Soc., Chem. Commun.* 7, (1995), 711.

[7] Edler, K.J.; White, J.W. *Chem. Mater.* 9, (1997), 1226.

[8] Edler, K.J.; Reynolds, P.A. White J.W., and David C. *J. Chem. Soc. Fara. Trans.* 93, (1997), 199.

[9] Edler, K.J.; White, J.W. *J. Mater. Chem.* 9, (1999), 2611.

[10] Huo, Q.; Margolese, D.I.; Stucky, G.D. *Chem. Mater.* 8, (1996), 1147.

[11] Kruk, M.; Jaroniec, M.; Sayari, A. *Langmuir* 13, (1997), 6267.

[12] Sayari, A.; Liu, P.; Kruk, M.; Jaroniec, M. *Chem. Mater.* 9, (1997), 2499.

[13] Sayari, A.; Yang, Y.; Kruk, M.; Jaroniec, M. *J. Phys. Chem. B.* 103, (1999), 3651.

[14] Matos, J.R.; Mercuri, L.P.; Kruk, M.; Jaroniec, M. *Chem. Mater.* 13, (2001), 1726.

[15] Kruk, M.; Jaroniec, M.; Yang, Y.; Sayari, A. *J. Phys. Chem. B.* 104, (2000), 1581.

[16] Kleitz, F.; Wolfgang, S.; Schuth, F. *Micro. Meso. Maters.* 44–45, (2001), 95.

[17] Broyer, M.; Valange, S.; Bellata, J.P.; Betrand, O.; Weber, G.; Gabelica, Z. *Langmuir* 18, (2002), 5083.

[18] Cassiers, K.; Linssen, T.; Mathieu, M.; Benjelloun, M.; Schrijnemakers, K.; Van Der Voort, P.; Cool, P.; Vansant, E.F. *Chem. Mater.* 14, (2002), 2317.

[19] Gusev, V.Y.; Feng, X.; Bu, Z.; Haller, G.L.; O'Brien, J.A. *J. Phys. Chem.* 100, (1996), 1985.

[20] Zhang, Y.; Wu, Dong.; Sun, Y.; Peng, S. *Mater. Letters* 55, (2002), 17.

[21] Mori, T.; Kuroda, Y.; Yoshikawa, Y.; Mahiko, N.; Kittaka, S. *Langmuir* 18, (2002), 1595.

[22] Zhu, H.Y.; Zhao X.S.; Lu G. Q.; Do D.D.; *Langmuir* 12, (1996), 6513.

[23] Kruk, M.; Jaroniec, M.; Kim, J.M.; Ryoo, R. *Langmuir* 15, (1999), 5279.

[24] Kruk, M.; Jaroniec, M.; Sakamoto, Y.; Terasaki, O.; Ryoo, R.; Ko, C.H. *J. Phys. Chem. B* 104, (2000), 292.

[25] Barrett, E.P.; Joyner, L.G.; Halenda, P.P. *J. Am. Chem. Soc.* 73, (1951), 373.

[26] Choma, J.; Jaroniec, M.; Burakiewicz-Mortka, W. *App. Sur. Sci* 196, (2002), 216.

[27] Sakintuna, B.; Yurum, Y. *Ind. Eng. Chem. Res.* 44, (2005), 2893.

[28] Ryoo, R.; Joo, S.H.; Jun, S. *J. Phys. Chem. B* 103, (1999) 7743.

[29] Kruk, M.; Jaroniec, M.; Ryoo, R.; Joo, S.H. *J. Phys. Chem. B.* 104, (2000), 7960.

[30] Ryoo, R.; Jun, S.; Kim, J.M.; Kim, M. J. *Chem. Commmun.* 22, (1997), 2225.

[31] Jun, S.; Ryoo, R. *J. Catalysis* 195, (2000), 237.

[32] Lee, J.; Yoon, S.; Oh, S.M.; Shin, C.H.; Hyeon, T. *Adv. Mater.* 12, (2000), 359.

[33] Joo, S.H.; Choi, J.S.; Oh, I.; Kwak, J.; Liu, Z.; Terasaki, O.; Ryoo, R. *Nature* 412, (2001) 169.

[34] Zhao, D.; Feng, J.; Huo, Q.; Melosh, N.; Fredrickson, G.H.; Chemlka, B. F.; Stucky, G. D. *Science* 279, (1998), 548.

[35] Ryoo, R.; Joo, S.H.; Kruk, M.; Jaroniec, M. *Adv. Mater.* 13, (2001), 677.

[36] Kruk, M.; Jaroniec, M.; Kim, T.W.; Ryoo, R. *Chem. Mater.* 15, (2003), 2815.

[37] Ryoo, R.; Joo, S.H.; Jun, S.; Tsubakiyama, T.; Terasaki, O. *Zeolites and mesoporous materials at the dawn of the 21st century*, Montpellier, France, 2001.

[38] Liu, X.; Tian, B.; Yu, C.; Gao, F.; Xie, S.; Tu, B.; Che, R.; Peng,L.-M.; Zhao, D. *Angew. Chem., Int. Ed.* 41, (2002), 3876.

[39] Chan, Y.T.; Lin, H.P.; Chung, Y.M.; Liu, S.T. *Chem. Commun.* 23, (2002), 2878.

[40] Ryoo, R.; Joo, S.H.; Jun, S. *J. Phys. Chem. B.* 103, (1999), 7743.

[41] Huo, Q.; Margolese, D.I.; Ciesla, U.; Feng, P.; Gier, T.E.; Sieger, P.; Leon, R.; Petroff, P.M.; Schuth, F.; Stucky, G.D. *Nature* 368, (1994), 317.

[42] Jun, S.; Joo, S.H.; Ryoo, R.; Kruk, M.; Jaroniec, M.; Liu, Z.; Ohsuna, T.; Terasaki, O. *J. Am. Chem. Soc.* 122, (2000) 10712.

[43] Wang, H.; Yao, J. *Ind. Eng. Chem. Res.* 45, (2006), 6393.

[44] Kyotani, T.; Nagai, T.; Inoue, S.; Tomita, A. *Chem. Mater.* 9, (1997), 609.

[45] Kyotani, T.; Yamada, H.; Sonobe, N.; Tomita, A. *Carbon* 32, (1994), 627.

[46] Sonobe, N.; Kyotani, T.; Tomita, A. *Carbon* 29, (1991), 61.

[47] Sonobe, N.; Kyotani, T.; Tomita, A. *Carbon* 28, (1990), 483.

[48] Bandosz, T. J.; Jagiello, J.; Putyera, K.; Schwarz, J. A. *Chem. Mater.* 8, (1996), 2023.

[49] Bandosz, T. J.; Jagiello, J.; Putyera, K.; Schwarz, J. A. *Langmuir* 11, (1995), 3964.

[50] Bandosz, T. J.; Putyera, K.; Jagiello, J.; Schwarz, J. A. *Carbon* 32, (1994), 659.

[51] Bandosz, T. J.; Putyera, K.; Jagiello, J.; Schwarz, J. A. *Clays Clay Miner.* 44, (1996), 237.

[52] Moreira, R.F.P.M.; Jose, H.J.; Rodrigues, A.E. *Carbon* 39, (2001), 2269.

[53] Soares, J.L.; Jose, H.J.; Moreira, R. *Braz. J. Chem. Eng.* 20, (2003), 75.

[54] Shiflett, M.B.; Foley, H.C. *Science* 285, (1999), 1902.

[55] Shiflett, M.B.; Pedrick, J.F.; McLearn, S.R.; Subramoney, S.; Foley H.C. *Adv. Mater.* 12, (2000), 21.

[56] Yi, B.; Rajagopalan, R.; Foley, H.C.; Kim, U.J.; Liu, X.M.; Eklund, P.C. *J. Amer. Chem. Soc.* 34, (2006), 11307.

[57] Strano, M.S.; Agarwal, H.; Pedrick, J.; Redman, D.; Foley, H.C. *Carbon* 13, (2003), 2501.

[58] Strano, M.S.; Zydney, A.L.; Barth, H.; Wooler, G.; Agarwal, H.; Foley, H.C. *J. Mem. Sci.* 2, (2002), 173.

[59] Mariwala, R.K.; Foley, H.C. *Ind. Eng. Chem. Res.* 10, (1994), 2314.

[60] Mariwala, R.K.; Foley, H.C. *Ind. Eng. Chem. Res.* 3, (1994), 607.

[61] Lafyatis, D.S.; Tung, J.; Foley, H.C. *Ind. Eng. Chem. Res.* 30, (1991), 865.

[62] Horvath, G.; Kawazoe, K. *J. Chem. Eng. Japan* 16, (1983), 470.

[63] Foley, H.C. *Micro. Maters.* 4, (1995), 407.

[64] Walton K.S.; Abney, M.B.; LeVan, M.D. *Micro. Meso. Maters.*, 91, (2006), 78.

[65] Tanev, P.T.; Pinnavaia, T.J. *Chem. Mater.* (1996), 2068.

[66] Jaroniec, M.; Kruk, M.; Olivier, J.P. *Langmuir* 8, (1999), 15, 5410–5413.

[67] Do, D.D. *Adsorption Analysis Equilibria and Kinetics*, Imperial College Press, London, 1998.

[68] Burket, C.L.; Rajagopalan, R.; Marencic A.P.; Dronvajjala, K.; Foley H.C. *Carbon* 44, (2006), 2957.

[69] Kruk, M.; Jaroniec, M.; Gadkaree, K.P. *J. Colloid and Interface. Sci.* 192, (1997), 250.

[70] He, Y; Seaton, N.A. *Langmuir* 22, (2006), 1150.

[71] Mahle, J.J.; Friday, D.K.; LeVan, M.D. *Ind. Eng. Chem. Res.* 35, (1996), 2342.

[72] Russell, B.P.; LeVan, M.D. *Ind. Eng. Chem. Res.* 36, (1997), 2380.

[73] Walton, K.S.; Pigorini, G.; LeVan, M.D. *Chem. Eng. Sci.* 59, (2004), 4423.

[74] Walton, K.S.; LeVan, M.D. *Sep. Sci. Technol.* 41, (2006), 485.

CHAPTER III

CARBON-SILICA COMPOSITE ADSORBENT: SENSITIVITY TO SYNTHESIS CONDITIONS

3.1 Introduction

A great deal of work has been performed recently to design mesoporous carbons by using controllable mesoporous silica templates. These materials provide a foundation for the design of a tunable, nanoporous, carbonaceous adsorbent. In our previous work,[1] several examples were discussed in a literature review in which a variety of different silica templates were related to the resulting templated carbon they produce. Of particular interest is the work performed by Kruk *et al.*[2] and Lee *et al.*[3] in which it was shown that MCM-41 templated carbon composite materials develop nanoporosity and that the carbon material recovered after extraction of the MCM-41 template is disordered. Kruk *et al.*[4] and Fuertes[5] show that carbon templated from SBA-15 can be controlled by the selection of the proper carbonization processing conditions. Also discussed in the review is the work of Foley *et al.*[6–8] on the development of polyfurfuryl alcohol (PFA) derived carbogenic molecular sieves and furfuryl alcohol derived carbon membranes with high ideal selectivities for small molecules such as nitrogen, oxygen, helium, and hydrogen.

The development of a controllable carbon adsorbent, as well as the established work concerning the application of PFA carbon membranes, makes the impregnation of MCM-41 by PFA for the production of a nanoporous carbon adsorbent uniquely appealing. In our previous work, we documented several unique features of our PFA impregnated MCM-41 carbon silica composite (CSC) material. We showed that our CSC material is nanoporous, contains exclusively a 5 Å pore, a high surface area (848 m^2/g), and a long range order. Each of these features provides evidence of the synthesis of a well defined and ordered carbon material. Moreover, in order to further develop CSC materials as a tunable carbonaceous adsorbent, it is necessary to understand better the effects of synthesis conditions on the resulting material.

Burket *et al.*[9] have provided extensive details concerning the carbonization of furfuryl alcohol. The authors state that the porosity formed from carbonizing PFA is generated spontaneously as ether linkages in furan rings fracture around 300 °C and remnants of the furan rings coalesce. At this temperature fractured ether linkages form carbonyl groups, which closely resemble the original polymer, provide a framework for mesoporosity in the carbon, and allow for the rapid transport of gaseous decomposition products through the carbon. As the temperature is increased to 500 °C, the polymer remnants and carbonyl groups decompose, and the mesoporosity of the carbon collapses leaving only a nanoporous carbon.[9]

The spontaneous generation of nanoporosity resulting from the chemical decomposition of the polymer provides a unique opportunity to tune the resulting carbon structure by altering the conditions of the carbonization. Therefore, the purpose of this work is to examine the sensitivity of CSC carbons to PFA solvent and carbonization pressure. Following this reasoning, several synthesis conditions were selected to investigate the effect of processing on the nature of the resulting CSC material. To determine the sensitivity of carbon to the solvent used during the impregnation sequence, samples were prepared using benzene, toluene, and methanol as the furfuryl alcohol solvent.

Because the polymer liberates gaseous products as it is carbonized, CSC materials were also processed under vacuum, atmospheric pressure, and 5 atm of pressure. Performing the carbonization under vacuum may allow for more effective diffusion of the decomposition products from the material or it may increase the volume of the gaseous by-products. Likewise, processing the material under pressure may alter the nature of the resulting pore structure by compressing the gaseous by-products exiting the sample or activate the material by forcing nitrogen into the polymer.

Also, to place perspective on the role that the MCM-41 template is having on the formation of the nanoporosity of the sample, a material was prepared using a silica gel template in place of MCM-41.

3.2 Experimental section

Materials.

Tetramethylammonium hydroxide pentahydrate (TMAOH) (97%), tetramethylammonium silicate solution (TMASi) (99.99%, 15-20 wt % in water), sulfuric acid (95.0-98.0%), polyfurfuryl alcohol (99%), benzene (99%), aluminum chloride hydrate (99.999%), and toluene (99.5%) were all purchased from Sigma Aldrich. Hexadecyltrimethylammonium chloride (CTAC) (25%) in water solution was purchased from Pfaltz and Bauer. An ammonium hydroxide (29 wt %) water solution and Cab-O-Sil M5 were purchased from Fisher Scientific.

Cryogenic adsorption measurements were made with a Micromeritics ASAP 2010. X-ray diffraction data were gathered using a Scintag X_1 θ/θ automated powder diffractometer with Cu target, a Peltier-cooled solid-state detector, a zero background Si(510) support, and a copper X-ray tube as the radiation source.

Synthesis Method for CSC

The synthesis procedure for MCM-41 material was based on the work of others[10–12] and is the same as detailed previously.[1] MCM-41 was first impregnated with aluminum by mixing MCM-41 with an aqueous solution of aluminum chloride. The solution was stirred for 3 hours, and the products were then recovered by vacuum filtration, dried in a convection oven, and calcined in air at 540 °C. The aluminated MCM-41 was placed in a Teflon-lined autoclave containing an 80 % PFA in toluene solution. The impregnation solution was stirred for three days at room temperature. After stirring, the solution was statically heated for 24 hours at 80 °C. The key distinctions between each sample preparation are presented briefly in Table 3.2. For the synthesis of CSC-2, the product from the previous step was recovered via vacuum filtration and placed in a reaction vessel, which was then heated at 1 °C per minute to 150 °C and maintained at 150 °C for 6 hours under N_2. The sample was then heated at 5 °C per minute to 600 °C and maintained at 600 °C under N_2 for 3 hours. The synthesis of CSC-3 was the same as that for CSC-2 except the polymerization step at 150 °C and carbonization step at 600 °C were preformed under approximately a 9.2×10^{-5} atm vacuum. CSC-4 was synthesized the same as CSC-2 except the 150 °C and 600 °C steps were preformed under 5 atm of nitrogen. CSC-5 was prepared the same as CSC-2 except methanol was used as the furfuryl solvent. CSC-1 was prepared as documented in our previous work using benzene as the furfuryl solvent and following the synthesis steps outlined for CSC-2. Finally, the silica gel carbon composite, CSC-Si, was synthesized following the steps of CSC-2 except silica gel was used in place of MCM-41.

3.3 Results and Discussion

The base MCM-41 material used for impregnation is well ordered, has a narrow PSD centered at 38 Å, and approximately 900 m^2 of surface area. The material used in this work is the same material used previously;[1] therefore, the X-ray diffraction (XRD) plots, nitrogen adsorption data, and corresponding standard adsorption plot can be found in the original work.

The new CSC materials were characterized using XRD to ensure that the long range ordering of the parent MCM-41 was present in the carbon. All of the materials exhibit XRD patterns similar to the one shown in Figure 3.1 indicating the presence of long range ordering.

Nitrogen adsorption isotherms for these materials are shown in Figure 3.2. The Type I adsorption isotherms are consistent with materials that are completely

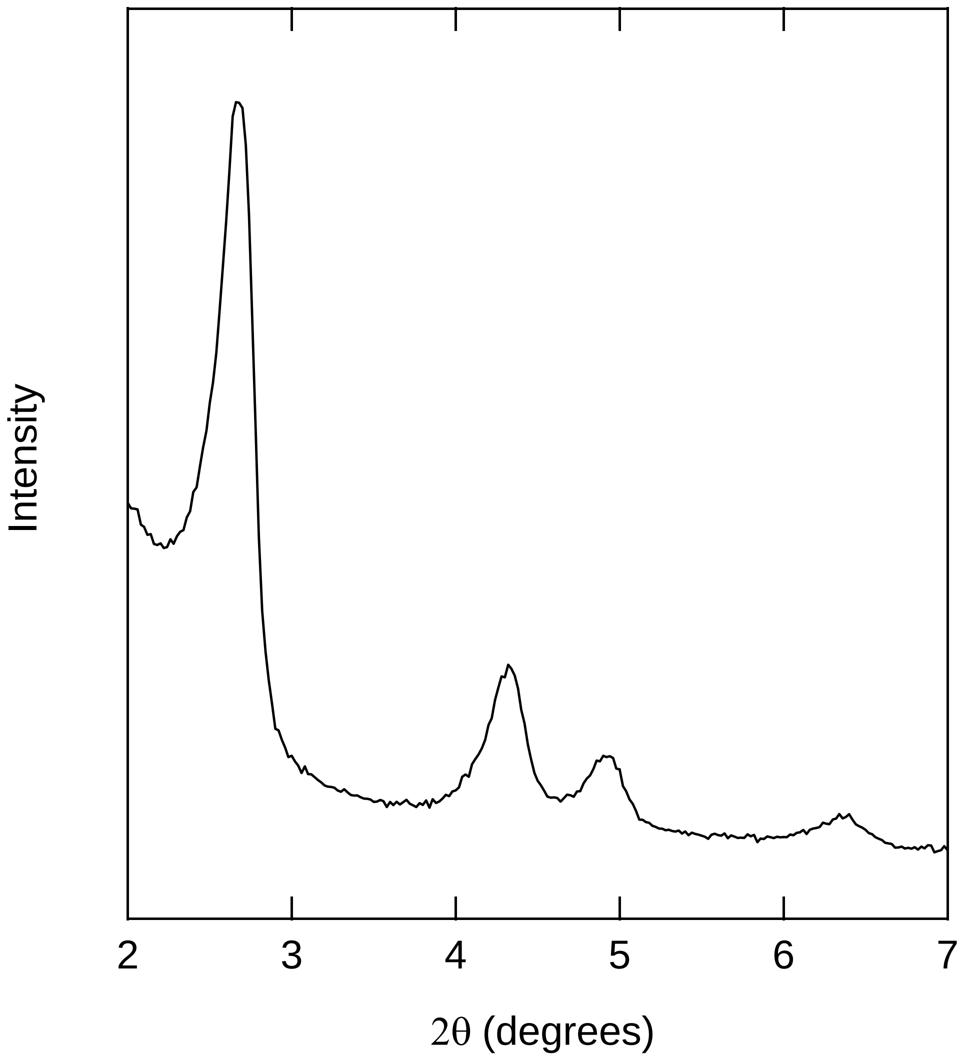

Figure 3.1: XRD pattern for CSC-2.

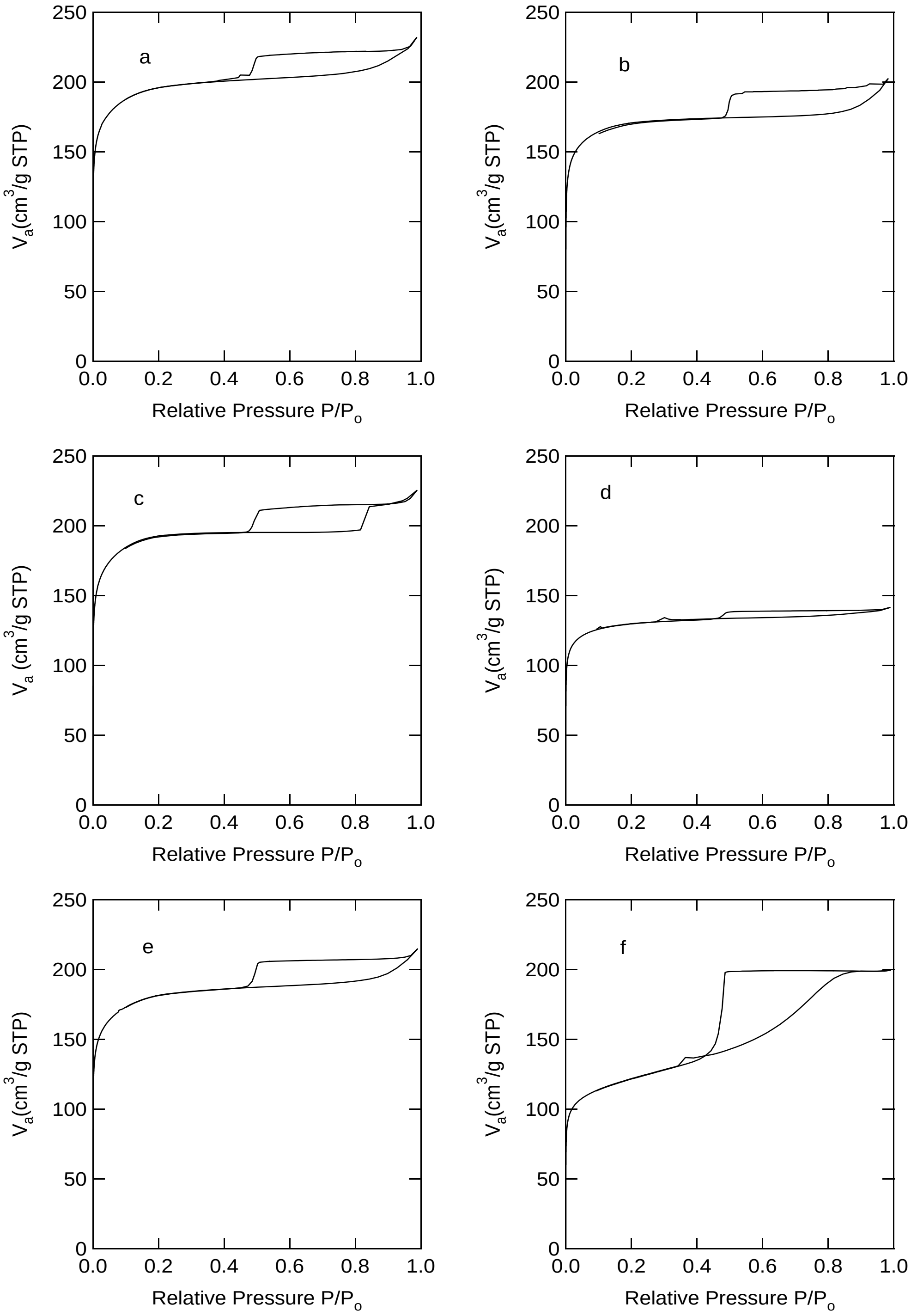

Figure 3.2: Nitrogen adsorption isotherm for CSC materials and parent MCM-41. (a) CSC-1 (b) CSC-2 (c) CSC-3 (d) CSC-4 (e) CSC-5 (f) CSC-Si

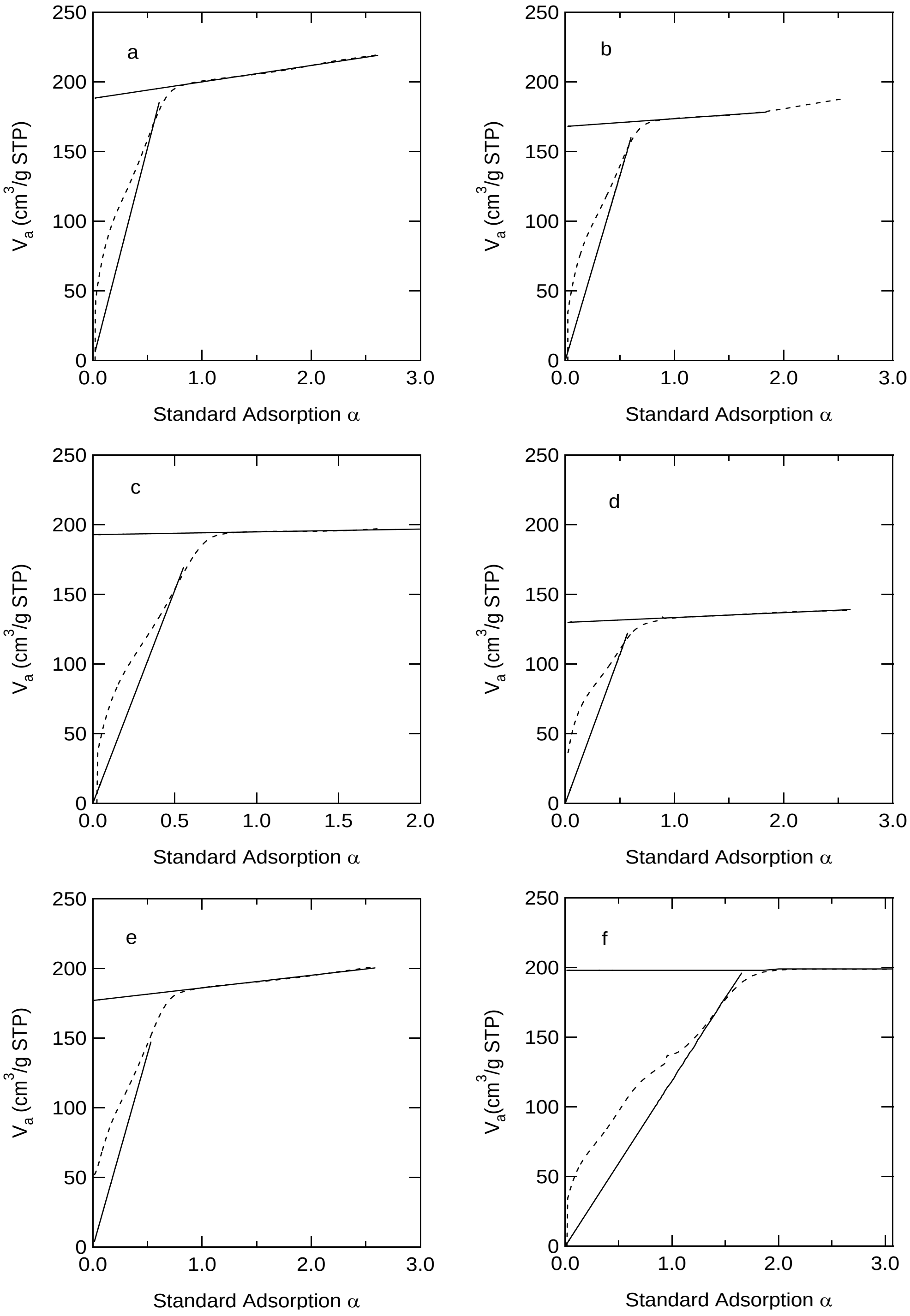

Figure 3.3: Standard adsorption plot of CSC materials. (a) CSC-1 (b) CSC-2 (c) CSC-3 (d) CSC-4 (e) CSC-5 (f) CSC-Si

nanoporous. Our initial work shows a material that maintains some residual mesoporosity as seen by the large linear portion of the isotherm beginning at approximately 0.2 relative pressure. However, all subsequently prepared CSC materials do not show the residual mesoporosity regardless of the preparation method. Also, the nanoporosity seen in the original work collapsed after a period of several weeks. This collapse decreased the surface area and left a purely nanoporous Type I isotherm similar to the isotherms and surface area reported in this work. Therefore, the isotherm in the original work shows intermediate CSC structure that still maintains some of the residual mesoporosity of the MCM-41 template. The lack of nanoporosity in the current CSC materials illustrates that these materials are more completely developed and structurally stable.

The surface area of these materials was affected by the processing conditions used during synthesis as illustrated in Table 3.2. Both CSC-2 and CSC-5, the materials prepared with toluene and methanol respectively, show a reduction in surface area relative to the material prepared using benzene. The effect illustrates that some control over the resulting carbon structure can be achieved by altering the PFA solvent used during synthesis.

Altering the pressure at which the carbonization and polymerization steps were performed had a stronger impact on the surface area than solvent effects. The results for CSC-4 show that performing polymerization and carbonization steps under pressure significantly inhibits the development of nanoporosity and surface area when compared to CSC-2, the material polymerized and carbonized under 1 atm of pressure. In fact, the surface area of CSC-4 is close to that of CSC-Si, the material prepared using silica gel instead of MCM-41. The reduced surface area of CSC-4 shows that these materials are not activated via a high pressure carbonization.

However, performing these steps under vacuum produced a material with a higher surface area than to CSC-2. In these particular samples, the material prepared under vacuum, CSC-3, has a surface area 230 m^2 higher than CSC-4, the material prepared under 5 atm of pressure. It is difficult to determine the mechanism by which pressure impacts the formation of PFA carbon. It is possible that performing the carbonization steps under vacuum helps to liberate gaseous byproducts from the material, and it is also likely that at low pressure the volume of the by-products expands and helps to activate the material. Also, as indicated later, under a vacuum the polymer and some of the resulting carbon may be removed from the MCM-41 structure. The removal of the PFA would result in the sample having a surface area closer to that of the base MCM-41. In either case, the results indicate that pressure can be used to adjust the properties of these materials.

The benefit of polymerizing PFA inside the pores of MCM-41 versus silica gel is well illustrated by the nearly 300 m^2 increase in surface area of CSC-1 over CSC-Si. The material developed using silica gel has a Type I isotherm consistent with a nanoporous sample, and the surface area of CSC-Si is approximately 180 m^2 higher than the parent silica gel. The increased surface area is the result of PFA forming a nanoporous carbon in the large mesopores of the silica gel. The nanoporosity of CSC-Si is significant because it illustrates that it is possible to form nanoporous PFA carbon inside the ordered and confined channels of MCM-41 as well as the large irregular silica gel mesopores.

The alpha plots shown in Figure 3.3 are consistent with materials that are completely nanoporous. These plots have been prepared using the same methods and reference materials as reported in our earlier work. All show nanoporous filling below α_s=0.5, indicating the presence of enhanced gas-solid interactions due to the overlap of attractive potentials of opposite nanopore walls.[14] Each of the materials, regardless of their preparation method, is fully-laden with nanopores. The solid linear segments in these plots illustrate the data that were used to calculate the material properties for each sample listed in Table 3.2.

Thermal gravimetric analysis studies of these materials were also performed, and the results are shown in Figure 3.4. PFA loads the MCM-41 near 40% by weight, which is close to the theoretical limit.[1] The fractional carbon loading of each material is shown in Table 3.1. CSC-3, the material prepared under vacuum, shows the least carbon loading implying that some polymer or carbon is removed during the carbonization. The material prepared using silica gel shows a greater weight loss than most of the materials prepared using MCM-41 due to the larger volumetric capacity of the silica gel. The material prepared under pressure also shows increased loading relative to other CSC materials. This large weight loss is interesting as it shows that pressure has an effect on the total carbon loading. It should be noted that CSC-4 has a carbon loading that slightly exceeds the theoretical max. One possible explanation for this is that the increased pressure is retarding the development and liberation of gaseous byproducts.

The HK pore size distribution of the CSC materials reported in this work all show nanoporous pore size distributions centered at approximately 5 Å. All of the CSC materials have nearly identical HK PSDs to the one shown in Figure 3.5. Although the HK method consistently reports PSDs of this type for nanoporous materials, the method has been shown to provide a reasonable estimate of the pore size and has been utilized by others to estimate the PSD of materials with pores near or less than 10 Å.[13,14]

To provide additional information about the pores contained in these materials, a PSD for each material was calculated using the nitrogen adsorption data and a carbon slit-pore density functional theory (DFT) model.[15,16] The results of these calculations are shown in Figure 3.6. All of the CSC materials have predominately 12 Å pores with some nanoporosity below 10 Å. The PSDs are all similar with the exception of the ones for CSC-4, the material prepared under pressure, and CSC-Si, the material prepared with silica gel in place of MCM-41. The PSD of CSC-4 is not

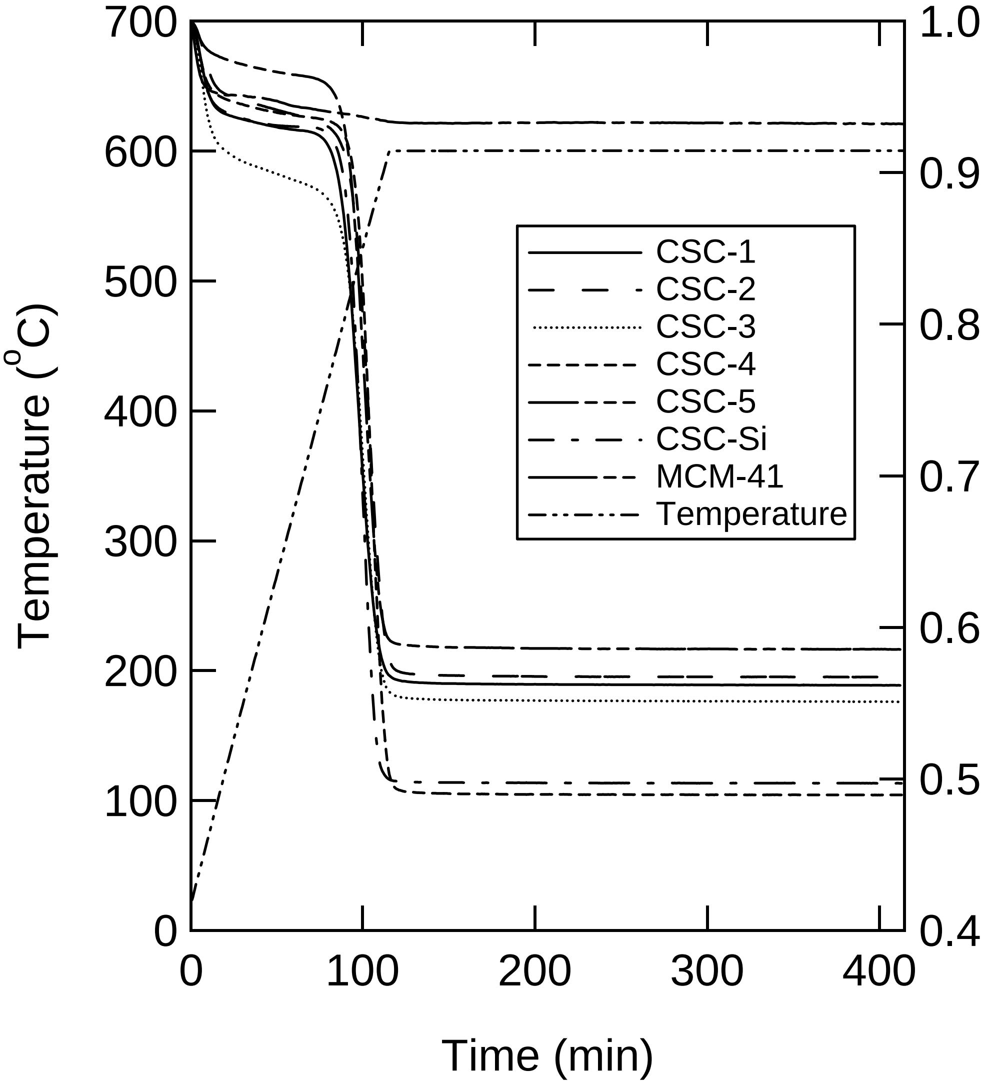

Figure 3.4: TGA profiles for CSC materials.

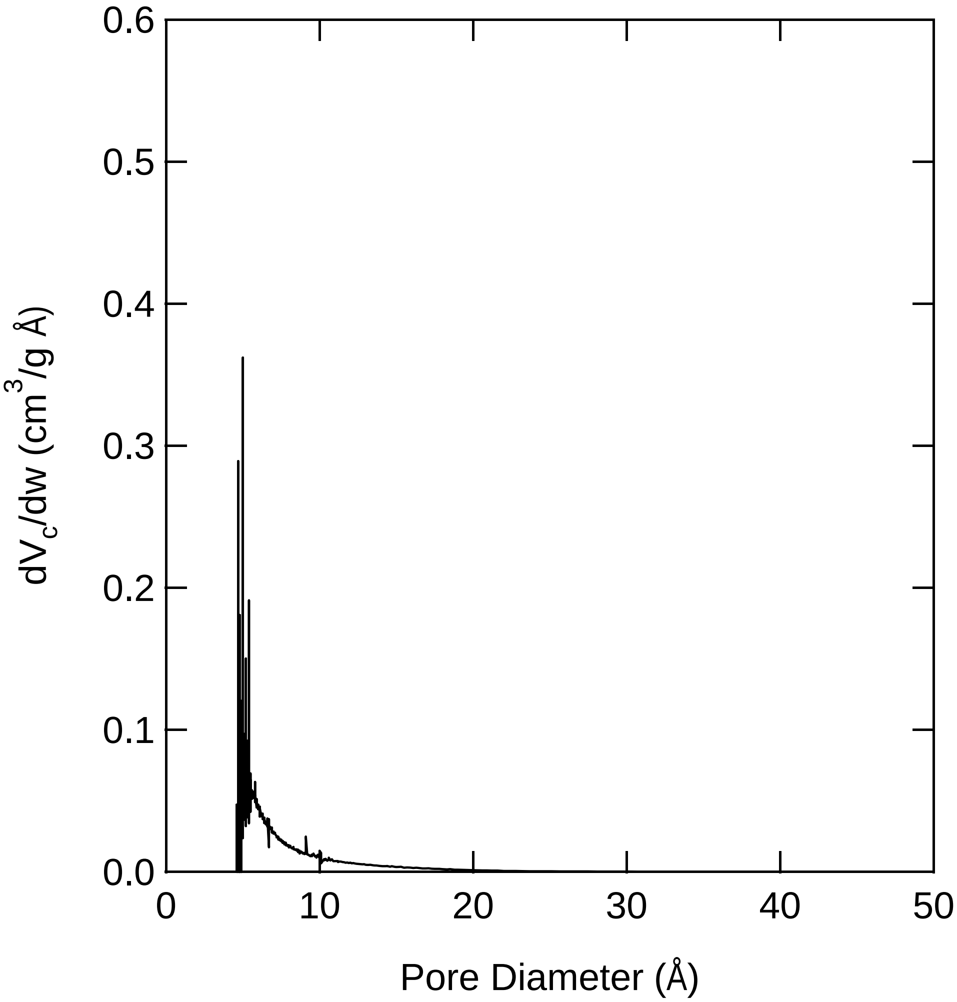

Figure 3.5: HK pore size distribution of CSC-2.

as clearly defined as the other CSC samples. The DFT PSD for CSC-Si shows pores at 12 Å as well as a distribution of mesopores centered near 67 Å that range between 30 and 130 Å, which are the result of the partial filling of the large (>100 Å) silica gel mesopores.

In order to determine the reliability of the impregnation procedure, and to provide a basis for the variance seen in the materials, a second MCM-41 sample was prepared and impregnated. This material has similar physical characteristics to the MCM-41 material used for the various processing runs that have been discussed. The MCM-41 material prepared had a 38 Å pore size when measured using the KJS method, a surface area of approximately 743 m^2/g, and was impregnated using the same procedure used to produce CSC-2. The resulting product has a 12 Å pore when measured using DFT and a surface area of 592 m^2/g. The carbon has approximately 80% of the surface area of the original parent MCM-41. CSC-2, likewise, has approximately 71% of the surface area of its parent MCM-41. The results shows that even when different MCM-41 source materials are used, the relative surface areas of two similarly prepared carbons are similar, in this case within 10% of one another.

While the CSC materials prepared in this work show nanoporosity when constructed using either MCM-41 or silica-gel, other investigations have shown that a mesoporous carbon can be prepared from PFA by using silica templates such as SBA-15 and MCM-48.[2,4,5,17] The carbons prepared in these other works make use of silica templates that are structurally different than MCM-41. In the case of SBA-15 the primary mesopores are generally larger (30–100 Å) than the ones contained in MCM-41 and they also possess nanoporous interconnects between the primary mesopore channels. The pore structure of MCM-48 is also different as its pores are three dimensional and interconnected. Currently, to the best of out knowledge all reported MCM-41 PFA impregnated structures have been nanoporous. The lack of developed mesoporosity from MCM-41 templated carbon and MCM-41 carbon composites

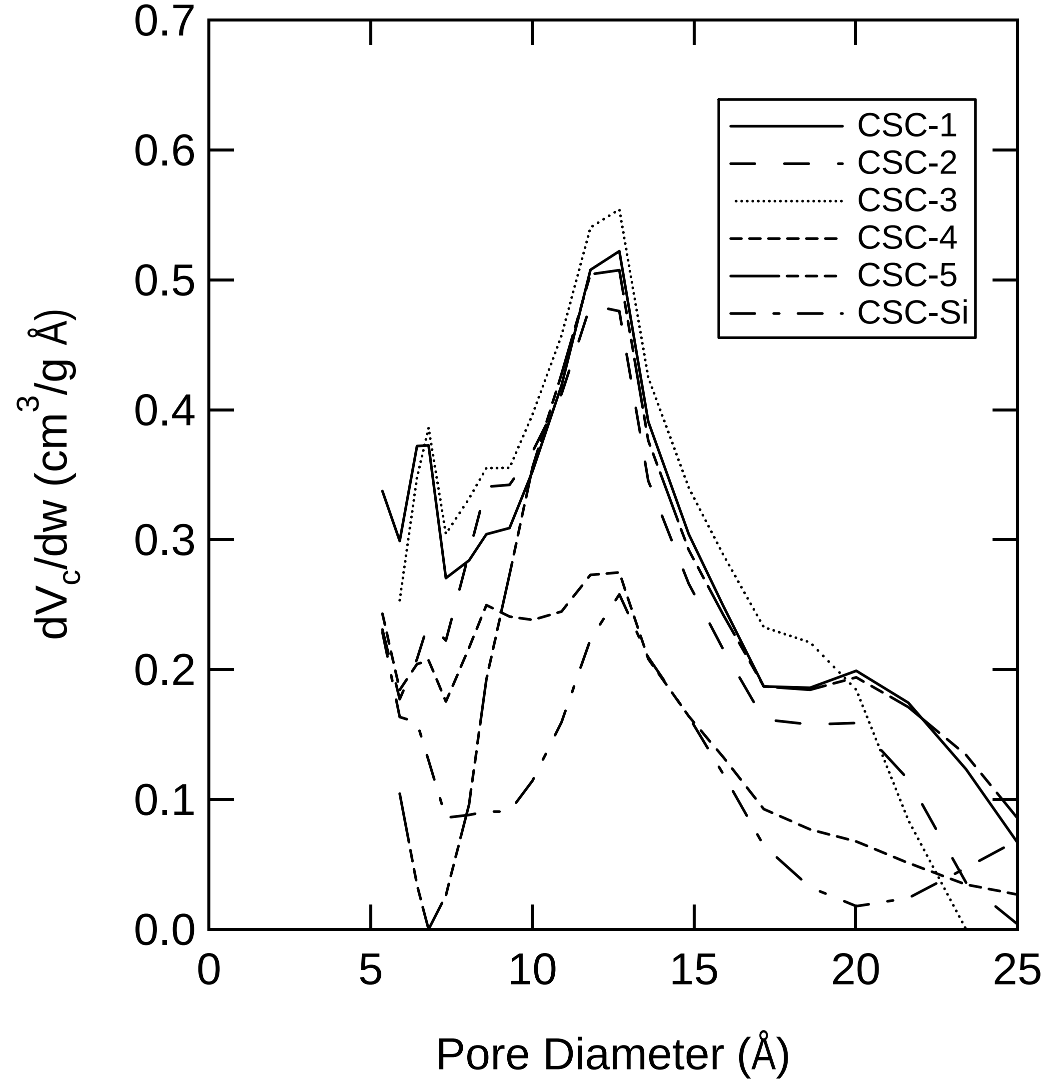

Figure 3.6: DFT pore size distribution of CSC materials.

could be the result of MCM-41 not having nanoporous interconnects between primary hexagonal channels, or it may be difficult to prevent the complete pore filling of MCM-41 by PFA. The works discussed above detailing the impregnation of MCM-48 and SBA-15 do mention intrinsic nanoporosity, porosity resulting from the carbon source alone and not mesoporosity resulting from lining the template, present in the carbon materials.

These materials have also been characterized by measuring adsorption isotherms for ethane at room temperature, and the results are shown in Figure 3.7. The adsorption isotherms were modeled well using the Freundlich isotherm

$$n = KP^m \tag{3.1}$$

where n is the loading in mol/kg, P is pressure in kPa, and K and m are model parameters, the values of which are listed in Table 3.1. The Figure shows that CSC materials prepared using benzene, methanol, and toluene adsorb similar amounts of ethane. The material prepared under vacuum, CSC-3, the material prepared under pressure, CSC-4, and the material prepared using silica gel, CSC-Si, all show reduced ethane loading. The material prepared under vacuum has a high surface area; however, as described earlier, preparing the material under vacuum removes some of the PFA and the impregnated carbon, which reduces the total carbon loading of the sample. This reduced carbon loading, in combination with the increased surface area, provides a plausible explanation for why CSC-4 adsorbs slightly less ethane than CSC-2. Likewise, the material prepared using silica gel maintains a large carbon loading; however, ethane adsorption is diminished due to its low surface area. Also, the material prepared under pressure shows the least amount of ethane loading, which further illustrates the detrimental effects pressure has on the development of porosity in the sample.

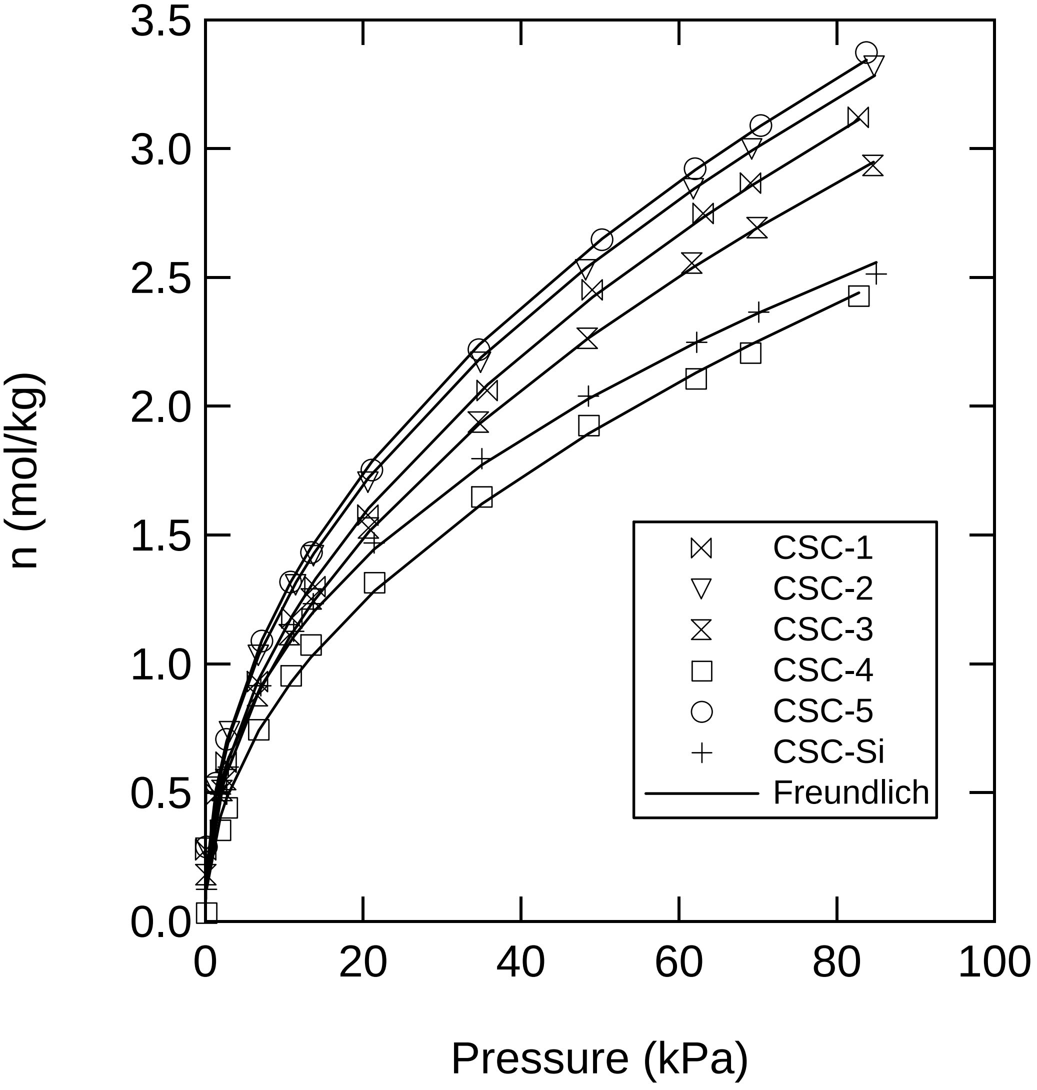

Figure 3.7: Ethane adsorption isotherms for CSC materials.

3.4 Conclusions

Several CSC materials have been synthesized and characterized, all of which possess a large surface area and regular pore size. The standard adsorption plots and adsorption isotherms show that these materials are completely nanoporous. The results illustrate that MCM-41 provides furfuryl alcohol a large surface area for polymerization and carbonization. The CSC material prepared under a moderate pressure shows a reduced surface area and pore structure relative to those prepared at atmospheric pressure. When the material is prepared under vacuum the surface area of the material is increased. Altering the solvent used during the MCM-41 impregnation has a more limited effect on the resulting CSC porosity. A nanoporous carbon prepared using a silica gel template illustrates that porosity can be formed both inside the well ordered and confined channels of MCM-41, as well as in the large and irregular pore structure of silica gel. The regularity of the nanopores contained in these materials and their high surface area make them reasonable candidates for adsorption separations.

Table 3.1: Freundlich isotherm parameters for CSC materials.

Sample	CSC-1	CSC-2	CSC-3	CSC-4	CSC-5	CSC-Si
K	0.377	0.431	0.553	0.299	0.446	0.406
m	0.478	0.457	0.474	0.476	0.455	0.414

Table 3.2: Physical properties of MCM-41 and CSC materials.

Sample	MCM-41	Si-Gel	CSC-1	CSC-2	CSC-3	CSC-4	CSC-5	CSC-Si
Solvent	–	–	benzene	toluene	toluene	toluene	methanol	toluene
Pressure (atm)	–	–	1	1	9.2×10^{-5}	5	1	1
S_{BET} (m^2/g)	910	260	740	650	730	500	680	440
C_{BET}	116	179	3302	1937	1361	2198	3588	4523
S_α (m^2/g)	800	–	830	730	800	590	760	320
S_{ext} (m^2/g)	92.7	–	51.5	24.3	8.80	15.4	39.4	1.40
S_{meso} (m^2/g)	710	–	–	–	–	–	–	–
V_{meso} (cm^3/g)	0.713	–	–	–	–	–	–	–
S_{nano} (m^2/g)	–	–	780	700	790	570	720	320
V_{nano} (cm^3/g)	–	–	0.291	0.260	0.299	0.201	0.274	0.306
V_{max} (cm^3/g)	0.952	1.11	0.359	0.313	0.349	0.219	0.332	0.309
d_{HK} (Å)	32.5	262	5.0	5.0	5.0	5.0	5.0	5.0
d_{KJS} (Å)	38.0	–	–	–	–	–	–	–
$d_{DFTslit}$(Å)	–	134	12	12	12	12	12	12,67
wt. fraction carbon	–	–	0.36	0.36	0.33	0.42	0.38	0.42

References

[1] Glover, T.G.; LeVan, M.D. *Micro. Meso. Maters.* (2007) in press.

[2] Kruk, M.; Jaroniec, M.; Ryoo, R.; Joo, S.H. *J. Phys. Chem. B.* 104 (2000) 7960.

[3] Lee, J.; Yoon, S.; Oh, S.M.; Shin, C.H.; Hyeon, T. *Adv. Mater.* 12 (2000) 359.

[4] Kruk, M.; Jaroniec, M.; Kim, T.W.; Ryoo, R. *Chem. Mater.* 15 (2003) 2815.

[5] Fuertes, A.B. *Micro. Meso. Maters.* 67 (2004) 273.

[6] Shiflett M.B.; Foley H.C. *Science* 285 (1999) 1902.

[7] Merritt A.; Rajagopalan R.; Foley H.C. *Carbon* 45 (2007) 1267.

[8] Shiflett M.B.; Pedrick J.F.; McLean S.R.; Subramoney S.; Foley H.C. *Adv. Mater.* 12 (2000) 21.

[9] Burket C.L.; Rajagopalan R.; Marencic A.P.; Dronvajjala K.; Foley H.C. *Carbon* 44 (2006) 2957.

[10] Chen, C.Y.; Li, X.H.; Davis, M.E. *Micro. Mater.* 2 (1993) 17.

[11] Chen, C.Y.; Burkett, S.L.; Li, H.X.; Davis, M.E. *Micro. Mater.* 2 (1993) 27.

[12] Edler, K.J.; White, J.W. *Chem. Mater.* 9 (1997) 1226.

[13] Lu A.H.,; Zheng J.T. *Carbon* 40 (2002) 1353.

[14] Kruk M.; Jaronic, M.; Choma J. *Carbon* 36 (1998) 1447.

[15] Olivier J.P.; *Carbon* 36 (1998) 1469.

[16] Olivier J.P.; *J. Porous Mater.* 2 (1995) 9.

[17] Sakintuna B.; Yurtum Y., *Ind. Eng. Chem. Res.* 44 (2005) 2893.

CHAPTER IV

DIFFUSION OF CONDENSABLE VAPORS IN SINGLE ADSORBENT PARTICLES MEASURED VIA CONCENTRATION-SWING FREQUENCY RESPONSE

4.1 Introduction

A wide variety of studies have been preformed to identify and mathematically model adsorption kinetics.[1–3] One problem of interest is characterizing the kinetics of adsorption of condensable vapors in various adsorbents. Detailed knowledge of the kinetics of vapors in carbon particles is important because a variety of filtration systems are used to adsorb organic vapors. Furthermore, the rate of adsorption of water by silica gel is also of significance due to the large scale industrial implementation of silica gel as a desiccant.

The adsorption of water in activated carbon has received a considerable amount of attention in the research literature. Dubinin and Serpinsky[4] presented one of the earliest models of water adsorption equilibrium in carbon particles that considered adsorption occurring via hydrogen bonds at active sites on the carbon surface. Talu and Meunier[5] developed a model to describe water adsorption by describing the adsorption of water as a series of sequential chain reactions to form water clusters. Do and Do[6] have developed a model that accounts for the microstructure of activated carbon by allowing for functional groups to be present at the edges of graphitic planes and considered water adsorbed in micropores in the form of a pentamer. Continuing this work, Furmaniak *et al.*[7] extended the model to account for the variation of the interaction energy between water molecules and surface active groups. Similarly, studies have also been conducted detailing the effect of surface oxidation and surface functional groups on water adsorption.[8–11] Recent molecular simulations have also detailed the adsorption of water in carbon slit pores of varying sizes. In these studies, the carbon surface is considered homogenous and pore interconnections are not accounted for. These works show that the pressure at which condensation occurs decreases with decreasing pore width to a limit near 6 Å, at which point, water clusters are constrained and high pressures are required to fill the pore.[12, 13]

The complexities associated with the adsorption equilibrium of water are also reflected in the adsorption kinetics of water in activated carbon. The studies documenting water adsorption kinetics in activated carbon are more limited than the ones detailing its equilibrium. Of particular interest is the pioneering work by Foley *et al.*[14] that describes the kinetics of water adsorption on carbon at different concentrations using a Glueckauf linear driving force (LDF) coefficient. They reported a minimum in the LDF coefficient as loading was increased. Following the interpretation of the adsorption equilibria, the kinetic results were interpreted based on water preferentially adsorbing at active sites and forming clusters.

While this study provided one of the first investigations of the kinetics of water on activated carbon, it was necessary to make several assumptions in the work. The diffusion mechanism for the system was assumed to be described well by a linear driving force model because this model had been used previously to describe the diffusion of water in carbon molecular sieves; however, results detailing the applicability of this model to a water-activated carbon system are not presented. Furthermore, the linear driving force model described in the work of Foley *et al.* assumes that the isotherm can be represented linearly for small changes in pressure, but some of the pressure changes in the work extend over a fairly large range of the isotherm. It is also assumed that the adsorption process is isothermal, and while the authors state that the temperature fluctuations where minimal, no evidence is presented that documents the thermal effects in the system. Moreover, two methods, one static and one flow-through, were used to acquire the kinetic data. When the uptake data gathered via the flow through method are plotted as $\ln(1 - \mathrm{M_t}/\mathrm{M_e})$ versus time, the data do not conform to a linear trend. In fact, three linear segments were identified for the extraction of the rate data. The authors attribute the discrepancy to the differences in the degas procedures of the static and flow through methods; however, the degassing methods appear adequate as the adsorption capacities are very similar. Therefore, another explanation is needed to describe the non-linear behavior observed. More sophisticated mass transport characterization methods, such as concentration-swing frequency response are now capable of addressing these concerns.

The work of Foley *et al.* was further extended in a subsequent study[15] detailing the adsorption kinetics of two different activated carbons. In this work, the rate of adsorption for a coconut-based carbon has a clear minimum as pressure is increased, whereas for wood-based carbon it decreases continually with increasing pressure. The unique adsorption kinetics of the materials are attributed to the differences in the adsorption isotherms as well as the differences in the concentration of primary adsorption sites on the surfaces of the carbons. This result is important because it illustrates that different types of activated carbon may exhibit noticeablly different mass transfer characteristics and possibly diffusion mechanisms. The minimum in diffusivity has also been investigated by Cossarutto *et al.*[16] who also described the adsorption of water vapor using the LDF model, assumed the system to be isothermal, and used a gravimetric uptake method to gather their kinetic data. The work is similar to the work of Foley *et al.* and showed the adsorption kinetics to have a clear minimum in the rate constant as pressure is increased. Likewise, the minimum in adsorption kinetics has been documented by Qi *et al.*,[17] who also used an LDF model, in an examination of the diffusion of water on BPL activated carbon.

In addition to studies on the adsorption of water on activated carbon, several authors have detailed the adsorption of condensable organic vapors on activated carbon.[18–33] For example, Do and coworkers[18–25] have published several studies concerning the diffusion and permeability of vapors such as benzene, hexane, toluene, and ethanol in activated carbon, detailed the use of constant molar flow semi-batch methods to determine adsorption kinetics, and performed extensive studies concerning the permeability of vapors on carbons including an examination of the relationship between the Darken equation and permeability.

Using a differential transient permeation method, Do *et al.*[19] completed a study of the diffusion of hydrocarbons in activated carbon in which they found that hexane diffusion was described well by the Darken model. In particular, they state that while activated carbon is a highly heterogeneous surface, large hexane molecules experience a more uniform homogenous surface, whereas smaller molecules, such as propane and butane, encounter a higher degree of heterogeneity for surface diffusion. The authors attribute these effects to the interaction of large hexane molecules with several surface sites of varying energy simultaneously, whereas smaller molecules interact with high energy sites first and lower energy sites only as loading increases.

Prasetyo et al.,[26] using a constant molar flow method, quantified the dependence of surface diffusion on loading of strongly adsorbing vapors at different temperatures on activated carbon and found that for the vapors studied, surface diffusion increases rapidly with loading. In other work, Do *et al.*[27] found agreement between the surface diffusivity of hexane on activated carbon as determined by a constant molar flow and differential permeation methods and provide a range for the surface diffusivity for a range of loadings of hexane in activated carbon.

Yang and Kapoor[33] found the interesting result that when the surface diffusivity at zero loading for hexane adsorption in activated carbon is extracted from a model without considering the concentration dependence of the data, the resulting diffusivity is two to three times higher than as predicted by the concentration dependent model.

The diffusion of water on silica gel has also received attention in the literature. For example, Suzuki and Chihara estimated the diffusion of water vapor on silica gel using a gravimetric method by assuming that surface diffusion is the controlling diffusion mechanism.[34] Other authors have examined this system using gravimetric methods and found thermal effects to be significant under specific adsorption conditions.[35,36] Rajniak and Yang,[37] who also used a gravimetric uptake method, predicted the concentration dependence of the effective diffusivity of water vapor on silica gel in the range where capillary condensation and adsorption hysteresis occur. Studies have also examined other aspects of the diffusion of water in silica gel, such as examining the significance of diffusion occurring on the surface of the silica gel versus in the core of the particle, as well as the dependence of diffusion on the pore size of the material.[38,39]

In addition to the methods discussed above, frequency response methods have also been used to measure the diffusion of condensable vapors in adsorbent materials.[40–44] Of the available types of frequency response methods, flow-through frequency response systems are appealing as they minimize heat effects and thereby allowing the system to often be treated isothermally. The development and application of frequency response (FR) methods to determine adsorption kinetics is reviewed in papers by LeVan *et al.*[45–50] Among these works is the development of a novel flow-through concentration-swing FR apparatus that perturbs the concentration of the system sinusoidally while maintaining a constant flow rate.[45] The model developed for the concentration swing apparatus is similar to the model used to describe the dynamics of their pressure swing frequency response apparatus.[46–48] It should be noted that most of the FR works discussed above assume that small perturbations to the system allow for portions of the kinetic model to be linearized. However, several studies have investigated nonlinear kinetic modeling of FR data.[51–57]

The purpose of this work is to utilize concentration-swing frequency response to determine and quantify the appropriate mechanism that describes the mass transport phenomena of condensable vapors in common adsorbent particles. This is the first application of concentration-swing frequency response to characterize the diffusion of condensable vapors in adsorbent particles. We pay particular attention to the kinetics associated with the adsorption of water in BPL activated carbon, the dependence of the diffusivity on concentration, and the applicability of the Darken equation. The results detailing the adsorption of water in BPL activated carbon will be contrasted with a rate study of the adsorption of hexane on BPL activated carbon and water on silica gel. In each case, the diffusion mechanism will be identified and diffusivity data presented. This work is unique in that it is, to the best of our knowledge, the first to focus on not only identifying the adsorption mechanism of water in BPL activated carbon and silica gel, but also the first to explore the applicability of the Darken relationship to a water-BPL activated carbon system.

4.2 CSFR System and Mathematical Model

The CSFR system of Wang and LeVan[45] was modified to accept a saturated vapor inlet stream. A schematic of the apparatus is shown in figure 4.1. Sparging vessels were placed in series in a temperature controlled water bath operating at subambient temperature to generate a saturated vapor. The pressure was controlled by a pressure controller upstream of the spargers, and helium was used as an inert carrier gas for the vapor.

One key modification that has been made to the system is a reduction in the total bed volume. Specifically, this feature allows for the collection of kinetic data on a single adsorbent particle. For the BPL activated carbon-water system the adsorbent particle had a mass of 5.5 mg, the BPL activated carbon-hexane system adsorbent particle mass was 4.7 mg, and the mass of the adsorbent particle used in the silica gel experiments was 1.3 mg. The small sample holder makes this method ideal for the characterization of materials that may exist in small quantities, such as novel adsorbent materials. While it is also possible to place a small particle in a large bed

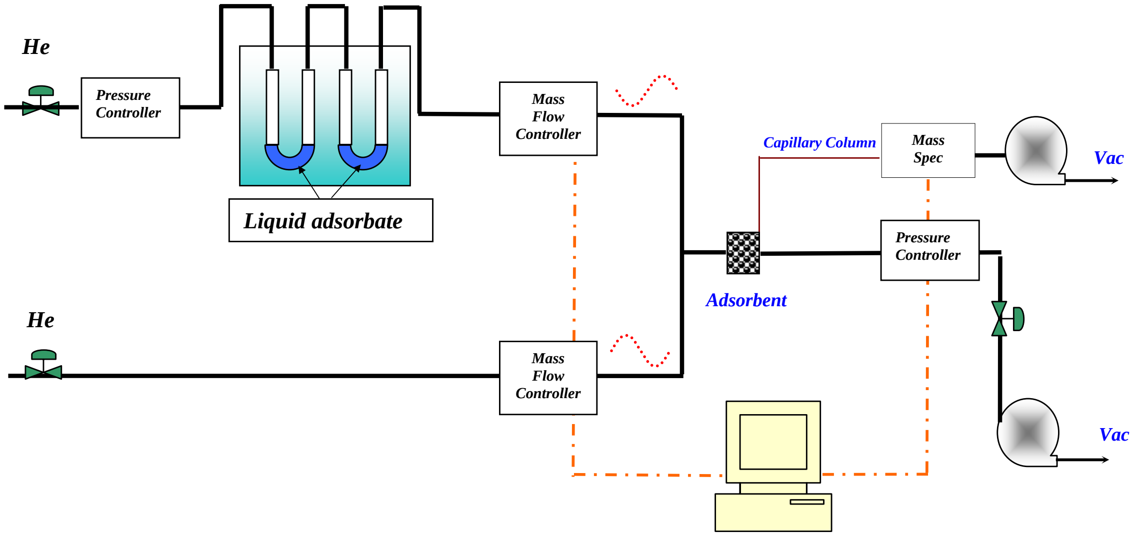

Figure 4.1: Concentration-swing frequency response apparatus for measurement of diffusion of condensable vapors.

volume, this leads to a large void space in the bed that may reduce the accuracy of the measurements. Also, utilizing a small adsorbent bed has been shown to eliminate axial dispersion effects which results in a simpler mathematical model of the system,[58] and as will be discussed later, the single particle adsorbent bed, in combination with a flow through design, reduces thermal effects present in the system. All measurements were performed at 25 ± 1 °C. We used BPL activated carbon Lot No. 4814-J from the Calgon Carbon Corporation and Davison Grade 40 silica gel. This is important to note as activated carbons and silica gels of different types may exhibit different diffusion mechanisms and mass transport rates.

The mathematical model for this system has been described by Wang and LeVan,[45] and the kinetic rate equations are given by Wang *et al.*[48] For our experiments, the kinetics will be modeled with either a nanopore diffusion (surface diffusion) or LDF model. Briefly, for one adsorbable component and spherical geometry the surface diffusion model can be expressed as

$$\begin{aligned} &\frac{\partial n}{\partial t} = \frac{D}{r^2}\frac{\partial}{\partial r}\left(r^2\frac{\partial n}{\partial r}\right) & \\ &n = n^* & \text{at } r = R \\ &\frac{\partial n}{\partial r} = 0 & \text{at } r = 0 \end{aligned} \tag{4.1}$$

where n is the adsorbate concentration in the micropore, $n^*(P)$ is the equilibrium adsorbate concentration in the equilibrium state, R is the radial coordinate for the microparticle, D is diffusivity, and t is time. External mass transfer can also be included in the model and is written as

$$\rho_b \frac{dn}{dt} = k_f a(c - c_s^*) \tag{4.2}$$

where k_f is the external mass transfer coefficient, c and c_s^* are the adsorbate concentrations in the bulk and at the fluid-pellet interface, and a is the specific surface area.

The linear driving force model is written as

$$\frac{dn}{dt} = k(n^* - n) \tag{4.3}$$

where k is the linear driving force mass transfer coefficient. Because the perturbation in concentration is small, the isotherm is linearized and written

$$n^* = n_{ref} + K(P - P_{ref}) \tag{4.4}$$

where K is the local slope of the isotherm. Therefore, care was taken to ensure that only small perturbations were made to the vapor concentration, and in most cases these perturbations were less than 10%. In some cases, the mass transport will be modeled using a non-isothermal surface diffusion model and the thermal effects investigated using an energy balance, as has been described in detail elsewhere.[50,58]

Following the method outlined previously, a total transfer function for the system is written for each kinetic model. The total concentration of the adsorbate component is perturbed using a sine wave and the resulting response of the system is characterized using the amplitude of the output. A plot of amplitude ratio (outlet over inlet) at specific frequencies is created, and the model is then used to determine the controlling mechanism and the kinetic parameters. With detailed diffusivity data at various loadings, it is possible to examine the relevance of the Darken equation for the cases studied. The Darken relationship can be written as

$$D = D_0 \frac{d \ln P}{d \ln n} \tag{4.5}$$

where D_0 is the corrected diffusivity. Thus, with an isotherm for the system of interest it is possible to calculate $d \ln P/d \ln n$, the thermodynamic correction factor, and use an experimental value of the diffusivity at a particular pressure to determine D_0.

4.3 Results and Discussion

Water Diffusion in BPL Activated Carbon

A distinct advantage of using FR methods is the capability to distinguish between mechanisms of adsorption. The transfer functions used to describe the system are derived based on a particular adsorption mechanism, and thus each mechanism produces a different transfer function with which to model the response.

This approach is illustrated in figure 4.2, which shows the amplitude ratio plotted versus frequency. The data shown are for the adsorption of water in BPL activated carbon at partial pressures of 0.64 kPa and 1.72 kPa. Also plotted in this figure is the control experiment, which is the response of the system without adsorbent material. The figure shows both the nanopore diffusion model of equation 4.1 and the Glueckauf linear driving force model of equation 4.3. The nanopore diffusion (ND) model passes through nearly every data point, whereas the LDF model has a shape that is inconsistent with the data. While the LDF model is unable to describe the data at either pressure, the LDF model describes the data at 1.72 kPa better than the data at 0.64 kPa. Continuing this idea, figure 4.3 shows that both the LDF and the ND models are able to describe the data at 2.39 kPa. In these experiments frequency response plots at each pressure were characterized using both models, and it was found that the LDF model is only able to describe the data at pressures of 1.93 kPa and above. Therefore, the ND model is the appropriate model to describe the diffusion of water in BPL activated carbon. The results are shown in figures 4.4 and 4.5 which show the frequency response plots and ND model passing through nearly every data point at each of the pressures measured.

The data were also modeled using a combined external film mass transfer resistance and ND model. The extracted external mass transfer coefficients were large enough such that they essentially eliminated the impact of the film resistance from the model. Also, inclusion of the external film resistance did not alter the quality of the fit, and the extracted diffusivities for this system were the same as those extracted when only the ND model was used.

These results are in contrast to previous works; however, the applicability of the ND model should not be extended to all activated carbons blindly as different carbon sources and activation methods may yield different mass transfer mechanisms. For example, carbon molecular sieves, which have a constrained pore opening, exhibit behavior consistent with an LDF mechanism. Likewise, the carbons used by Foley and coworkers[14–16] may be more accurately described using an LDF mechanism depending on the nature of the porosity in the carbon.

To investigate thermal effects present in the system, the data at 1.72 kPa were modeled using both the ND model and the non-isothermal ND model and the results are shown in figure 4.6. This particular pressure was selected because the isotherm is steeper at this pressure than any of the other pressures examined and therefore should produce the largest change in temperature for a change in loading. The two models are nearly indistinguishable from one another and both provide nearly identical diffusivities. Using the energy balance discussed previously, the remaining pressures were investigated to determine the change in temperature as a result of the perturbation in pressure. The maximum predicted change in temperature was determined to be 0.03 K and occurred at 1.72 kPa, and nearly all other pressures were predicted to have a temperature change near 0.005 K. With both the non-isothermal and isothermal models yielding similar results, as well as the small changes in temperature with loading, the system can be properly identified as isothermal.

Furthermore, the results shown in figure 4.4 show that as the water pressure is increased the curves move to lower frequencies. This effect is the result of a decrease in the mass transfer rates in the system with increasing pressure. The decrease continues as pressure is increased until a minimum is reached at approximately 1.72

kPa, at which point, the curves progress back toward faster frequencies as shown in figure 4.5. The frequency response plots show a clear minimum in the kinetics occurring at approximately 1.72 kPa.

When the diffusivities are extracted from the model and plotted versus loading, as seen in figure 4.7, the unique diffusion characteristics of water on BPL activated carbon become more apparent. This plot clearly shows a minimum in the diffusivity occurring at approximately 5 mol/kg loading. This unique behavior is consistent with previous kinetic studies of water carbon systems[14–17] even though the transport models used to describe the system are substantially different. Specifically, Foley *et al.*[14] reported a minimum occurring in the range of 1.22 to 1.52 kPa which is consistent with minimum occurring at 1.72 kPa as reported in this work. The diffusivities corresponding to each pressure are listed in table 4.1.

These results are also consistent with the mechanism of water adsorption discussed in the introduction. The first region shown in figure 4.7, spanning loadings from zero to approximately 5 mol/kg, corresponds to the adsorption of water at active sites on the carbon surface. The minimum in adsorption diffusivity occurs as water clusters form around the active sites. Beyond the minimum, the adsorption rate increases as water clusters are formed that are large enough to begin to fill the pores of the carbon.[16] The adsorption of water via a clustering phenomena at active sites results in the adsorption isotherm having a very steep segment. For example, the water adsorption isotherm for BPL as reported by Qi *et al.*[17] shows a rapid increase in loading for small changes in pressure near relative pressures of approximately 0.5 P/P_o.

To evaluate the applicability of the Darken equation to this system, the isotherm reported by Qi *et al.*[17] was used to evaluate the thermodynamic correction factor, and the data at 1.96 kPa were used to extract a constant corrected diffusivity. Therefore, the measured diffusivity and the diffusivity predicted with the Darken relationship at

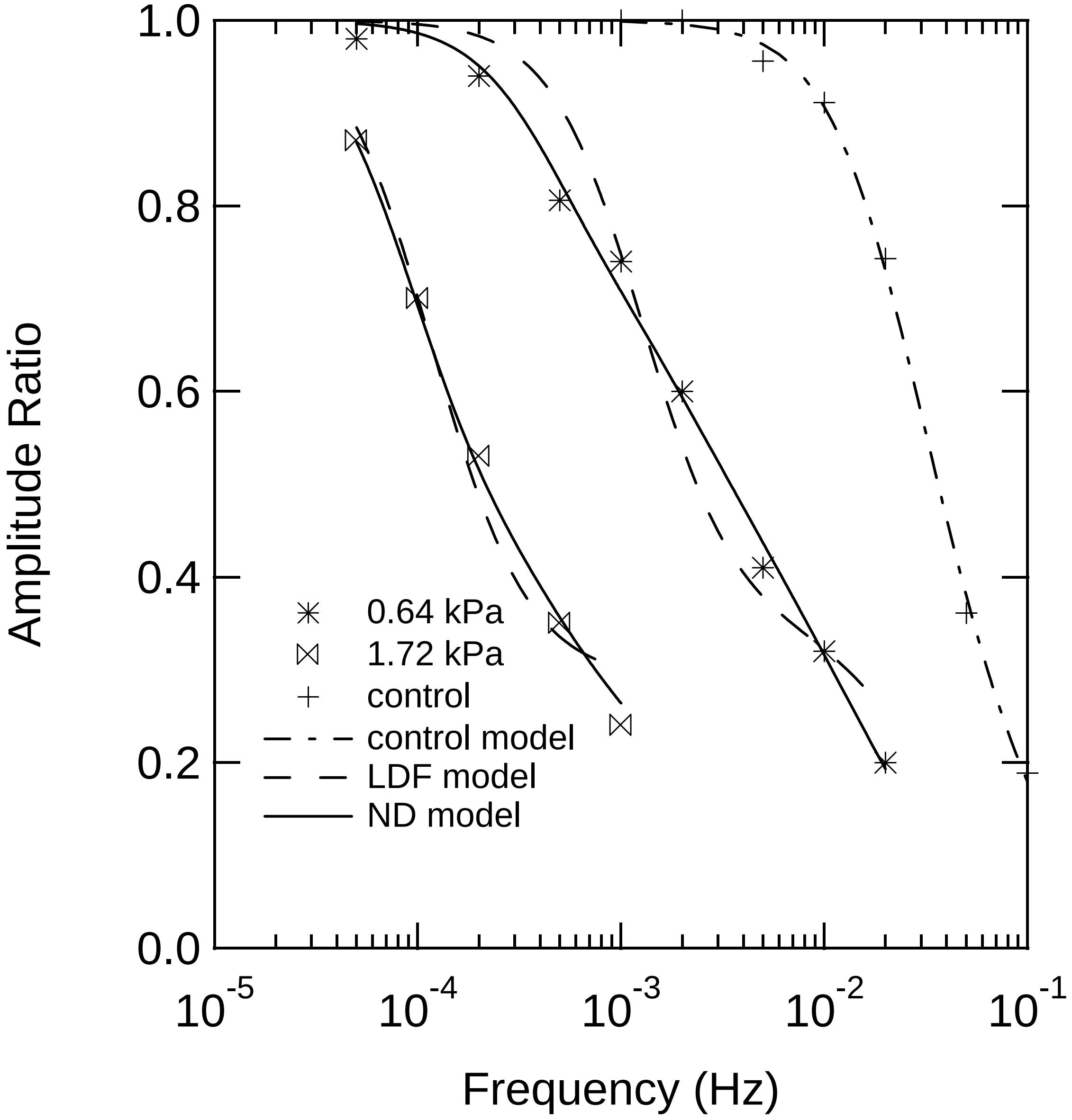

Figure 4.2: Frequency response plot of water adsorption in BPL activated carbon at two pressures and the nanopore diffusion and linear driving force models

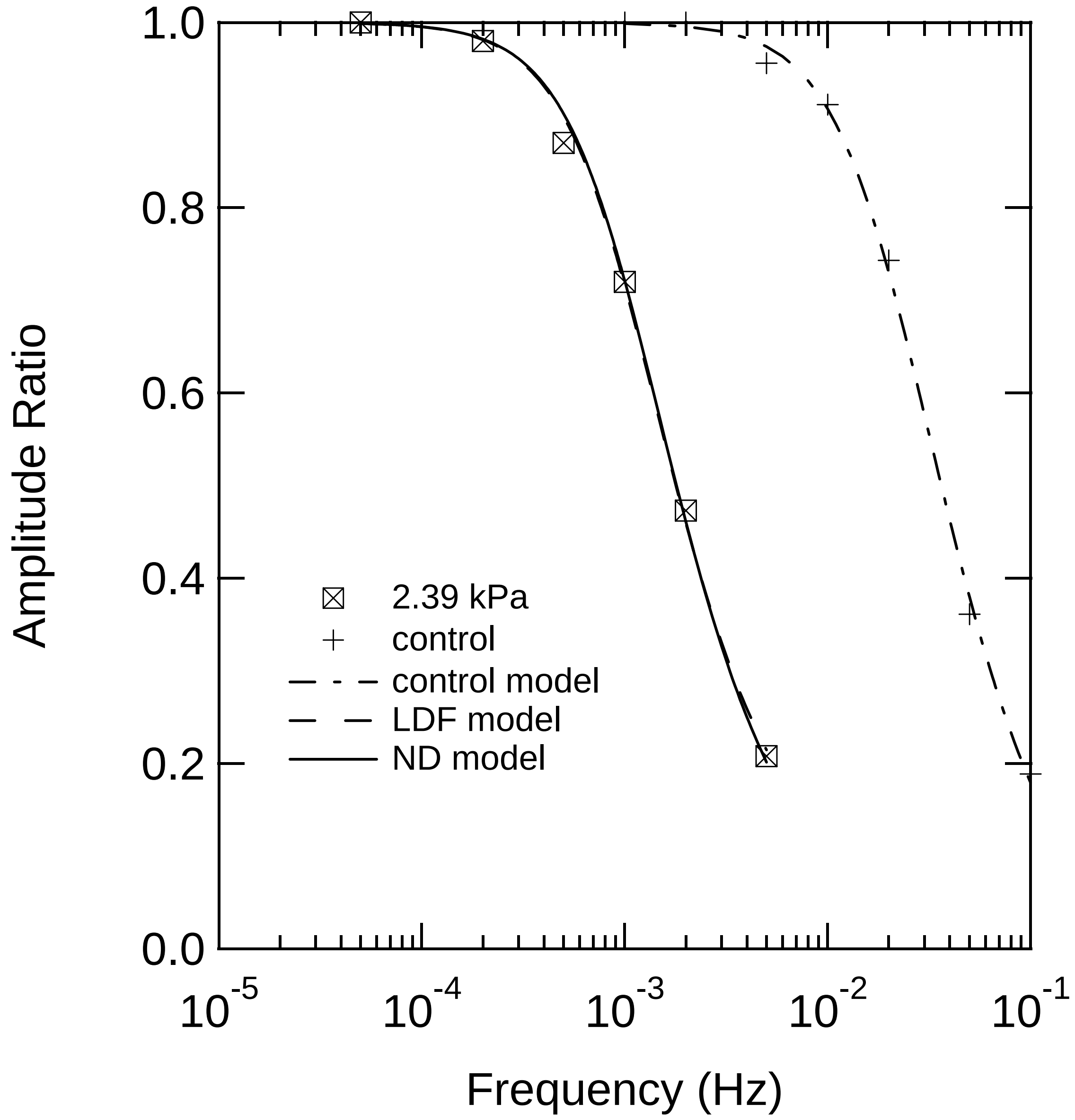

Figure 4.3: Frequency response plot of water adsorption in BPL activated carbon at high water pressures and the linear driving force model and nanopore diffusion models

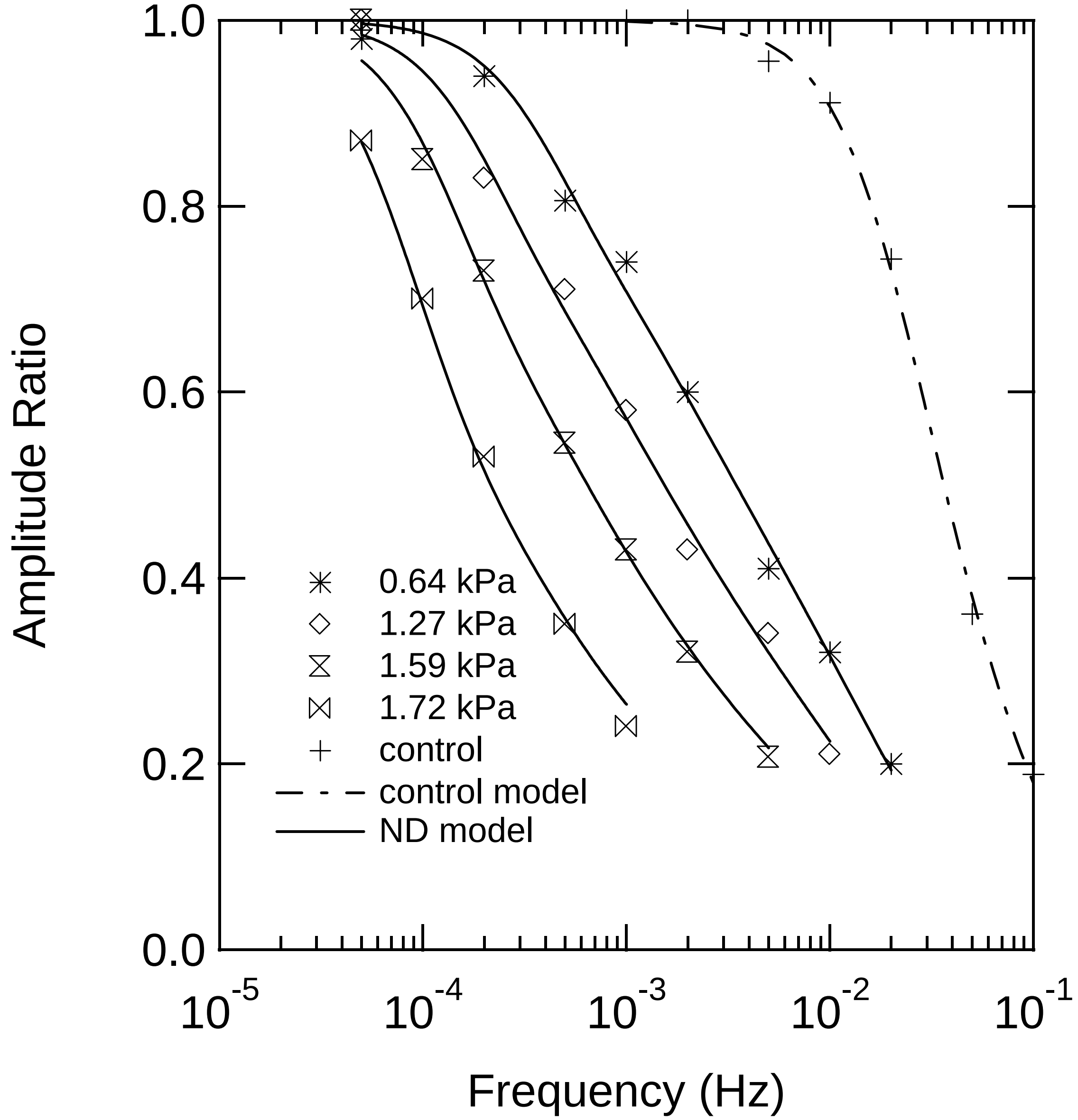

Figure 4.4: Frequency response plot of water adsorption in BPL activated carbon at low water pressures

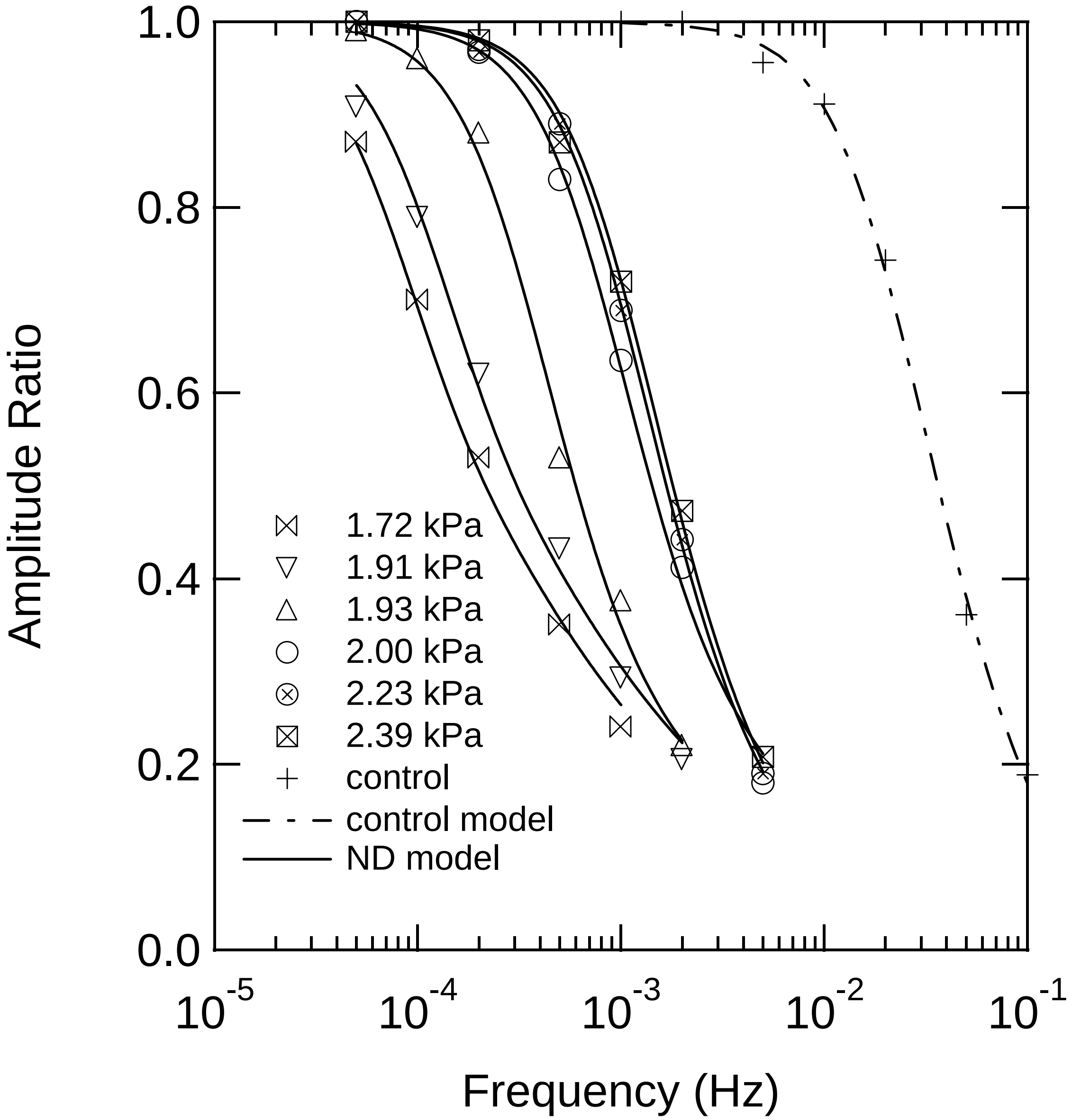

Figure 4.5: Frequency response plot of water adsorption in BPL activated carbon at high water pressures

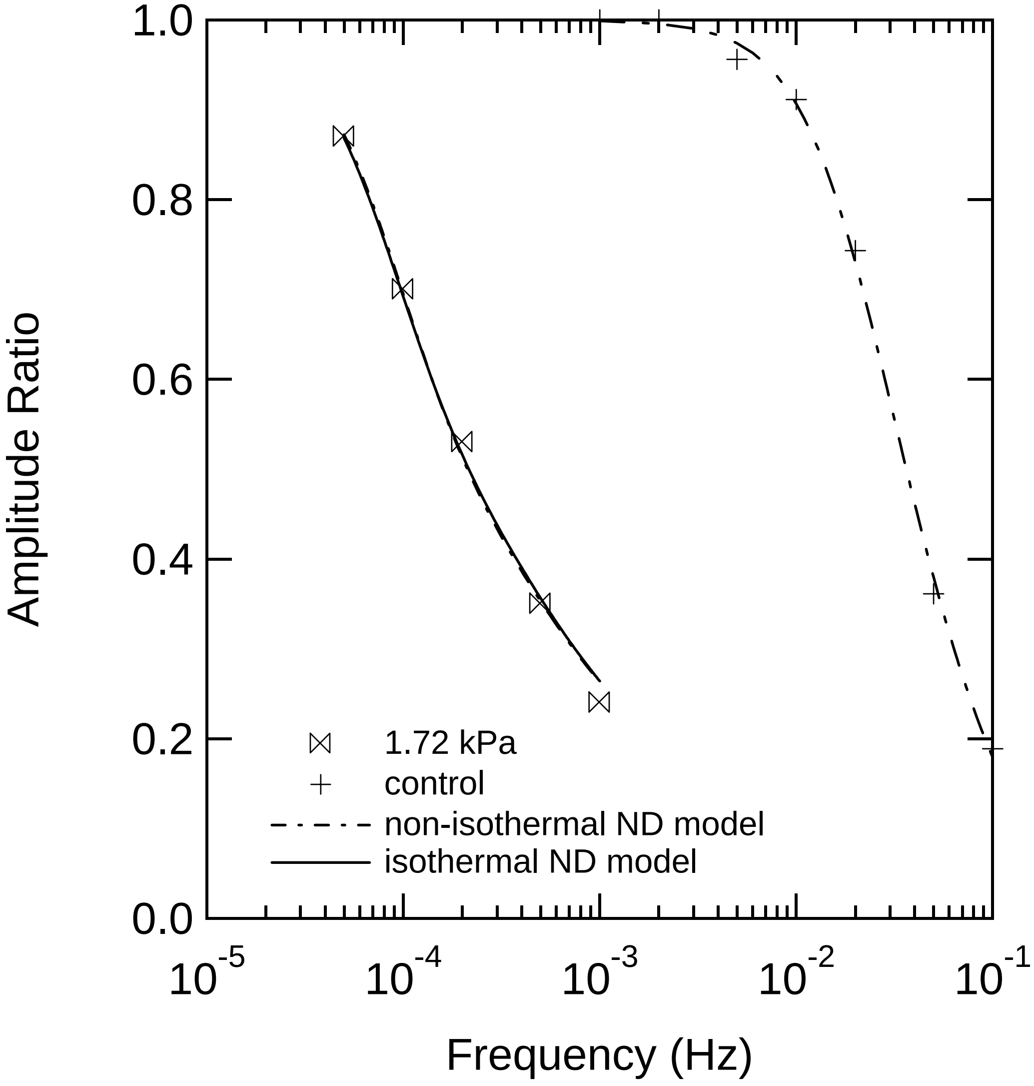

Figure 4.6: Frequency response plot of the adsorption of water in BPL activated carbon and the isothermal and non-isothermal ND models.

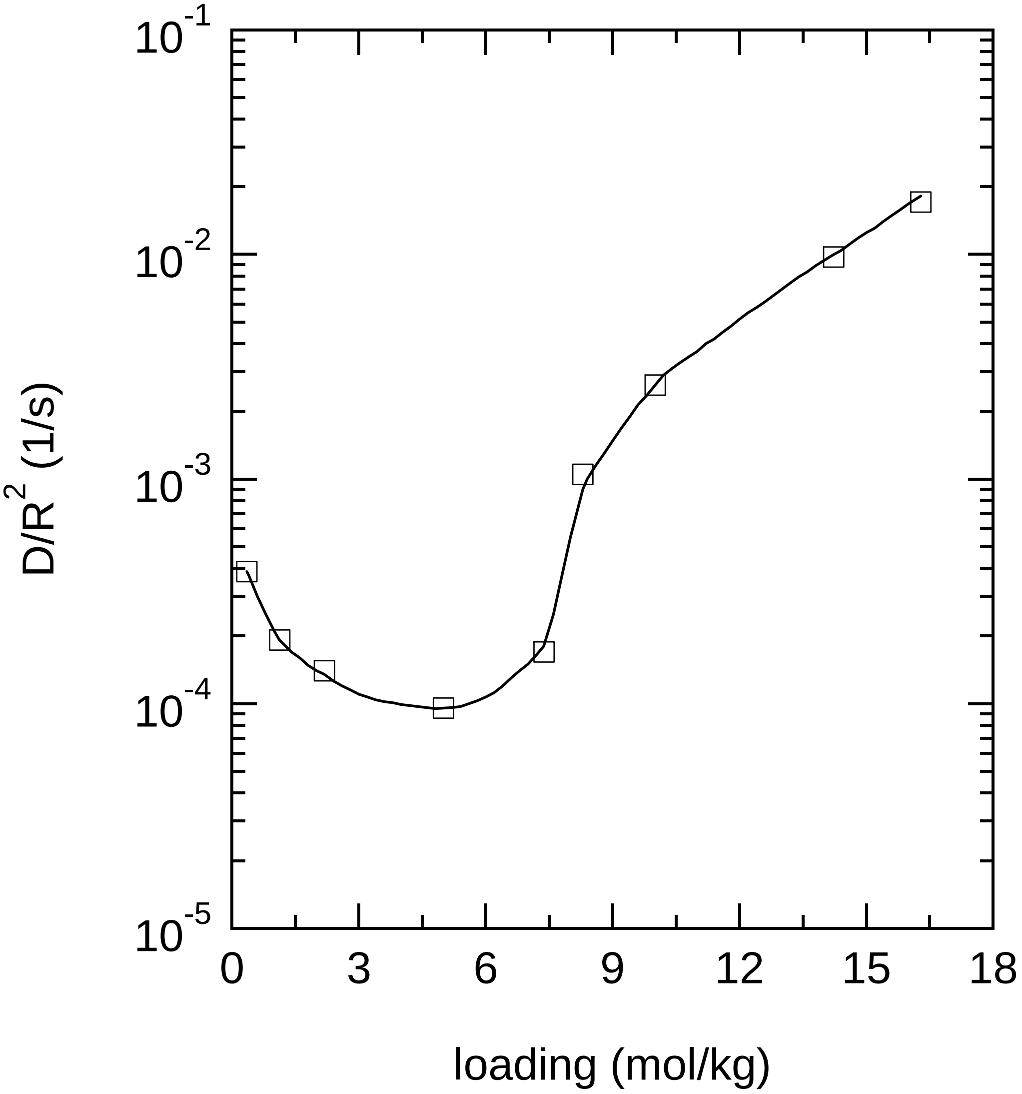

Figure 4.7: Diffusivity of water versus loading. The curve through the data is a guide for the eye only.

1.96 kPa are equal. As indicated in table 4.1, the Darken relationship fails to predict the complex water adsorption kinetics. In particular, the Darken relation agrees with the low pressure data qualitatively; however, as the pressure and the slope of the isotherm begins to increase the relationship fails.

Hexane Diffusion in BPL Activated Carbon

Following the same procedure discussed above, the adsorption of hexane in BPL activated carbon was also examined at several different concentrations. The data used to identify the mechanism of this system are displayed in figures 4.8 and 4.9 and the diffusivities and LDF coefficients are tabulated in table 4.2. The figure shows the data can be described by both the LDF and the ND models. Specifically, the small differences in the shape of the curves for the models are not extensive enough to invalidate the description of this system by either model. The data were also modeled using a combine ND and external film resistance model to evaluate the impact of the film resistance on the data set. It was found that the extracted external film coefficients essentially eliminated this resistance from the model, and that the diffusivity extracted from the combined resistance model and the ND model alone were essentially the same.

To determine the thermal effects present in the system, the 13.3 kPa data were fit to the non-isothermal ND model. As before, the isothermal and non-isothermal models are indistinguishable from one another and the reported diffusivity values were nearly identical; furthermore, the predicted change in temperature at each pressure was found to be approximately 0.006 K, which justifies the application of the isothermal model to the system.

Moreover, in contrast to the adsorption of water on BPL, the adsorption of hexane on activated carbon is more accurately described by the Darken relationship as shown by the data in table 4.2; while not exact, the data are in the range predicted

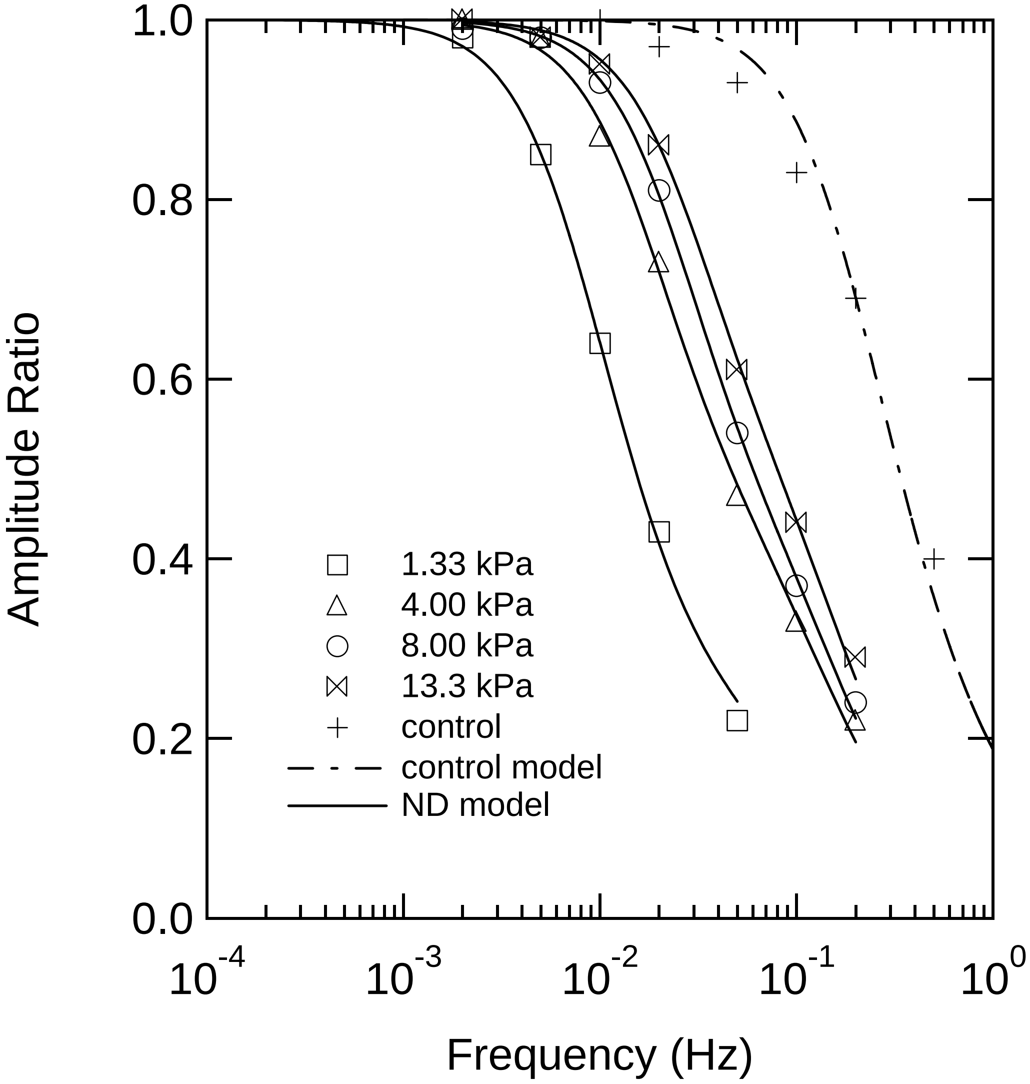

Figure 4.8: Frequency response plot of the adsorption of hexane in BPL activated carbon at various hexane pressures and the nanopore diffusion model

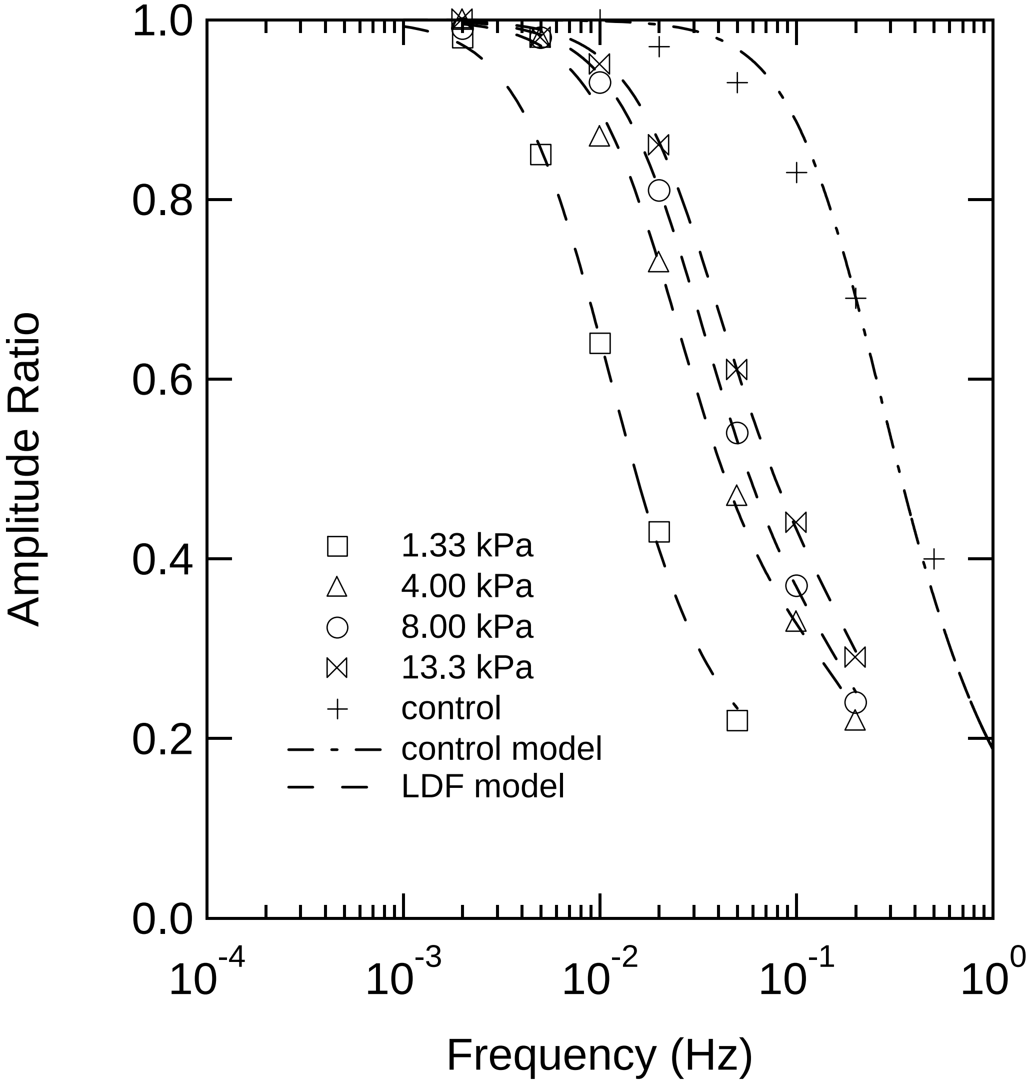

Figure 4.9: Frequency response plot of the adsorption of hexane in BPL activated carbon at various hexane pressures and the LDF model

by the Darken equation. According to Do *et al.*,[19] this relationship applies because hexane is much larger than water and is able to occupy several sites on the carbon surface and thus experience a more homogenous surface relative to the surface experienced by water. However, over the entire range of pressure explored, the variance in the diffusivity is small and therefore definitive conclusions about the applicability of the Darken expression to a hexane BPL activated carbon system are limited. It should also be mentioned that the diffusivity data reported here are consistent with the expected range of diffusivities of hexane on activated carbon as reported by Do and Do.[27]

Water Diffusion in Silica Gel

The adsorption dynamics of water adsorbed in silica gel are distinctive when compared to the examples discussed thus far. While the ND model provides a good description of the diffusion of water and hexane in BPL activated carbon, it fails to describe the adsorption of water by silica gel. Shown in figure 4.10 is the frequency response plot and corresponding LDF and ND models for the diffusion of water in silica gel at 0.13 kPa, and figure 4.11 shows the frequency response plot of the entire data set with comparison to the LDF model. The response shown in these plots is described well by the LDF model.

As in the BPL activated carbon-water system, the ND and LDF models were applied at every pressure measured, and the ND model failed to describe any of the data. Also, the impact of the external film resistance was evaluated via a combined LDF-external film resistance model. It was determined that the external film mass transfer resistance makes only a limited contribution to the model, and the extracted LDF coefficient with and without the film resistance was nearly identical. All of the plots of the ND model were similar to the results shown in figure 4.10, and the thermal effects in the system were determined to be negligible by using an energy balance to

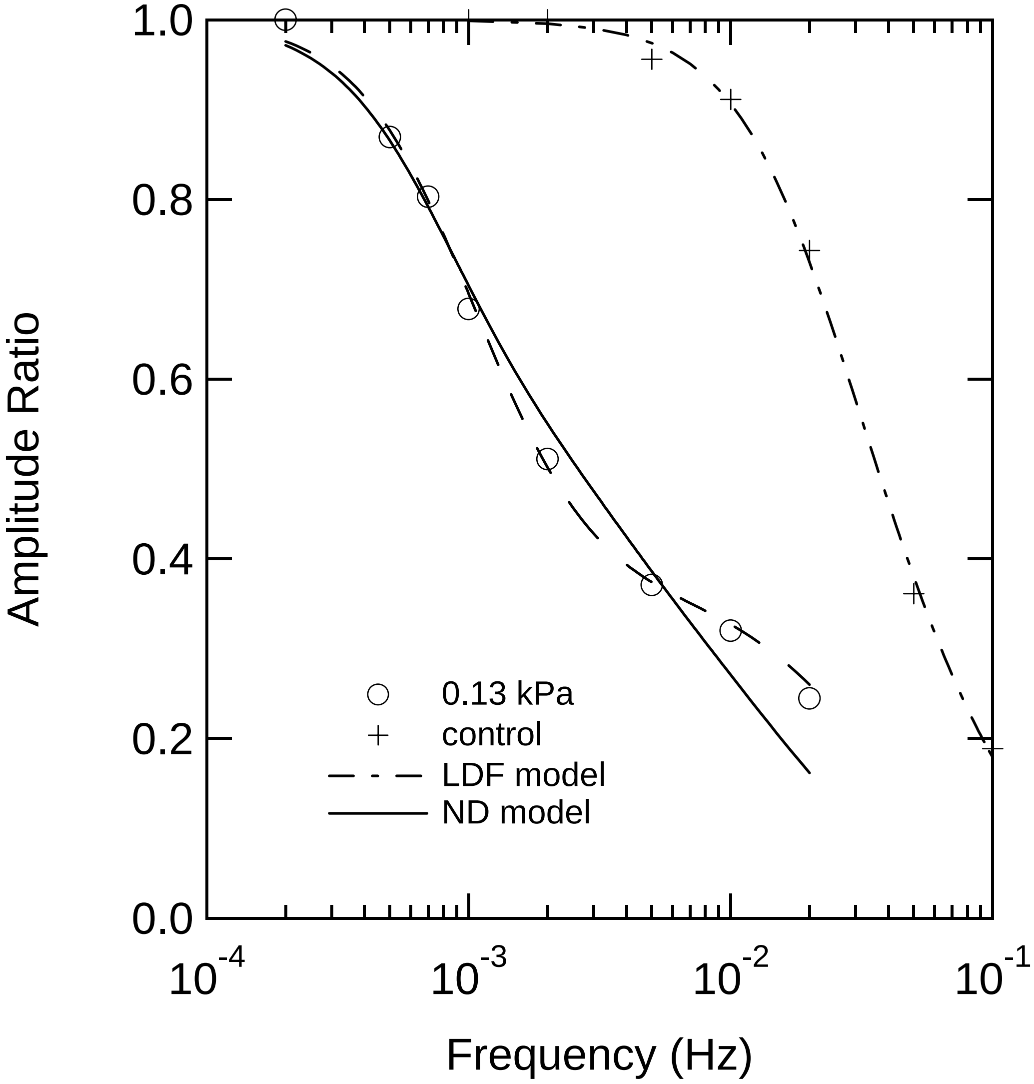

Figure 4.10: Frequency response plot of water diffusion in silica gel and the LDF and nanopore diffusion models.

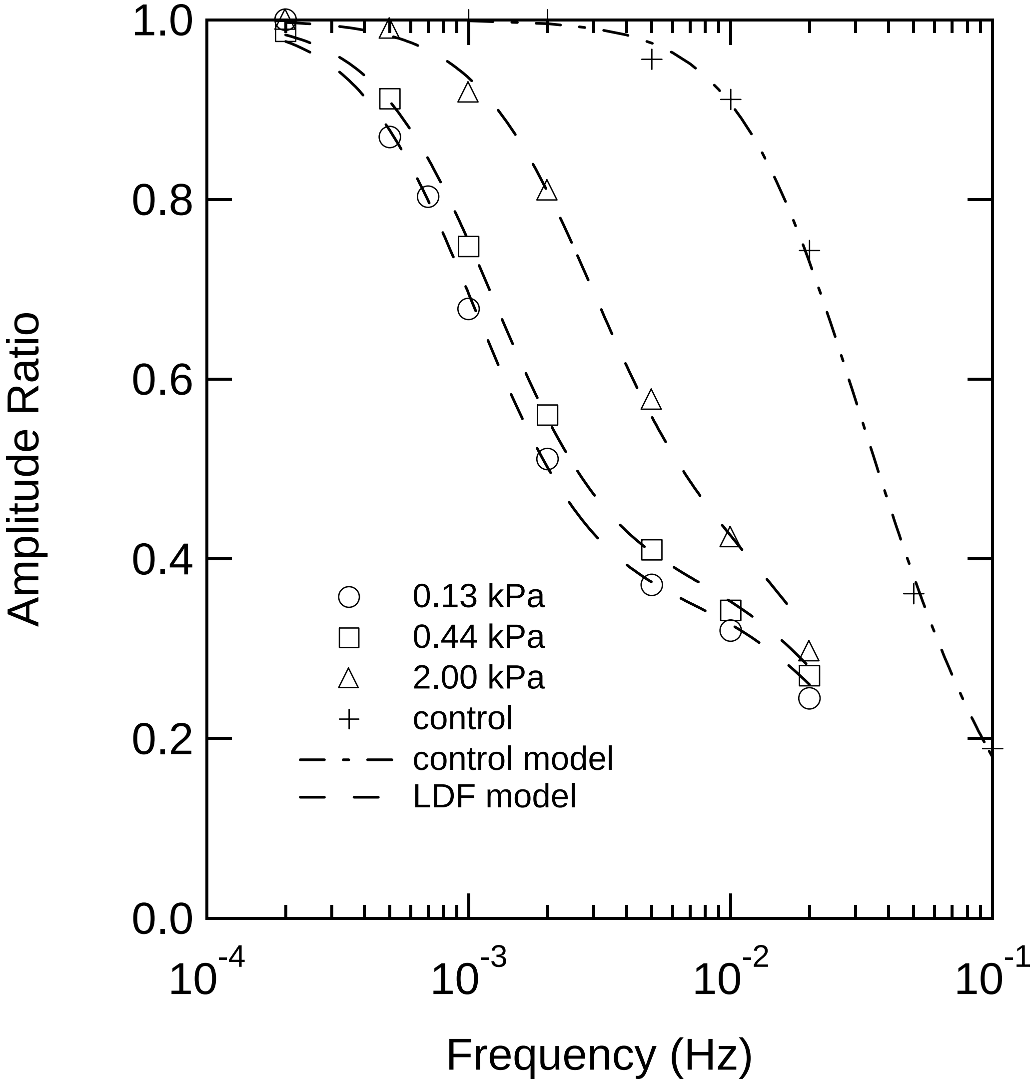

Figure 4.11: Frequency response plot of the adsorption of water in silica gel at various water pressures.

estimate the change in temperature at each pressure, which did not exceed 0.0032 K. To provide perspective on the error contained in the data, the experiment detailing the adsorption of water in silica gel at 2.0 kPa was repeated. A standard deviation of the amplitude data for the entire data set was determined to be 0.02 by averaging the standard deviations at each frequency. The amplitude data are on a scale from 0 to 1. The standard deviation with vapor generation is apparently somewhat greater than that for light gases.

As discussed for activated carbon, the LDF model provides a good description of the mass transfer of water in Davision Grade 40 silica gel. However, this model may not be appropriate for all silica gels given the wide variety in silica gel preparation methods, porosity, and chemical structure. One possible explanation for the failure of the ND model could be that the surface chemistry and morphology of silica gel are distinctly different when compared to activated carbon, and this gives two distinct mass transport mechanisms for the adsorption of water. Studies[45,48] have also shown the applicability of the LDF model to describe the diffusion of nitrogen, oxygen, and methane on carbon molecular sieves (CMS), which has a well defined pore constriction; therefore, it is reasonable that silica gel may also contain some nanopore constrictions.

The results discussed in these examples are distinctive as they provide documentation of the applicability of mass transport models to three systems. Furthermore, examining the diffusivities of water and hexane in BPL shows that hexane diffuses in BPL activated carbon at approximately two orders of magnitude faster than water. Likewise, by comparing the LDF coefficients of hexane and water it is clear that hexane diffuses approximately one order of magnitude faster in BPL than water does in silica gel.

4.4 Conclusion

This work documents the use of a concentration-swing frequency response apparatus to measure the diffusion of condensable vapors at room temperature. The mechanism of each system has been identified as either nanopore diffusion (surface diffusion) or a resistance characterized by a linear driving force. The adsorption kinetics of water and hexane in BPL activated carbon and water in silica gel were all characterized and the dependence of the diffusivity on loading identified. For BPL activated carbon, we found that water adsorption was well described by nanopore diffusion rather than by the LDF model adopted in previous studies, and the system shows unique behavior with the diffusivity reaching a minimum at approximately 0.5 P/P_o. The complexities of the adsorption of water in BPL inhibit the ability of the Darken relationship to adequately describe the change in diffusivity with concentration.

The diffusion of hexane in activated carbon is also well described by the nanopore diffusion model, the concentration dependence of the diffusivity is reasonably well predicted by the Darken equation, and the LDF model provides an excellent approximation of the Fickan diffusion mechanism. In contrast to the two previous examples, the diffusion of water in our silica gel is not well described by the micropore diffusion model, but rather, is best described using a linear driving force model. The structure and the surface chemistry of the silica gel is different from that of activated carbon, which may explain the need for two distinct rate mechanisms for the adsorption of water in BPL and silica gel.

Table 4.1: Diffusivities for adsorption of water in BPL activated carbon.

Measured Diffusivity D/R^2 (1/s)	Darken Diffusivity D/R^2 (1/s)	Pressure (kPa)	P/P_o
3.87×10^{-4}	9.65×10^{-4}	0.64	0.20
1.92×10^{-4}	5.68×10^{-4}	1.27	0.40
1.40×10^{-4}	3.29×10^{-4}	1.59	0.50
9.55×10^{-5}	1.38×10^{-4}	1.72	0.54
1.70×10^{-4}	1.70×10^{-4}	1.90	0.60
1.05×10^{-3}	2.00×10^{-4}	1.93	0.61
2.62×10^{-3}	2.79×10^{-4}	2.00	0.63
9.74×10^{-3}	5.30×10^{-4}	2.23	0.70
1.71×10^{-2}	6.45×10^{-4}	2.36	0.74

Table 4.2: Diffusivities for the adsorption of hexane in BPL activated carbon.

Measured Diffusivity D/R^2 (1/s)	Darken Diffusivity D/R^2 (1/s)	LDF Coefficient (1/s)	Pressure (kPa)
2.00×10^{-2}	2.27×10^{-2}	0.27	1.33
2.26×10^{-2}	2.78×10^{-2}	0.37	4.00
3.22×10^{-2}	3.17×10^{-2}	0.47	8.00
3.48×10^{-2}	3.48×10^{-2}	0.48	13.3

Table 4.3: Linear driving force coefficients for adsorption of water in silica gel.

LDF Coefficient (1/s)	Pressure (kPa)
1.49×10^{-2}	0.13
1.65×10^{-2}	0.44
3.57×10^{-2}	2.0

References

[1] Do, D.D. *Adsorption Analysis Equilibria and Kinetics*, Imperial College Press, London, 1998.

[2] Cussler, E.L. *Multicomponent Diffusion*, Elsevier, New York, 1976.

[3] Karger, J. and Ruthven D.M., *Diffusion in Zeolites*, Wiley, New York, 1992.

[4] Dubinin M.M., Water Vapor Adsorption and the Microporous Structures of Carbonaceous Adsorbents. *Carbon* 1980, 18, 355-364.

[5] Talu O., Meunier F., Adsorption of Associating Molecules in micropores and Application to Water on Carbon. *AIChE J.* 1996, 42, 809-819.

[6] Do D.D., Do H.D., A Model for Water Adsorption in Activated Carbon. *Carbon* 2000, 38, 797-773.

[7] Furmaniak S., Gauden P.A., Terzyk A.P., Rychlicki G., Wesolowski R.P., Kowalczyk P., Hetergeneous Do-Do model of Water Adsorption on Carbons. *J. Colloid Interface Sci.* 2005, 290, 1-13.

[8] Wongkoblap A., Do D.D., Adsorption of Water in Finite Length Carbon Slit Pore: Comparison between Computer Simulation and Experiment. *J. Phys. Chem. B* 2007, 111, 13949-13956.

[9] Salame I.I., Bandosz T.J., Experimental Study of Water Adsorption on Activated Carbons. *Langmuir* 1999, 15, 587-593.

[10] Salame I.I., Bandosz T.J., Study of Water Adsorption on Activated Carbons with Different Degrees of Surface Oxidation. *J. Colloid Interface Sci.* 1999, 210, 367-374.

[11] Fletcher A.J., Uygur Y., Thomas K.M., Role of Surface Functional Groups in the Adsorption Kinetics of Water Vapor on Microporous Carbons. *J. Phys. Chem. C* 2007, 111, 8349-8359.

[12] Striolo A., Chialvo A.A., Cummings P.T., Gubbins K.E., Water Adsorption in Carbon-Slit Nanopores. *Langmuir* 2003, 19, 8583-8591.

[13] Liu J.C., Monson P.A., Does Water Condense in Carbon Pores? *Langmuir* 2005, 21, 10219-10225.

[14] Foley N.J., Thomas K.M., Forshaw P.L., Stanton D., Norman P.R., Kinetics of Water Vapor Adsorption on Activated Carbon. *Langmuir* 1997, 13, 2083-2089.

[15] Harding A.W., Foley N.J., Norman P.R., Francis D.C., Thomas K.M., Diffusion Barriers in the Kinetics of Water Vapor Adsorption/Desorption on Activated Carbons. *Langmuir* 1998, 14, 3858-3864.

[16] Cossarutto L., Zimny T., Kaczmarczyk J., Siemieniewska T., Bimer J., Weber J.V., Transport and sorption of Water Vapour in Activated Carbons. *Carbon* 2001, 39, 2339-2346.

[17] Qi N., Appel S., LeVan M.D., Finn J.E., Adsorption Dynamics of Organic Compounds and Water Vapor in Activated Carbon Beds. *Ind. Eng. Chem. Res.* 2006, 45, 2303-2314.

[18] Do D.D., Do H.D., Prasetyo I., Constant Molar Flow Semi-Batch Adsorber as a tool to study Adsorption Kinetics of Pure Gases and Vapours. *Chem. Eng. Sci.* 2000, 55, 1717-1727.

[19] Do H.D., Do D.D., Prasetyo I., Surface Diffusion and Adsorption of Hydrocarbons in Activated Carbon. *AIChE J.* 2001, 47, 2515-2525.

[20] Do D.D., Dynamics of a Semi-Batch Adsorber with Constant Molar Supply Rate: A Method for studying Adsorption Rate of Pure Gases. *Chem. Eng. Sci.* 1995, 50, 549-553.

[21] Wang K., King B., Do D.D., Rate and Equilibrium Studies of Benzene and Toluene Removal by Activated Carbon. *Sep. Purif. Tech.* 1999, 17, 53-63.

[22] Bae J.S., Do D.D., Surface Diffusion of Strongly Adsorbing Vapors in Activated Carbon by a Differential Permeation Method. *Chem. Eng. Sci.* 2003, 58, 4403-4415.

[23] Bae J.S., Do D.D., Study on Diffusion and Flow of Benzene, n-Hexane, and CCl_4 in Activated Carbon by a Differential Permeation Method. *Chem. Eng. Sci.* 2002, 57, 3013-3024.

[24] Bae J.S., Do D.D., Permeability of Subcritical Hydrocarbons in Activated Carbon. *AIChE J.* 2005, 51, 487-501.

[25] Rutherford S.W., Do D.D., Permeation Time Lag with Multilayer Adsorption and Surface Diffusion. *Chem. Eng. Sci.* 1999, 74, 155-160.

[26] Prasetyo I., Do H.D., Do D.D., Surface Diffusion of Strongly Adsorbing Vapors on Porous Carbon. *Chem. Eng. Sci.* 2002, 57, 133-141.

[27] Do D.D., Do H.D., Surface Diffusion of Hydrocarbons in Activated Carbon: Comparison Between Constant Molar Flow, Differential Permeation, and Differential Adsorption Bed Methods. *Adsorption* 2001, 7, 189-209.

[28] Fletcher A.J., Thomas K.M., Adsorption and Desorption Kinetics of n-Octane and n-Nonane Vapors on Activated Carbon. *Langmuir* 1999, 15, 6908-6914.

[29] Fletcher A.J. Thomas K.M., Compensation Effect for the Kinetics of Adsorption / Desorption of Gases / Vapors on Microporous Carbon Materials. *Langmuir* 2000, 16, 6253-6266.

[30] Fletcher A.J., Yuzak Y., Thomas K.M., Adsorption and Desorption Kinetics for Hydrophilic and Hydrophobic Vapors on Activated Carbon. *Carbon* 2006, 44, 989-1004.

[31] Golden T.C., Kumar R., Adsorption Equilibrium and Kinetics for Multiple Trace Impurities in Various Gas Streams on Activated Carbon. *Ind. Eng. Chem. Res.* 1993, 32, 159-165.

[32] Saxena A., Singh B., Sharma A., Dubey V., Semwal R.P., Suryanarayana M.V.S., Rao V.K., and Sekhar K., Adsorption of Dimethyl Methylphophonate on Metal Impregnated Carbons Under Static Conditions. *J. Haz. Mater. B* 2006, 134, 104-111.

[33] Kapoor A., Yang R.T., Contribution of Concentration-Dependent Surface Diffusion to Rate of Adsorption. *Chem. Eng. Sci.* 1991, 46, 1995-2002.

[34] Chihara K., Suzuki M., Air Drying by Pressure Swing Adsorption. *J. Chem. Eng. Japan* 16, 293-299.

[35] Aristov Y.I., Tokarev M.M., Freni A., Glaznev I.S., Restuccia G., Kinetics of Water Adsorption on Silica Fuji Davison RD. *Micro. Meso. Mater.* 2006, 96, 65-71.

[36] Ni C.C., San J.Y., Measurement of Apparent Solid-Side Mass Diffusivity of a Water Vapor-Silica Gel System. *Int. J. Heat Mass Trans.* 2002, 45, 1839-1847.

[37] Rajniak P., Yang R.T., Unified Network Model for Diffusion of Condensable Vapors in Porous Media. *AIChE J.* 1996, 42, 319-331.

[38] Yamamoto E., Watanabe F., Kobayashi N., Hasatani M., Intraparticle Heat and Mass Transfer Characteristics of Water Vapor Adsorption. *J. Chem. Eng. Japan* 2002, 35, 1-8.

[39] Li X., Zhong L., Xia Q., Hongxia X., Effects of Pore Sizes of Porous Silica Gels on Desorption Activation Energy of Water Vapour. *App. Therm. Eng.* 2007, 27, 869-876.

[40] Shen D., Rees L.V.C., Frequency Response Technique Measurements of *p*-Xylene Diffusion in Silicalite-1 and -2. *J. Chem. Soc. Fara. Trans.* 1993, 89, 1063-1065.

[41] Shen D., Rees L.V.C., Analysis of Bimodal Frequency-Response Behavior of *p*-Xylene Diffusion in Silicalite-1. *J. Chem. Soc. Faraday Trans.* 1995, 91, 2027-2033.

[42] Shen D., Rees L.V.C., Study of Fast Diffusion in Zeolites using a Higher Harmonic Frequency Response Method. *J. Chem. Soc. Faraday Trans.* 1994, 90, 3011-3015.

[43] Song L., Rees L.V.C., Adsorption and transport of *n*-hexane in Silicalite by the Frequency Response Technique. *J. Chem. Soc. Faraday Trans.* 1997, 93, 649-657.

[44] Song L., Rees L.V.C., Adsorption and Diffusion of Cyclic Hydrocarbons in MFI-type Zeolites Studied by Gravimetric and Frequency-Response Techniques. *Micro. and Meso. Maters.* 2000, 35-36, 301-314.

[45] Wang Y., LeVan M.D., Mixture Diffusion in Nanaoporous Adsorbents: Development of Fickian Flux Relationship and Concentration-Swing Frequency Response Method. *Ind. Eng. Chem. Res.* 2007, 46, 2141-2154.

[46] Wang Y., LeVan M.D., Investigation of Mixture Diffusion in Nanoporous Adsorbents via the Pressure-Swing Frequency Response Method. 1. Theoretical Treatment. *Ind. Eng. Chem. Res.* 2005, 44, 3692-3701.

[47] Wang Y., LeVan M.D., Investigation of Mixture Diffusion in Nanoporous Adsorbents via the Pressure-Swing Frequency Response Method. 2. Oxygen and Nitrogen in a Carbon Molecular Sieve. *Ind. Eng. Chem. Res.* 2005, 44, 4745-4752.

[48] Wang Y., Sward B.K., LeVan M.D., New Frequency Response Method for Measuring Adsorption Rates via Pressure Modulation: Application to Oxygen and Nitrogen in a Carbon Molecular Sieve. *Ind. Eng. Chem. Res.* 2003, 42, 4213-4222.

[49] Wang Y., LeVan M.D., New Developments in Flow-Through Apparatus for Measurement of adsorption mass-transfer rates by frequency response method. *Adsorption* 2005, 11, 409-414.

[50] Sward B.K., LeVan M.D., Frequency Response Method for Measuring Mass Transfer Rates in Adsorbents via Pressure Perturbation. *Adsorption* 2003, 9, 37-54.

[51] Petkovaska M., Do D.D., Nonlinear Frequency Response of Adsorption Systems: Isothermal Batch and Continuous Flow Adsorbers. *Chem. Eng. Sci.* 1998, 53, 3081-3097.

[52] Petkovska M., Do D.D., Use of Higher-Order Frequency Response Functions for Identification of nonlinear Adsorption Kinetics: Single Mechanisms under Isothermal Conditions. *Nonlinear Dynamics* 2000, 21, 353-376.

[53] Petkovska M., Nonlinear Frequency Response of nonisothermal Adsorption Systems. *Nonlinear Dynamics* 2001, 26, 351-370.

[54] Petkovska M., Petkovska L., Use of Nonlinear Frequency Response for Discriminating Adsorption Kinetics Mechanisms Resulting with Bimodal Characteristic Functions. *Adsorption* 2003, 9, 133-142.

[55] Petkovska M., Application of Nonlinear Frequency Response to Adsorption Systems with Complex Kinetic Mechanisms. *Adsorption* 2005, 11, 497-502.

[56] Petkovska M., Petkovska L.T., Application of Nonlinear fFequency Response to Investigation of Membrane Transport. *Sep. Sci. Tech.* 2006, 41, 43-72.

[57] Onyestyak G., Valyon J., Bota A., Rees L.V.C., Frequency-Response Evidence for Parallel Diffusion Processes in the Bimodal Micropore System of an Activated Carbon. *Helvetica Chimica Acta* 2002, 85, 2463-2468.

[58] Wang Y., LeVan M.D., Nanopore Diffusion Rates for Adsorption Determined by Pressure-Swing and Concentration-Swing Frequency Response and Comparison with Darken's Equation. *Ind. Eng. Chem. Res.*, in press.

Nomenclature

$D =$ main-term diffusivity, m^2/s

$K =$ local slope of isotherm dn/dp, mol/(g kPa)

$n =$ adsorbate concentration, mol/kg

$P =$ pressure, kPa

$r =$ radial coordinate of microparticle, m

$R =$ microparticle radius, m

$T =$ temperature, K

$t =$ time, s

Subscripts

$o =$ saturation

CHAPTER V

SENSITIVITY ANALYSIS OF ADSORPTION BED BEHAVIOR: EXAMINATION OF PULSE INPUTS AND LAYERED-BED OPTIMIZATION

5.1 Introduction

Understanding how a process variable affects the output of a pulse is critical for the design and optimization of efficient fixed-bed systems. Specific applications of this type include building filters for large scale air purification, gas masks for protection against toxic gases and vapors, fixed-bed adsorbers for solvent recovery, and temperature and pressure swing adsorption systems.

Detailed quantitative sensitivity data allows for the dynamics of a variety of adsorption processes to be better understood. For example, fixed-bed adsorption systems are frequently used to remove pulse inputs of toxic gases or vapors. In this case, sensitivity data can provide quantitative proof of what phenomena are governing the system, which allows for the design of a system optimized for the factors that most directly impact performance. Without sensitivity data, it is difficult to designate one process parameter as more important than another. In particular, it is impossible to know if the isotherm parameters, mass transport parameters, or energy parameters are controlling the system.

The dynamics of pulses in fixed beds is one of many industrial situations that can be characterized using sensitivity data. For example, it is common for an industrial process to remove gases from humid process streams via adsorption. In this case, sensitivity data can provide quantitative evidence for how much water can be tolerated in the process stream without degradation of adsorber performance beyond acceptable limits.

In addition to illustrating which process or transport parameters are controlling an adsorption process, quantitative sensitivity data provide a means to optimize the system with respect to a variety of process variables. The data that are returned in a sensitivity analysis are more than a simple measure of which parameter is more important than others. The sensitivity data are a quantitative representation of how a particular parameter is impacting the output of the system at a particular time. The application of such detailed data allows for the optimization of a process with respect to any process variable.

Sensitivity of adsorption cycles to input parameters has been explored both experimentally and computationally.[7, 11, 17, 20, 26–28, 31, 34, 35] One approach to determine the effect of a process variable is to hold all other process variables constant and vary the parameter of interest. By performing several runs and varying several different process variables it is possible to determine the parameters that govern the system.[17, 20, 26] For example, Hartzog and Sircar[17] performed a simulation of the separation of ethylene and methane via a Skarstrom pressure swing adsorption (PSA) cycle and determined that small errors in the heats of adsorption of the components can severely alter the overall performance of the process. They also found that the mass transfer coefficients of the components must be accurate in order to obtain a precise description of the separation. In another study, Kumar[20] investigated the sensitivity of a four-bed, nine-step, PSA process used to separate methane from hydrogen. The performance of the system was examined relative to the mass transport resistances, purge gas quantity, and isotherm shape. The results showed that increasing the mass transfer coefficient used in the linear driving force model increased performance, but only up to a limit. By increasing the porosity of the adsorbent to increase mass transfer, the overall bulk density of the adsorbent was reduced, which decreased the total volumetric production of the unit. The work also revealed that it is important to consider not only the maximum working capacity of the adsorbent, but also its selectivity. In addition to these studies, Sircar[32] studied the influence of the fluid-solid heat film resistance on the performance of a PSA system. In this study, the author concluded that the fluid-solid heat film transfer coefficient may impact the efficiency of the system in cases where the Nusselt number is less than six.

Other studies have also examined the sensitivity of PSA units to purify hydrogen. For example, Malek and Farooq[26] studied the recovery of hydrogen from a stream containing methane, ethane, propane, and butane. The process had six layered beds, and hydrogen comprised 60-70% of the feed. The authors demonstrated the effect of high operating pressure on product recovery and purity and the effects of treating the adsorption system isothermally. In addition to the studies mentioned, several other authors have also examined the effects of other process variables such as production pressure, purge gas flow rate, production duration, feed gas conditions, purge gas pressure, and pressurization rates on both product purity and recovery of adsorption systems.[11,27,28,34]

Sensitivity analysis has not been limited to PSA systems. For example, Sircar *et al.*[31] considered the effects of heat losses to the surroundings on the breakthrough curve of a single adsorbate from an inert carrier gas. They determined that heat losses may distort the symmetry of the breakthrough curve and showed that the analysis of a system by an isothermal or adiabatic model may yield incorrect mass transfer coefficients.

In another study concerning fixed beds, Walton and LeVan[35] examined the sensitivity of fixed-bed simulations to common energy balance approximations by using local equilibrium theory. They examined the sensitivity of the system to adsorbed-phase heat capacity and isosteric heat of adsorption. The results showed that the impact of common energy balance approximations was small for plateau temperature, partial pressure, and loadings, but large for breakthrough behavior.

The effects of mass transfer kinetics on adsorption processes behavior have also been examined. Chanbani-Tondeur[7] showed through modeling that neglecting intraparticle concentrations may lead to erroneous simulations. They present results that show the classic linear driving force and solid diffusion models are inadequate and recommend a pore diffusion model.

Quantifiable sensitivity information also allows for the direct optimization of an adsorption system.[9, 10, 13, 14] In direct optimization, the material and energy balances are solved while simultaneously determining the sensitivity of the solution to initial conditions. The sensitivity information is then used to determine the periodic steady state directly. Direct optimization is frequently used to determine the optimal operating conditions of PSA systems, and a variety of process conditions have been examined.[1, 18, 19]

Performing multiple simulation runs or simultaneously calculating sensitivities is not the only method of acquiring sensitivity data. Chlendi *et al.*,[8] for example, developed a set of polynomials that describe the sensitivity of PSA cycle performance in relation to design variables. The set of polynomials provides a quantitative means to optimize the performance of the adsorption system.

This paper examines two adsorption applications for which sensitivities are particularly important but have not been utilized in any detail, namely, a pulse input to an adsorption bed and an optimally layered bed. The study of the sensitivity of a pulse input to a fixed bed is absent in the research literature and is particularly relevant to industrial situations. Fixed beds found in fume hoods or building filtration units frequently retain pulses of organic vapors. However, the pulse input, once adsorbed, continues to propagate through the bed as air passes through the filter. If the filters are not changed the pulse will break through the bed and begin to contaminate the effluent air. Examining the ability of fixed beds to retain a pulse input relative to various process parameters is important for the proper design of filtration systems receiving non-constant feed concentrations, such as building filters or gas masks. Furthermore, sensitivity data can illustrate effects that are counterintuitive, such as unique energy and mass transport effects and can quantitatively prove that a particular process parameter may have little or no impact on the output. Also missing from the current literature is the use of sensitivity data to optimize the adsorbent layers in a fixed bed. While the optimization of PSA systems in relation to a variety of process conditions has been documented, using sensitivity data to determine directly the optimum bed layering has not been studied. The method used to optimize a layered bed can also be applied to optimize a system with respect to particle radius, end cap and wall effects, feed temperature, and bed layering. These types of optimizations can be explored in process models for both fixed beds and PSA systems.

Several different examples are considered. In the first example, a low-concentration pulse of hexane is passed to a fixed bed of BPL activated carbon after which nitrogen, assumed inert, passes continually through the bed. The hexane is readily adsorbed by the fixed bed but will continue to slowly migrate through the bed until it eventually breaks through. The purpose of this case is to illustrate the use of modeling for the estimation of the residual life of a fixed-bed filter and to determine what impact transport resistances have on the retention time of a low-concentration organic vapor in a fixed bed of BPL activated carbon.

The second example considered is the adsorption of nitrogen on a carbon molecular sieve adsorbent. This example is different from the first in that the time required for breakthrough is shorter, the adsorbate is a light gas, and the adsorbent has a known mass transport limitation.

In the third example, the adsorption of a pulse of nitrogen on activated carbon is studied. This example considers the sensitivity of a weakly adsorbed pulse to both mass and energy transport coefficients. This example is important because it reveals unique mass and energy transport effects that are counterintuitive.

The last example considers the sensitivity of the performance of a PSA system for the separation of methane from a feed stream containing carbon dioxide and nitrogen. The adsorbent bed contains a layer of 13 X zeolite used to remove carbon dioxide, followed by a layer of carbon molecular sieve used to separate the nitrogen and methane. By calculating sensitivity data the product purity from the PSA system can be optimized with respect to bed layering.

5.2 Mathematical Model

For the examples involving only a mass conservation equation the following assumptions are made: (1) the ideal gas law applies, (2) only one adsorbable component is present in the fluid-phase, (3) the system is isothermal, and (4) the velocity and pressure are constant. The mass transport parameters considered in this model include the external-film resistance, the Glueckauf linear driving force solid-phase resistance, and axial dispersion. The material balance, rate equations, and boundary conditions used in these examples are

$$k_f a(c - c^*) + \epsilon' \frac{\partial c}{\partial \tau} + \frac{\partial c}{\partial \zeta} = \frac{1}{Pe} \frac{\partial}{\partial \zeta} \left(\frac{\partial c}{\partial \zeta} \right) \tag{5.1}$$

$$\rho_b \frac{\partial n}{\partial \tau} = k_f a(c - c^*) = k_n(n^* - n) \tag{5.2}$$

$$c - \frac{1}{Pe} \frac{\partial c}{\partial \zeta} = c_{feed} \quad \text{at} \quad \zeta = 0 \tag{5.3}$$

$$\frac{\partial c}{\partial \zeta} = 0 \quad \text{at} \quad \zeta = 1 \tag{5.4}$$

where n is the adsorbed-phase concentration, c is the fluid-phase concentration, τ is dimensionless time, and ζ is dimensionless distance. Dimensionless groups are defined as

$$\tau = \frac{\epsilon v_{ref} t}{L} \tag{5.5}$$

$$\zeta = \frac{z}{L} \tag{5.6}$$

The model of Mahle *et al.*[25] is used for examples that involve mass and energy effects and PSA systems. The original model has been modified following the work of Davis and LeVan[12] to include a fluid-solid heat transfer coefficient. The conservations equations and rate equations are

$$k_n a(n^* - n) + \epsilon' \frac{\partial c}{\partial t} + \frac{\partial (vc)}{\partial t} = 0 \tag{5.7}$$

$$\rho_b \frac{\partial n}{\partial t} = k_n (n^* - n) \tag{5.8}$$

$$ha(T_f - T_s) + \epsilon' \frac{\partial c u_f}{\partial t} + \frac{\partial v c h_f}{\partial z} = -U_p (T_f - T_w) \tag{5.9}$$

$$\rho_b \frac{\partial u_s}{\partial t} = ha(T_f - T_s) \tag{5.10}$$

$$\epsilon' \frac{\partial c u_f}{\partial t} + \frac{\partial v c h_f}{\partial z} = -U_e (T_f - T_w) \tag{5.11}$$

$$-U_p(T_w - T_f) - U_o(T_w - T_{surr}) = m_w c_{pw} \frac{\partial T_w}{\partial t} \tag{5.12}$$

with

$$u_f = h_f - P/\rho_f \tag{5.13}$$

$$h_f = c_{pf}(T - T_{ref}) \tag{5.14}$$

$$u_s = c_{ps}(T - T_{ref}) + n h_a - \int_0^n \lambda dn \tag{5.15}$$

where v is the velocity, u_f is the internal energy of the fluid, h_f is the enthalpy of the fluid, u_s is the internal energy of the solid, and other parameters are defined in the original work. When this model is applied to the PSA example the temperature of the fluid and solid are assumed to be equal. The equation used to represent the isotherm data presented in the original work is

$$P = n \exp[k_o + (k_1/T) + (k_2 n/T)] \tag{5.16}$$

where P is in kPa, T is in Kelvin, and parameters are $k_o = 22.75$, $k_1 = -5101$, and $k_2 = 922$. In the energy balance presented in eqs. 5.9-5.12, U_p, U_e, and U_o are the energy transport coefficients for the packed column, the empty column, and the exterior of the column, respectively. Equation 5.11 describes the energy transport taking place in the end caps of the column, which do not contain adsorbent, while eq. 5.12 describes the transport of energy between the column wall and the surroundings. The non-isothermal model makes the following assumptions: (1) the ideal gas law applies, (2) there are negligible axial pressure gradients, (3) the temperature gradient in the wall is negligibly small, and (4) the temperature dependence of the fluid-phase properties is neglected relative to the large dependence of the fluid-phase properties on pressure.

The examples involving only a parabolic equation for mass conservation are evaluated with central differences, while equations pertaining to the hyperbolic model of Mahle *et al.* are evaluated using backward differences. The process model can be integrated using an initial value problem integrator such as ODESSA[21] or DASPK 3.0,[23,24] which allow for the local sensitivities of the system to multiple process variables to be determined in one integration. In this work, the sensitivity data are simultaneously calculated as the process model is integrated using ODESSA. The sensitivities can be incorporated in a Taylor series as

$$c_{new} = c + \frac{\partial c}{\partial \ln p_1}\Delta \ln p_1 + \frac{\partial c}{\partial \ln p_2}\Delta \ln p_2 + \cdots + \frac{\partial c}{\partial \ln p_n}\Delta \ln p_n + \cdots \tag{5.17}$$

where the parameters have been expressed using differences in $\ln p$ so that the data can be plotted as the change in the breakthrough curve for a fractional change in a parameter.

5.3 Examples

Hexane Adsorption on BPL Activated Carbon

In this first example, we are interested in determining the parameters that govern low-concentration pulses adsorbed on activated-carbon beds over long periods of time. The bed is pulsed with hexane in nitrogen for approximately 1800 seconds, after which nitrogen, which is assumed non-adsorbing, is passed through the bed. Because hexane is strongly adsorbed on BPL activated carbon, the pulse remains in the bed for a long period of time.

The system is based on the work of Davis and LeVan.[12] Equations 5.1-5.3 include a term for axial dispersion but not an energy balance. The process parameters examined via sensitivity analysis were the solid-phase linear driving force coefficient k_n, the external fluid-phase transport coefficient k_f, and the Peclet number Pe. The transport coefficients were estimated using the methods presented in the original work. The linear driving force coefficient was used as reported by Shin *et al.*,[30] and Pe was estimated via methods outlined in the work of LeVan.[22] Adsorption equilibria were used as given by Qi and LeVan.[29] System parameters for this example are presented in Table 5.1.

Figure 5.1 shows the breakthrough of the fluid-phase for three pulses. Included in this figure is the pulse as predicated by local equilibrium theory, which is a pure shock at the toe of the breakthrough curve with a gradual tail as determined by the slope of the isotherm. The calculation of the local equilibrium pulse was performed originally by Glueckauf.[16] Using the method outlined by LeVan,[22] Glueckauf's result was recast into notation convenient for this example. For the gradual tail, because the derivatives are constant with a uniformly saturated bed, the material balance gives

$$\rho_b \zeta = \frac{\tau}{dn/dc} \tag{5.18}$$

The material balance to determine the total amount adsorbed in the column with a pulse input is

$$\int_{\zeta_{\text{back}}}^{\zeta_{\text{front}}} \rho_b n \; d\zeta = c_{feed} \tau_o \tag{5.19}$$

where the integration is performed from the back of the wave to the front of the wave

Table 5.1: System Parameters for Examples 1 and 2

	Hexane/ Activated Carbon	Nitrogen/ CMS
T	298 K	298 K
k_n	0.002 s^{-1}	5.4×10^{-4} s^{-1}
k_f	0.064 m/s	0.216 m/s
n_o	2.13 mol/kg	0.372 mol/kg
c_{feed}	7.50 mmol/m^3	3.76 mmol/m^3
t_p	1890 s	10 s
L	0.1 m	0.29 m
R_p	1.0×10^{-3} m	1.25 $\times 10^{-3}$ m
ϵ	0.4	0.2
ϵ'	0.7	0.52
ρ_b	480 kg/m^3	550 kg/m^3

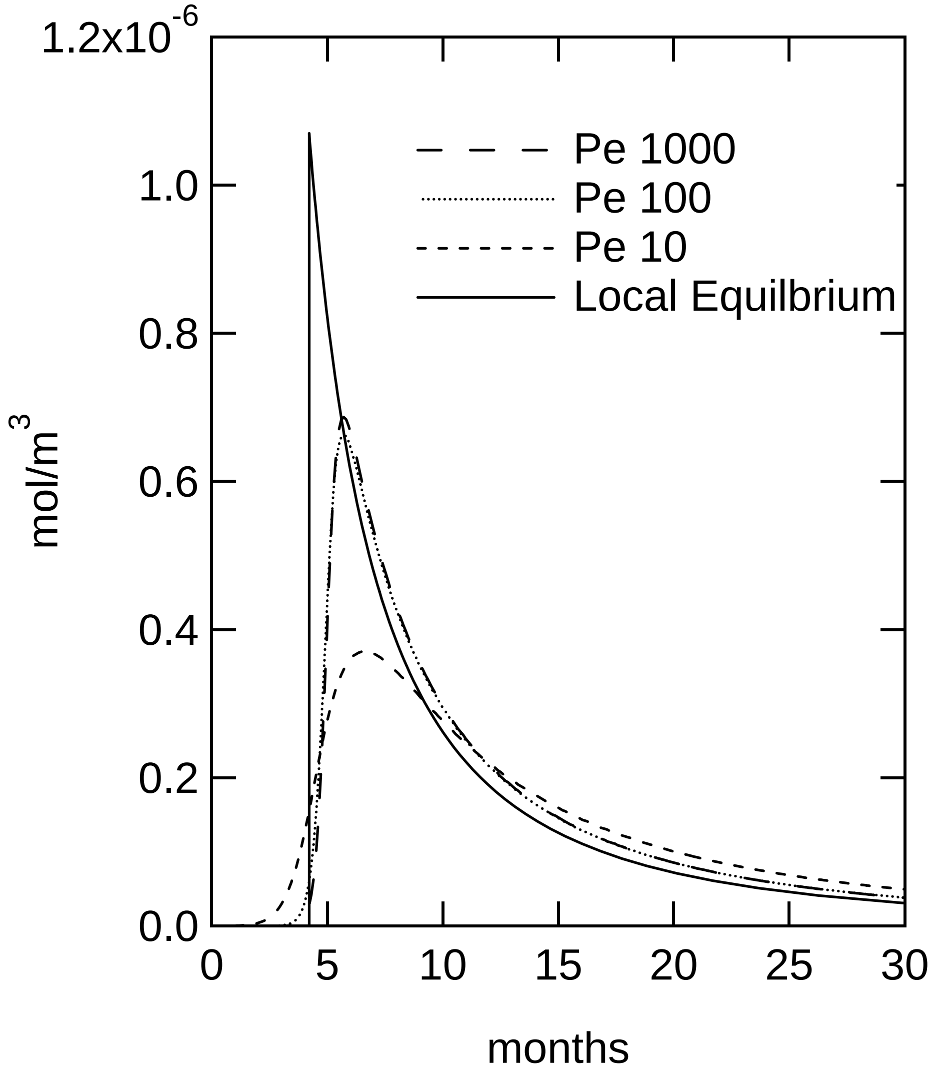

Figure 5.1: Breakthrough curves at three different Peclet numbers and as predicted by local equilibrium theory.

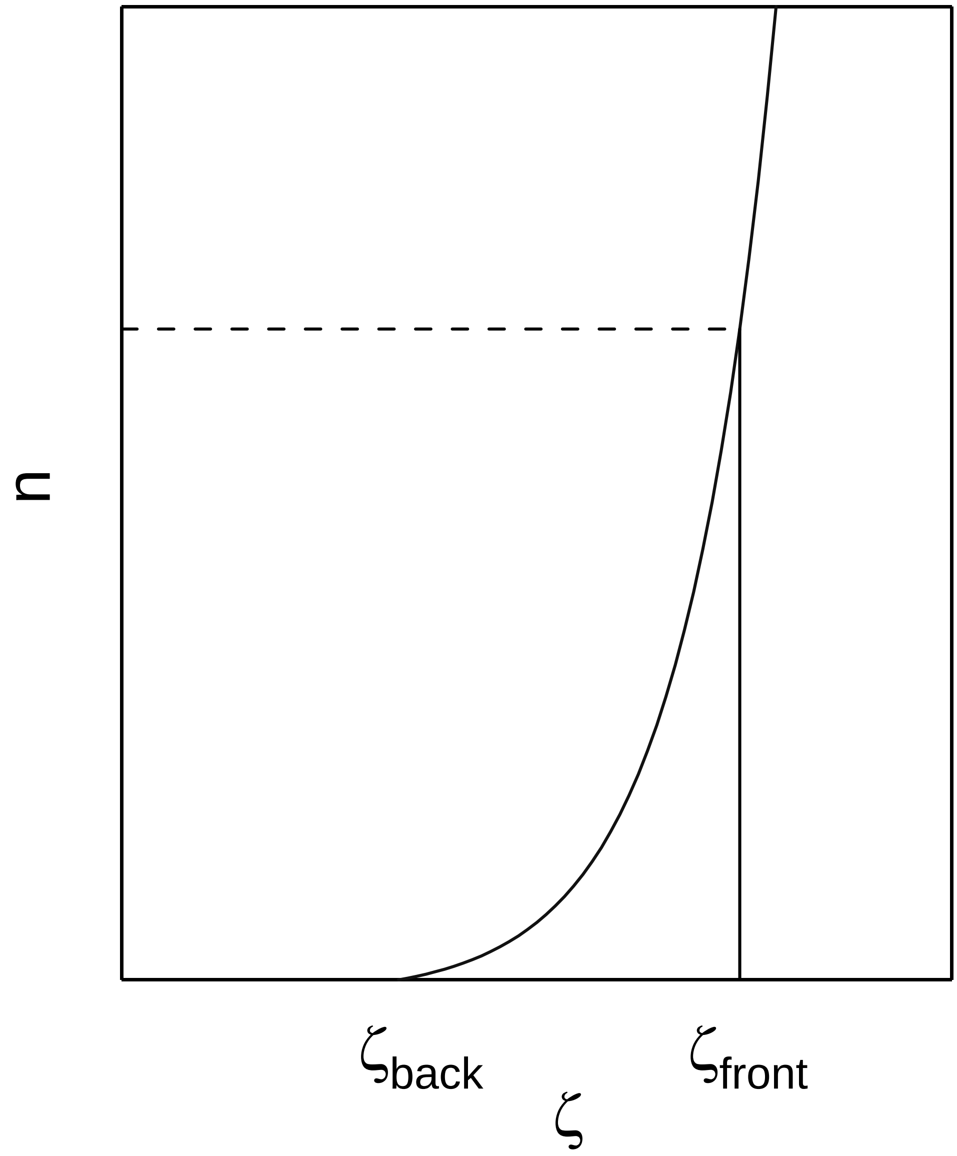

Figure 5.2: Wave front in the adsorbed-phase down the length of the column.

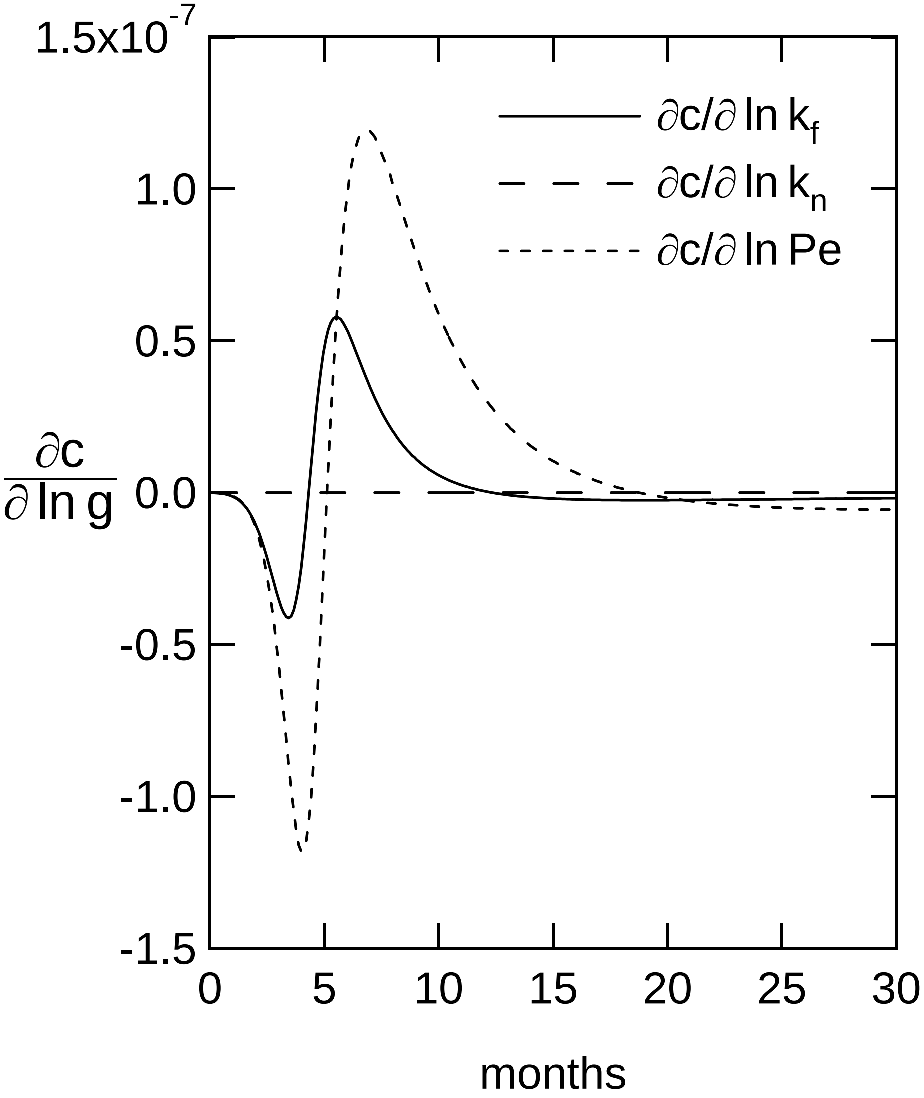

Figure 5.3: Sensitivity of the breakthrough curve with respect to k_n, k_f, and Pe at $Pe = 10$ where g represents any of the parameters of interest.

as illustrated in Figure 5.2. Integrating eq. 5.19 by parts gives

$$\left(\frac{n_{front}}{dn/dc|_{front}} - c_{front}\right)\tau = c_{feed}\tau_o \tag{5.20}$$

To determine the local equilibrium pulse, a fluid-phase concentration range was first selected. Second, eq. 5.18 was used to determine the τ that corresponds to the concentration range. The curve generated by eq. 5.18 is a locus of pulse maxima that can occur at the bed outlet and reflects the slope of the adsorption isotherm at a particular fluid-phase concentration. Finally, eq. 5.18 was solved for τ and substituted into eq. 5.20 to give

$$\zeta = \frac{c_{feed}\tau_o}{\rho_b(n - c\, dn/dc)} \tag{5.21}$$

Setting ζ to 1 in eq. 5.21 and solving for the outlet concentration provided the concentration that corresponds to the apex of the local equilibrium pulse.

The sensitivity of the breakthrough of the pulse to changes in k_n, k_f, and Pe is presented in Figure 5.3, which shows the pulse as it passes through the bed. The sensitivity data show that for a fractional change in the three parameters of interest, Pe will have the largest effect on the breakthrough curve. By examining the sensitivity of the breakthrough concentration with respect to Pe in Figure 5.3, it can be seen that between approximately 0 and 5 months, an increase in Pe will decrease the fluid-phase concentration at the outlet. The data presented in Figure 5.1 also follows this trend. As Pe is increased, the pulse is sharpened and the base of the pulse narrows, thus decreasing the fluid-phase concentration.

At approximately 5 months, the sensitivity data in Figure 5.3 pass through zero showing that the pulse is insensitive to modest changes in Pe at this time. As predicted by the sensitivity data, the breakthrough curves do indeed appear insensitive to changes in Pe at approximately 5 months. In fact, increasing Pe from 10 to 100 had little effect on the shape of the breakthrough curve. With an increase in Pe, the breakthrough curves show an increase in fluid-phase concentration at approximately 5 to 12 months and a decrease in fluid-phase concentration from 12 to 30 months. The changes seen in the breakthrough curves are reflected in the sensitivity data and are consistent with a pulse approaching local equilibrium.

Between 5 and 18 months the sensitivity curve shows an increase in fluid-phase concentration with increasing Pe. The time indicated by the sensitivity data for the transition of Pe from a positively correlated relationship with fluid-phase concentration to a negatively correlated relationship is about 18 months; however, the breakthrough curves show this transition at about 12 months. The sensitivity data are local data based on the Taylor series expansion mentioned above. Therefore, dramatic increases in sensitivity parameters may affect the breakthrough curves differently than predicted by the sensitivity data plots. The increase in Pe from 100 to 1000 extends beyond the scope of the local derivatives reflected in the sensitivity data plots.

To ensure that the transition time indicated in the sensitivity plots is correct, small changes in Pe near 10 were made and the breakthrough curves studied. Figure 5.4 shows that for small changes in the Pe the transition occurs closer to 18 months and that increasing Pe moves the transition to shorter times. As changes to Pe move beyond the scope of the sensitivity data, the sensitivity plots begin to predict the effects on the breakthrough curves more qualitatively.

From the sensitivity data presented in Figure 5.3 it is clear that altering Pe will have the most dramatic effect on the breakthrough curve, followed by changes in k_f, while changes in k_n have no observed effect on output. Sensitivity data were also calculated for Pe of 100 and 1000. For the case were Pe is 100, the data in Figure 5.5 show that an increase in Pe will not impact the breakthrough curve as strongly as an equivalent change in the external-film resistance k_f. The narrowing of the base of the peak is seen in the sensitivity data for times between 0 and 4.5 months and again for times greater than 6.5 months. The increase in the apex of the peak with an increase in k_f is reflected in the sensitivity data between about 4.5 months and 6.5 months. The sensitivity data again show that the solid-phase resistance has

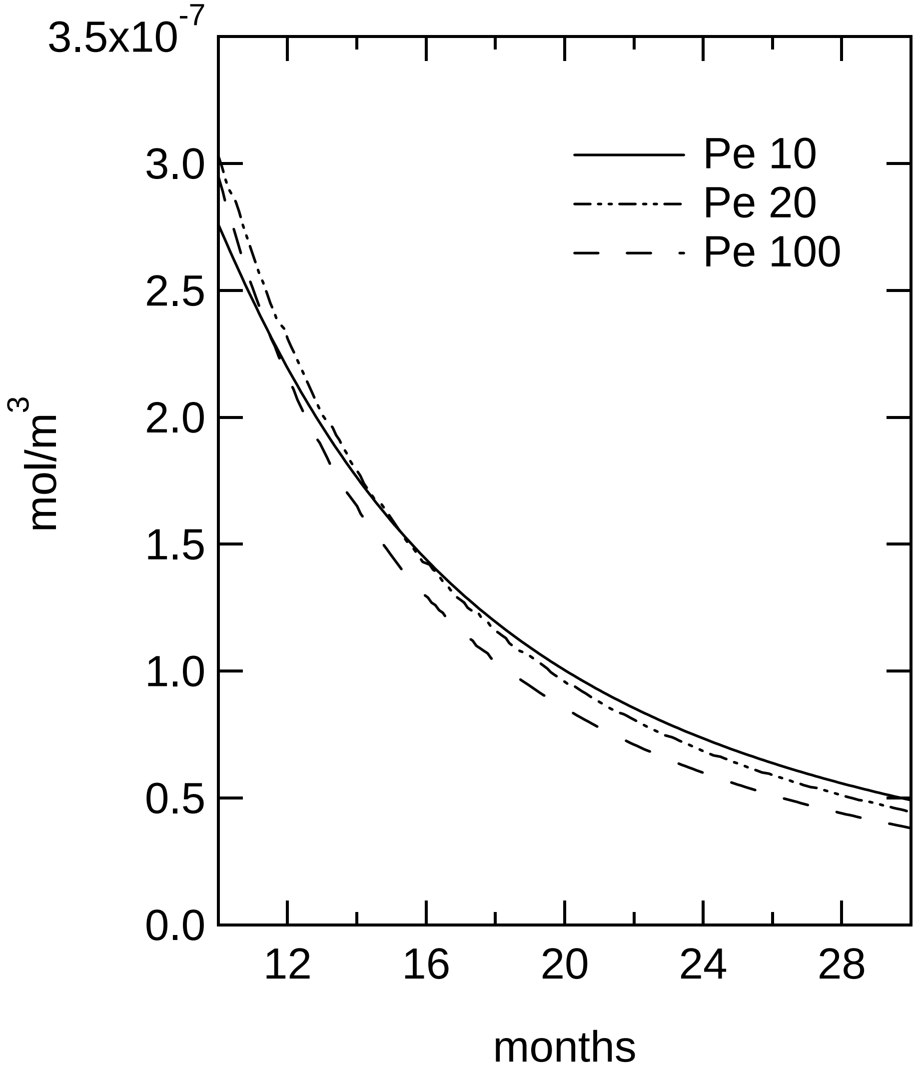

Figure 5.4: Tails of breakthrough curves for *Pe* values of 10, 20, and 100.

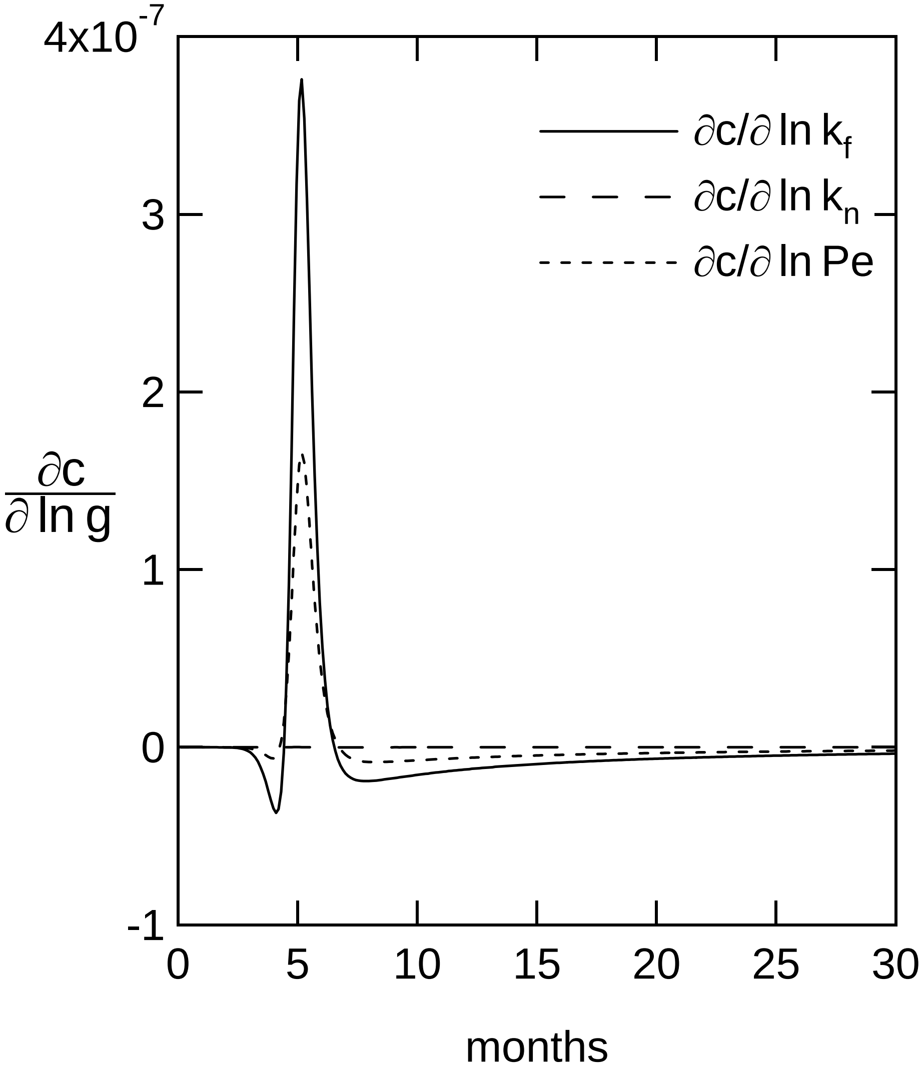

Figure 5.5: Sensitivity of the breakthrough curve with respect to k_n, k_f, and Pe at $Pe = 100$ where g represents any of the parameters of interest.

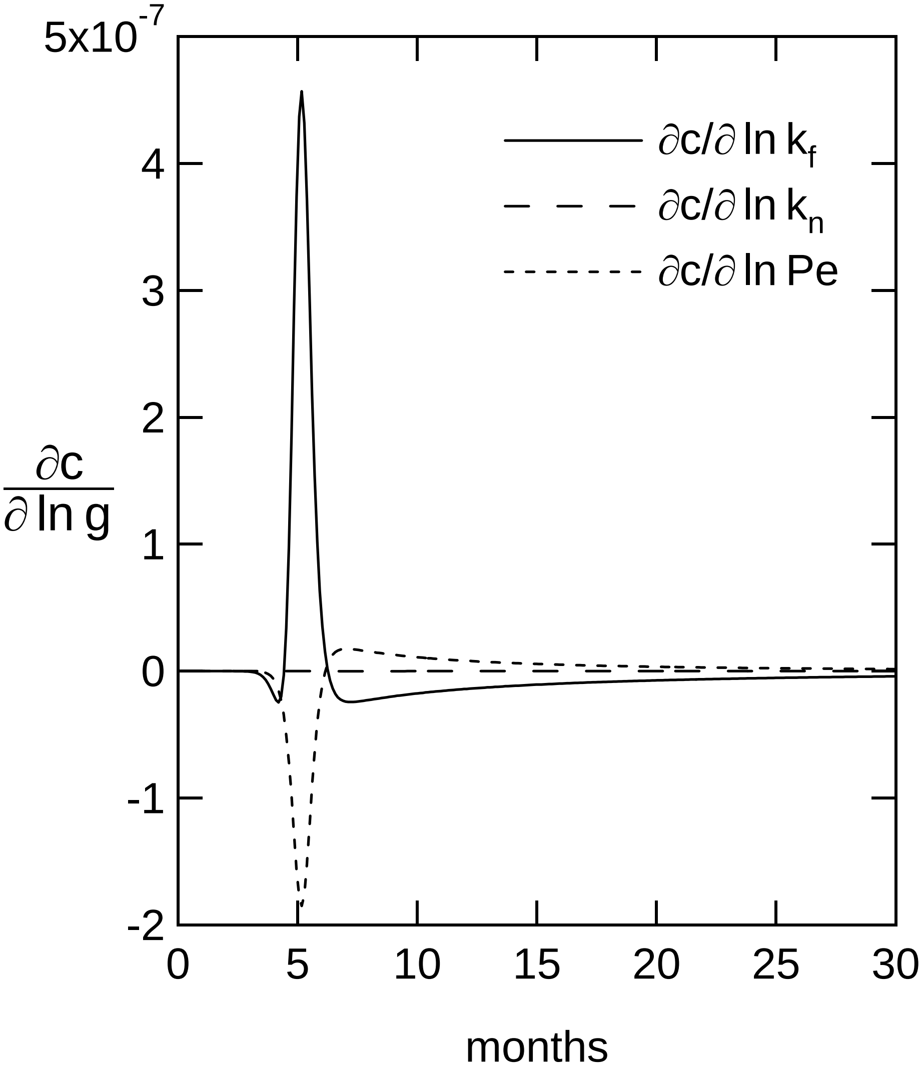

Figure 5.6: Sensitivity of the breakthrough curve with respect to k_n, k_f, and Pe at $Pe = 1000$ where g represents any of the parameters of interest.

essentially no effect on the shape of the breakthrough curve.

Sensitivities for Pe of 1000 are presented in Figure 5.6. For this large Pe value the external-film resistance acts as the controlling mass transfer mechanism. As before, k_n does not make any contribution to the model. In this example, the sensitivity data at different values of Pe required only one run of the process model at each value of Pe. Without using sensitivity variables, the simulation would have to be performed more than once at each value of Pe in order to gather the sensitivity data using finite differences.

The sensitivity data presented for this example illustrate quantitatively which transport resistances govern a pulse of hexane passed through a fixed bed of carbon at low concentrations. In cases where axial dispersion is important, Pe dominates. However, as dispersion effects are decreased, the fluid-phase resistance contributes more heavily to the breakthrough behavior. Furthermore, the sensitivity data illustrate that the inclusion of a linear driving force solid-phase resistance in the model is not necessary. This information demonstrates that in the case of a low-concentration pulse of a strongly adsorbed gas on BPL activated carbon, adsorption is controlled by the ability of the adsorbable component to move to the adsorption particle and not by its ability to diffuse through the pore structure of the material.

Nitrogen Adsorption on Carbon Molecular Sieve

In addition to a pulse of hexane on BPL activated carbon, a pulse of nitrogen in helium fed to a bed of carbon molecular sieve was also considered in order to determine the governing behavior of a pulse of a lightly adsorbed gas on a kinetically selective adsorbent. The model for the adsorption of nitrogen on carbon molecular sieve (CMS) was based on the same equation set, eqs. 5.1 through 5.6, used for the previous model. The adsorption parameters are listed in Table 5.1. The solid-phase

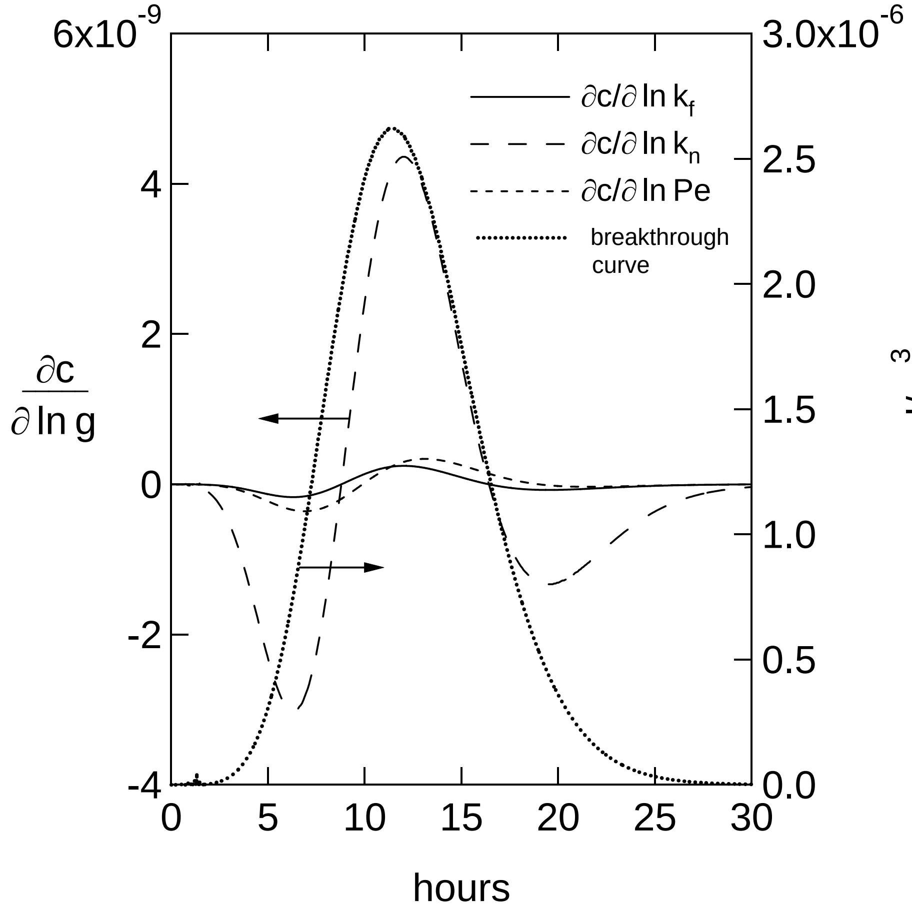

Figure 5.7: Breakthrough curve and corresponding sensitivities with respect to k_n, k_f, and Pe for nitrogen on CMS where g represents any of the parameters of interest.

diffusion parameter k_n is given by Wang *et al.*,[37] and other parameters were estimated with available correlations.

Figure 5.7 shows the breakthrough curve for this case along with the corresponding sensitivity data. This figure shows that for CMS the controlling transport parameter is the solid-phase linear driving force diffusion coefficient, which is expected given the constricted pores of CMS. Unlike the previous example, the sensitivity data show that none of the three transport parameters should be neglected, although the pulse is somewhat insensitive to the external-film resistance and Pe. Therefore, using only a solid-phase linear driving force transport model would be an accurate first approximation for this example. The previous example showed that low-concentration pulses are governed by external transport and dispersion limitations. However, in this example the adsorption of a low-concentration pulse of a light gas to a fixed bed of a kinetically selective adsorbent is not controlled by the ability of the adsorbate to diffuse to the adsorbent. The solid-phase diffusion resistance of this particular adsorbent is large enough to be dominant over all other transport mechanisms. Therefore, the sensitivity analysis predicts that, while the linear driving force diffusion coefficient was not important in the previous example for a low concentration pulse of strongly adsorbed species passed to activated carbon, the coefficient is important when the adsorbent material has a strong diffusion limitation such as the one found in carbon molecular sieves.

Adsorption of Nitrogen on BPL Activated Carbon

The previous examples only consider the effects of mass transport parameters; however, sensitivity plots can be obtained for any process variable. To explore the effects of both mass and energy transport parameters on the breakthrough of a pulse, the adsorption of nitrogen from helium on BPL activated carbon was examined. The parameters in the model were used as presented in the original work or were estimated

Table 5.2: System Parameters for Example 3

	Nitrogen Activated Carbon
T_{feed}	298 K
k_n	0.76 s^{-1}
h_a	0.525 kJ/(m^2s K)
M_{bwc}	0.96 kg
M_{fec}	0.48 kg
M_{pec}	0.96 kg
R_{ci}	0.0190 m
R_{co}	0.0215 m
L	0.24 m
R_p	5.0×10^4
ϵ'	0.7
λ	39.0 kJ/mol
ρ_b	460 kg/m^3
F_{feed}	98.0 SLPM
F_{prod}	49.0 SLPM
P_{feed}	405 kPa
P_{prod}	101 kPa
c_{pw}	0.46 kJ/(kg K)
c_{ps}	1.05 kJ/(kg K)
V_{in}	57.0 cm^3
V_{out}	109.0 cm^3

and are listed in Table 5.2.

The sensitivity of the breakthrough curve with respect to the energy parameters U_p, U_o, and U_e in eqs. 5.9 through 5.12 and the breakthrough curve are shown in Figure 5.8. The results show that the packed column heat transfer coefficient U_p has the greatest effect on the breakthrough curve. The sensitivity data show the energy transport from the column wall to the surroundings has no discernible effect on the pulse, and the energy transport in the end caps provides only a minor contribution.

Figure 5.9 shows that the effects seen in the sensitivity of the mole fraction to energy transport parameters are also seen in the outlet temperature. The sensitivity data of outlet temperature with respect to the energy parameters should mirror the mole fraction sensitivity data because, as the fluid-phase is adsorbed, energy is liberated and the temperature increases. Thus, the data show that increasing the packed column coefficient increases the heat transfer from the fluid to the column wall. This allows for more adsorption to take place, thereby decreasing the fluid-phase mole fraction and increasing the fluid-phase temperature.

Shown in Figure 5.10 is the sensitivity of the outlet temperature and fluid-phase mole fraction with respect to the fluid-solid heat transfer coefficient h_a. The results show that increasing h_a will increase the fluid-phase mole fraction. This occurs because increasing the coefficient allows more energy to be transferred to the solid-phase which in turn decreases the adsorption on the solid and increases the fluid-phase mole fraction.

The effect of k_n on the output mole fraction and the output temperature is seen in Figure 5.11, which shows unique behavior at the toe of the breakthrough curve. Without sensitivity analysis, the behavior is difficult to estimate because the mass and energy balances are coupled. It is also difficult to estimate which transport parameter is producing the unique breakthrough behavior without sensitivity analysis. However, a detailed understanding of the behavior of the toe of the curve is important for many industrial filtration applications where breakthrough, even at low concentrations, is unacceptable.

Figure 5.12 shows two regions in the toe of the breakthrough curve that have a negatively correlated relationship with k_n and two regions that show a positively correlated relationship with k_n. For clarity, the peaks with an inverse relationship to the breakthrough curve have been labeled 1 and 3, and the peaks that show a proportional relationship to the breakthrough curve have been labeled 2 and 4. To verify these results several breakthrough curves with varying k_n were examined.

The sensitivity analysis in Figure 5.12 shows that an increase in k_n will initially decrease the fluid-phase concentration at the leading edge of the breakthrough curve as seen by peak 1. Figure 5.13 illustrates how the breakthrough curve behavior changes when k_n is increased 25% at the very leading edge of the curve. As predicted by the sensitivity analysis, the fluid-phase concentration decreases for an increase in k_n.

Returning to the sensitivity analysis in Figure 5.12, an increase in k_n will slightly increase the fluid-phase concentration just after the leading edge of the breakthrough curve as seen by peak 2. This increase in k_n provides a very slight increase in the fluid-phase concentration at moderate times (e.g. 1.4 seconds), prior to the apex of the breakthrough curve. The slight increase is consistent with the small magnitude of peak 2. Examining peak 3 in Figure 5.12 shows that the apex of the breakthrough curve should decrease with an increase in k_n. Figure 5.14 shows the apex of the breakthrough curve for several different adjustments to k_n. A 25% increase in k_n reduces the apex of the breakthrough curve as predicted. The diminishing of the apex of the breakthrough curve is also seen for a two-fold increase in k_n.

The complex sensitivity data at the toe of the curve in Figure 5.11 is also seen in the sensitivity of the outlet mole fraction to the heat transfer coefficient h_a and packed column coefficient. Small fluctuations in the leading edge of these curves are the result of complex mass and energy balance effects. However, these complex behaviors are not as significant as the ones seen in Figure 5.11.

The impact of one parameter versus another on the breakthrough curve can easily be judged by examining the magnitudes of the sensitivity results for the parameters. Furthermore, the sensitivity data provide a quantitative criterion for determining when any process parameter can be neglected. For example, the sensitivity of the outlet temperature to the heat transfer coefficient h_a is nearly four orders of magnitude larger than the sensitivity of the fluid-phase mole fraction to this resistance. Therefore, a change in h_a will have a more profound effect on the outlet temperature than on the fluid-phase mole fraction. However, the sensitivity data for h_a is at least one order of magnitude lower than any of the other sensitivity data thus illustrating its limited importance in the simulation. Likewise, the packed column coefficient will have a stronger impact on the outlet mole fraction and temperature than will the heat transfer coefficient. Therefore the packed column coefficient should be estimated accurately as it more directly impacts system performance. However, the data also illustrate that the solid-phase mass transfer coefficient k_n must also be estimated accurately as it has the largest impact on the column output relative to all other parameters.

As seen in the previous example, the resulting changes in the breakthrough behavior for modest changes in the transport parameters is difficult to estimate without using sensitivity analysis. The character of most adsorption systems involves multiple process variables that are mutually dependent, such as mass and energy effects. Understanding how all the process variables are impacting a particular system requires detailed knowledge of each particular process. In this case, the simulation revealed that the adsorption of a light gas by activated carbon is governed by solid-phase diffusion and is significantly impacted by the energy balance. The breakthrough behavior of a pulse of a light gas to a carbon bed may seem intuitive, but the data reveal

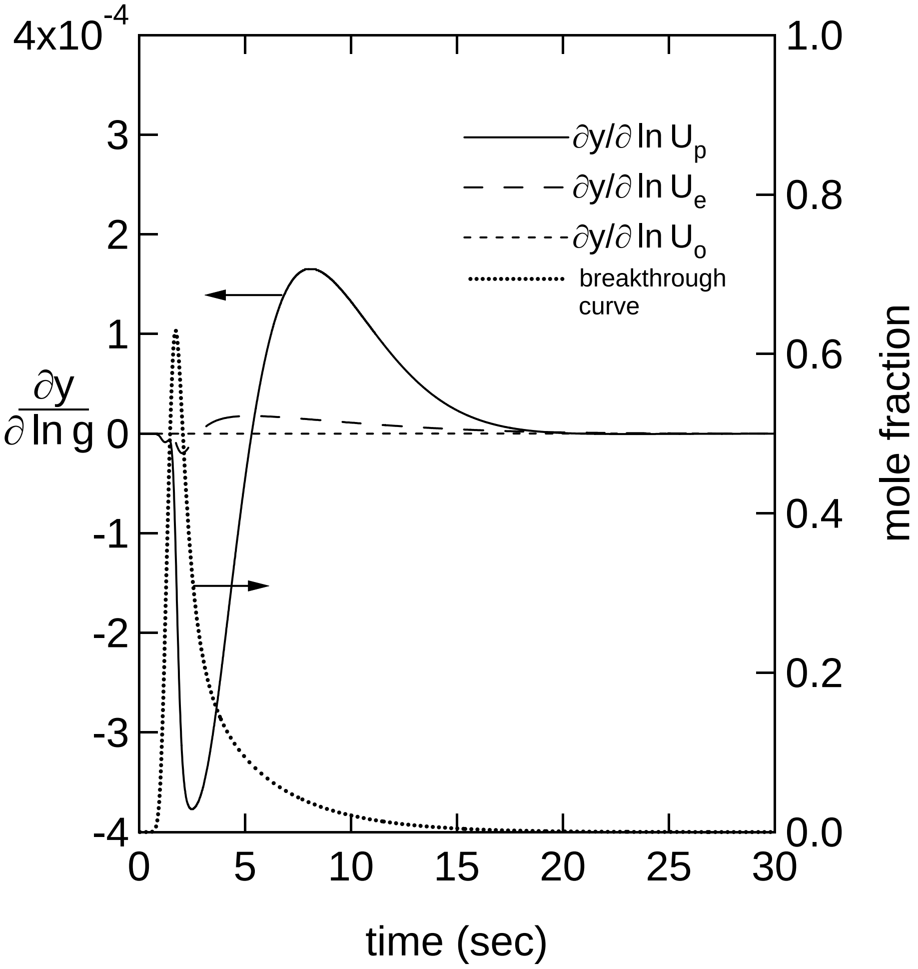

Figure 5.8: Breakthrough curve and corresponding sensitivities with respect to energy parameters where g represents any of the parameters of interest.

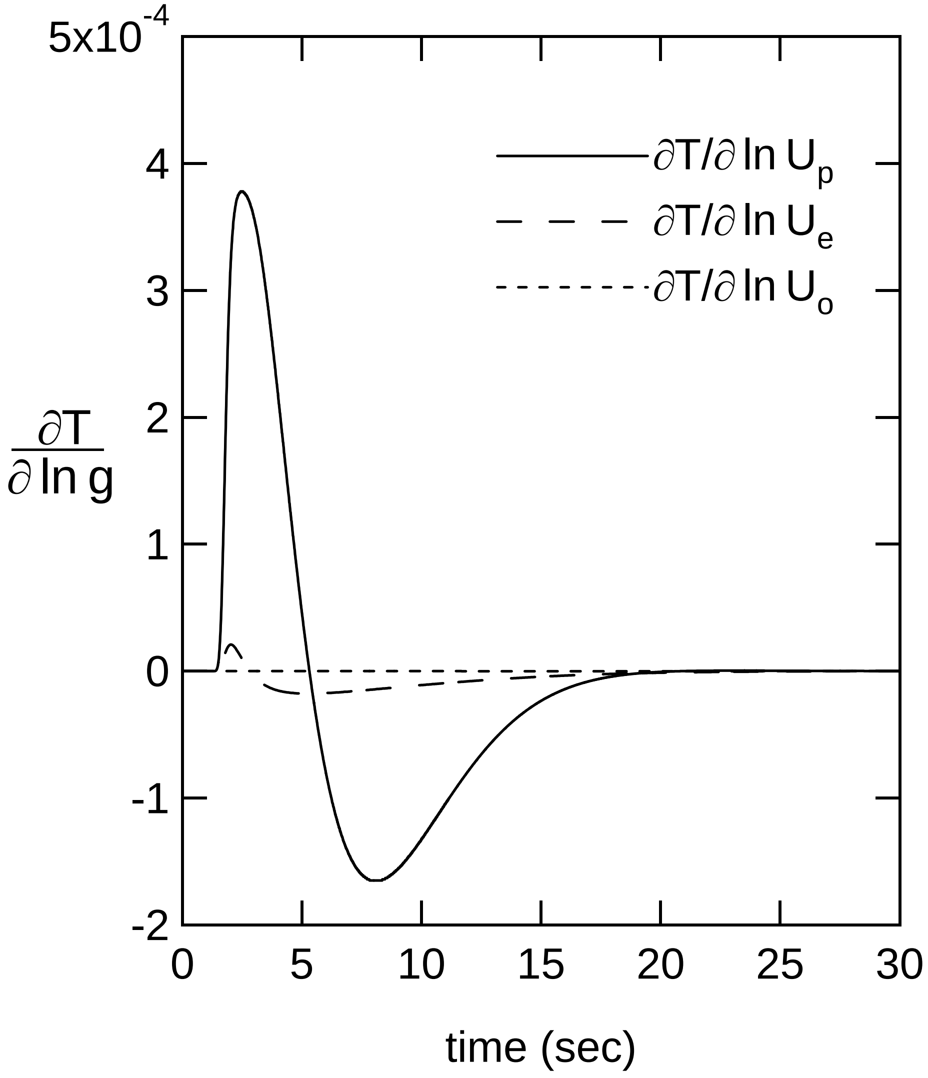

Figure 5.9: Sensitivity of the outlet temperature with respect to energy parameters where g represents any of the parameters of interest.

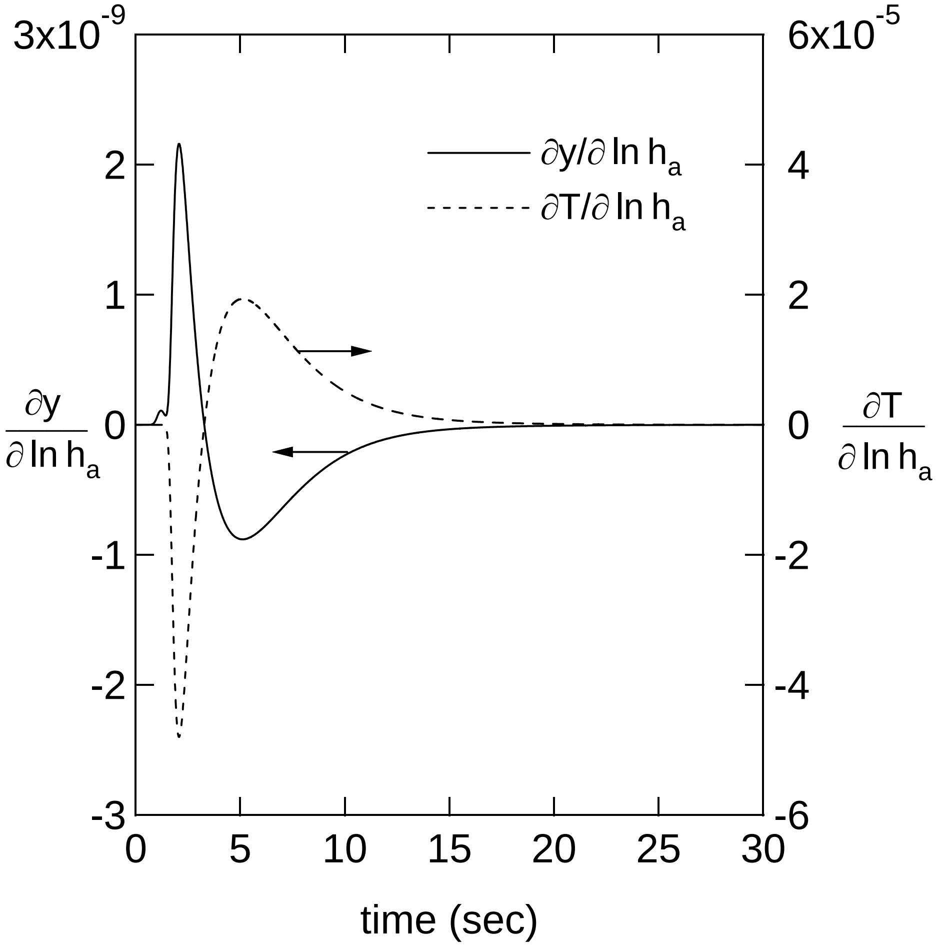

Figure 5.10: Sensitivity of the outlet mole fraction and temperature with respect to the fluid-solid heat transfer coefficient.

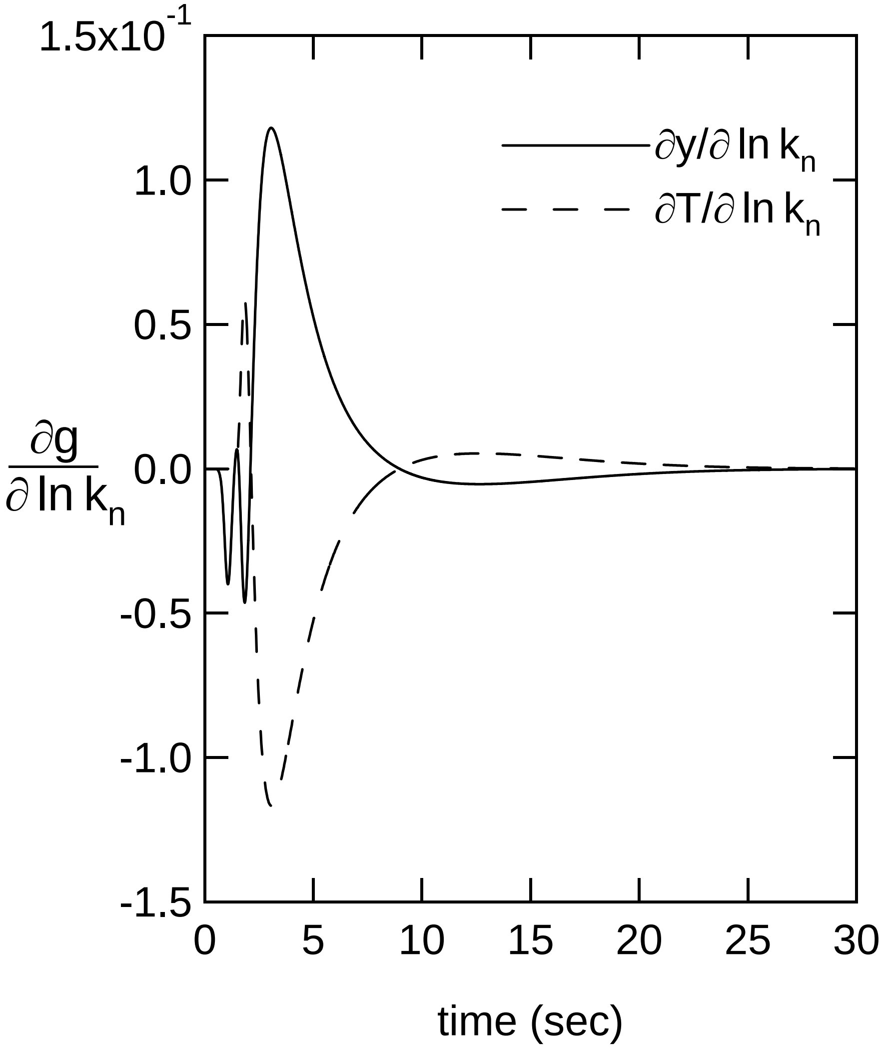

Figure 5.11: Effects of changes in k_n with respect to temperature and mole fraction where g represents any of the parameters of interest.

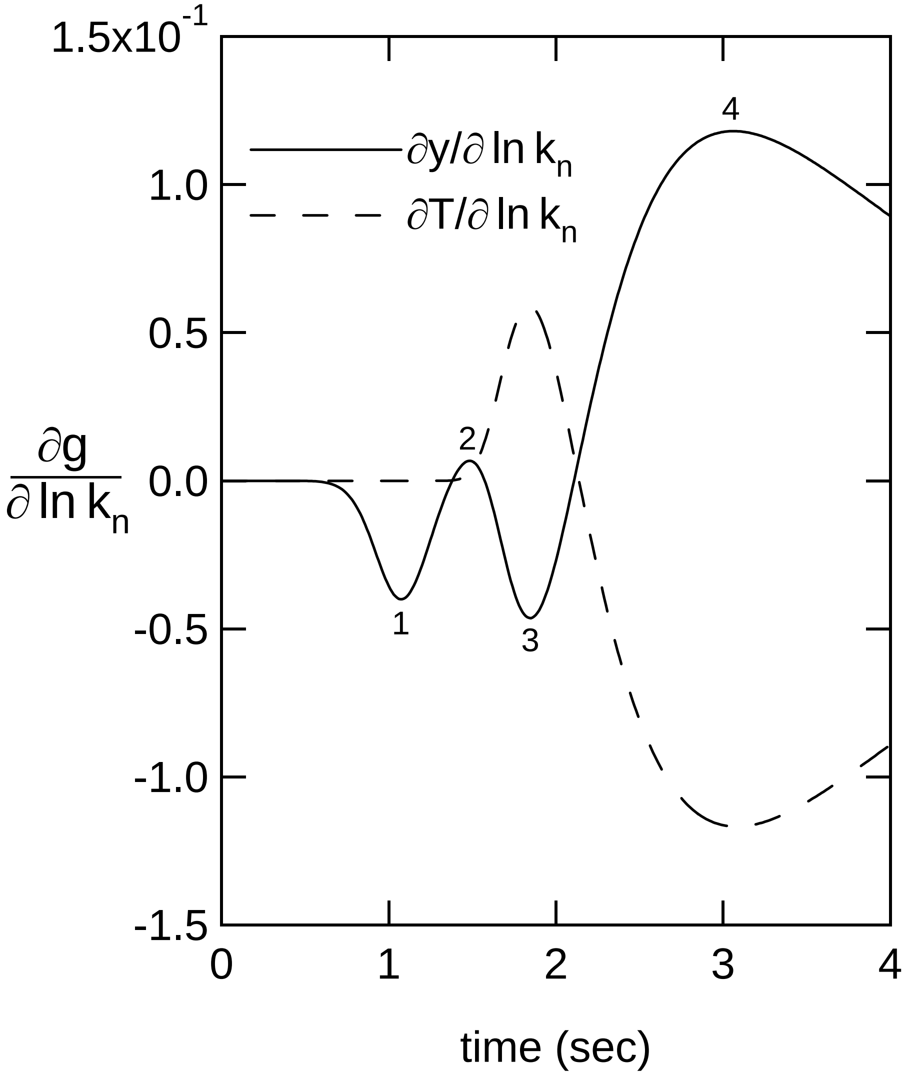

Figure 5.12: Detailed examination of changes k_n on the leading edge of the breakthrough curve. Peaks on the curve have been numbered for clarity.

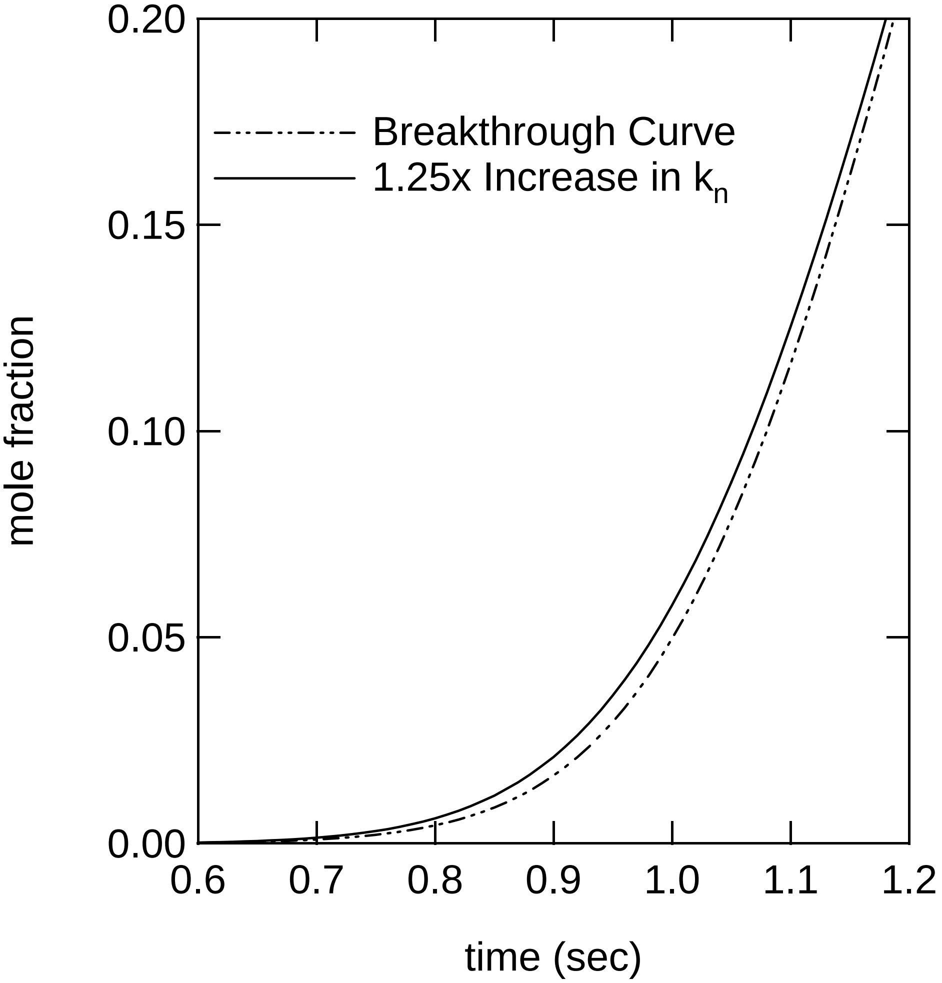

Figure 5.13: The effect of small changes in k_n on the leading edge of the breakthrough curve.

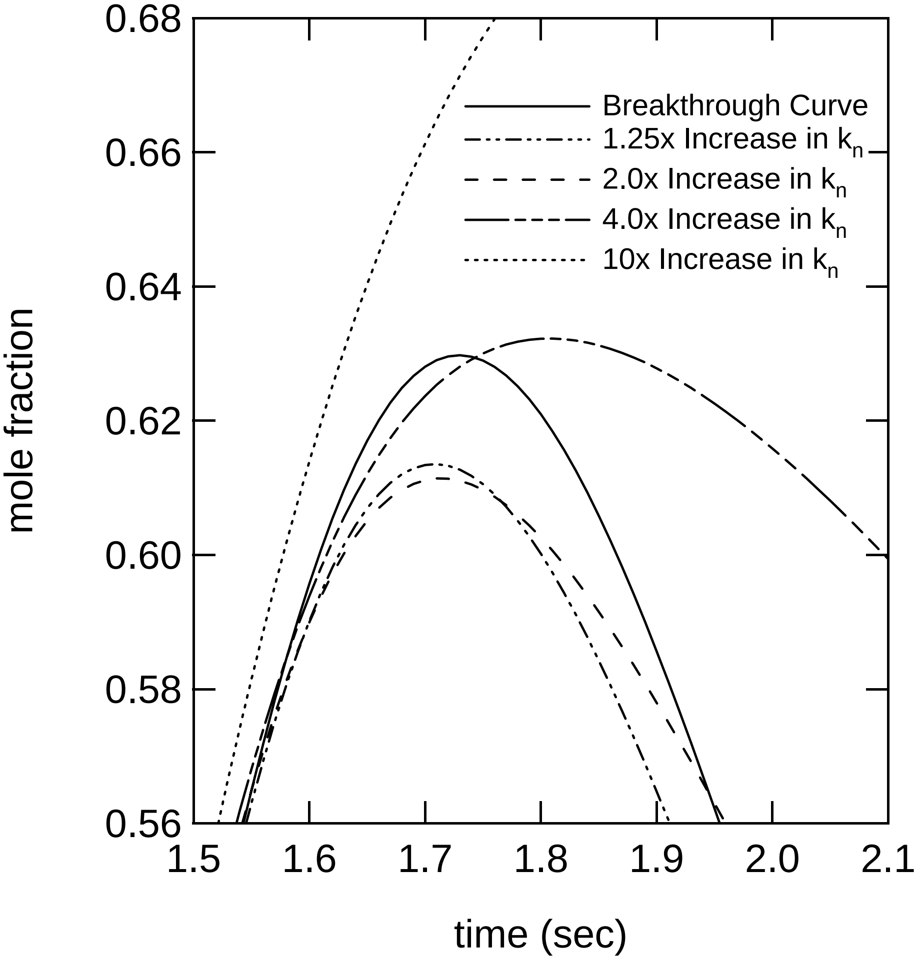

Figure 5.14: The effect of small changes in k_n on the apex of the breakthrough curve.

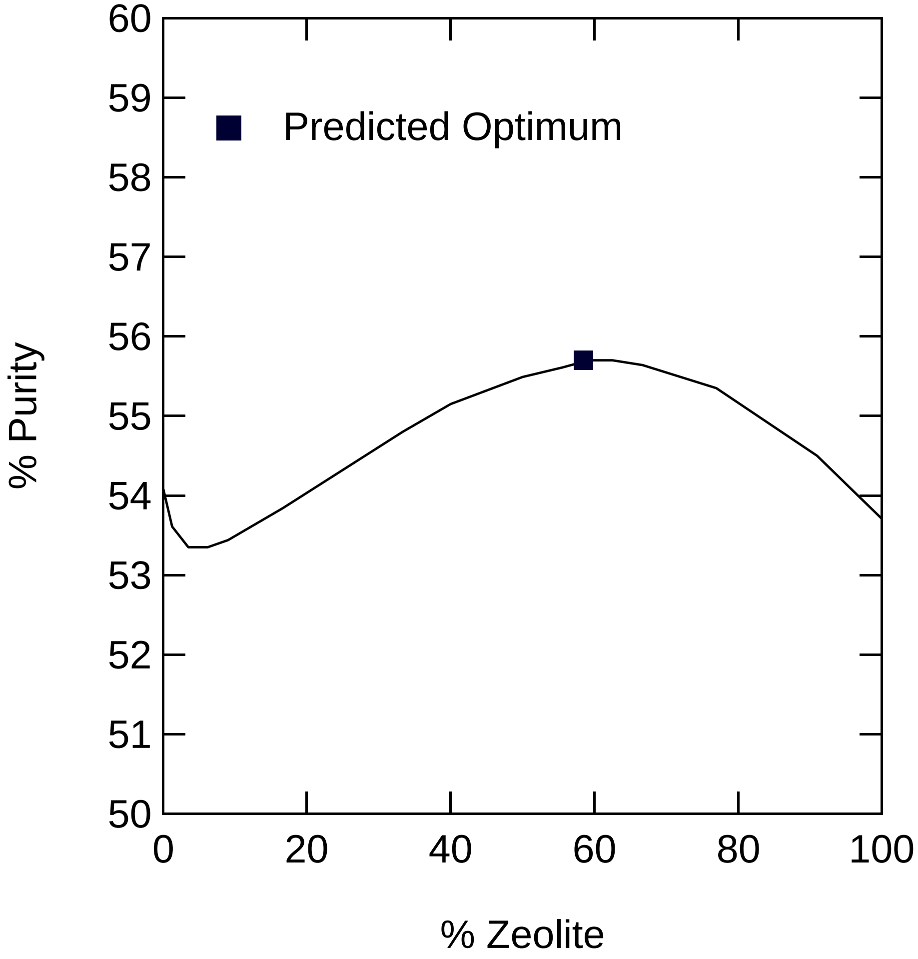

Figure 5.15: Optimum bed layering as predicted by the process model.

breakthrough behavior that is difficult to estimate.

Optimization of Layered Bed

With a detailed quantitative description of how key process parameters impact system performance, system optimizations can easily be performed. Sensitivity calculations determine derivatives of the variables defined by differential equations with respect to a particular process variable of interest, i.e., $\partial x/\partial g$ where x is any variable defined by differential equations and g is a process variable. These sensitivities are well suited for a maximum or minimum optimization routine. Defining an objective function such as objective $= f(x, g)$ allows for the optimization of an objective function of x with respect to any process variable g. Using a Newton or quasi-Newton routine such as Hybrid1[15] along with the sensitivity data from ODESSA allows for the optimum of the system to be determined.

To optimize the layering of an adsorption bed, we have developed a PSA model based on the work of Cavenati[2–6] to upgrade the purity of methane contained in a stream of carbon dioxide and nitrogen. They present a Skarstrom cycle that uses a layered adsorption bed comprised of a CMS and 13X zeolite. The purpose of the zeolite is to remove the carbon dioxide and allow the methane and nitrogen to pass through to the CMS. The CMS then kinetically separates the nitrogen and methane. They show that not only is it possible to upgrade the feed stream, but that it is also possible to obtain an optimum purity by adjusting the ratio of the adsorbent layers.

The model of Mahle *et al.*[25] was applied to a system similar to the one examined by Cavenati et al. The PSA model uses a Skarstrom cycle and two adsorption beds. The system is non-isothermal and the mass transport resistances are modeled using the solid-phase linear driving force. The diffusion parameters for the zeolite were estimated using the correlation of Sladek *et al.*,[33] while those for the CMS were taken as presented in the work of Wang *et al.*[36] The system parameters are outlined in Table 5.3 and 5.4. A purity was defined as

$$\text{Purity} = \frac{\int_0^{t_{feed}} c_{CH_4} v dt}{\int_0^{t_{feed}} c_{CH_4} v dt + \int_0^{t_{feed}} c_{CO_2} v dt + \int_0^{t_{feed}} c_{N_2} v dt} \tag{5.22}$$

and was calculated at the bed outlet. The objective of the program was to maximize the purity with respect to the percent of zeolite contained in the column.

The program was run until a periodic state was virtually reached. Then, the purity was evaluated at the bed outlet and the objective function was calculated. Using the objective function, a new bed configuration was estimated and the process repeated until the objective function was essentially zero.

A key benefit of calculating sensitivities simultaneously during the process run is that the sensitivity calculations do not have to be performed prior to the cycle of interest. The program can be run to a periodic state without spending time computing sensitivities. In addition, by using the sensitivities to complete a direct optimization, the time required to reach the periodic state for each new bed configuration could be reduced. Thus, the application of sensitivities to optimize a system in relation to process parameters is complementary to the direct optimization schemes.

The sensitivity data were gathered at a periodic state on the last process cycle. The program calculated the sensitivities using output from the previous cycle as its initial condition. Thus, the program used ODESSA to evaluate how the output of the last cycle would change if the bed layering were adjusted prior to that cycle. For computational efficiency, the sensitivity data were not calculated by selecting a bed layering scenario, running to a periodic state, followed by selecting a new bed layering scenario, running to a new periodic state, and calculating the derivative between the two periodic states.

The results of optimizing the system with respect to the percentage of zeolite contained in the bed are presented in Figure 5.15. The data show that the purity of the product is a function of the bed layering. The maximum of the parabola is predicted at 58.48% zeolite and a product purity of 55.70%. This particular bed configuration was selected by the program as the ideal layering by using a Newton method to drive the objective for purity to a maximum. The small difference between the predicted maximum and the actual maximum of the purity curve is within the tolerances of the program. Specifically, the difference between the predicated and actual maximum is 0.008% in purity.

The application of this type of optimization scheme is not limited to two bed layers, but rather can be extended to optimize columns containing multiple layers. Furthermore, bed layering is just one example among many that could have been selected for optimization. Examples of interest could include optimization with respect to regeneration temperature, purge pressure, column diameter, or particle radius. The objective function could also be changed and optimization routines performed on product recovery or other performance measures.

5.4 Conclusion

The application of sensitivity calculations with respect to process variables allows for a quantitative determination of how process variables govern performance. In the case of a low-concentration pulse of hexane to an activated carbon bed, the sensitivity analysis predicts the importance of Pe and the external-film resistance in the modeling of the mass transfer. The results provide a quantifiable reason to neglect the solid-phase mass transfer coefficient. Furthermore, by gathering a range of sensitivity data it is possible to quantitatively examine the changing importance of the three transport parameters of interest.

In the second example detailing the adsorption of nitrogen on CMS, the sensitivity data reflect the importance of a solid-phase linear driving force coefficient. This case shows that both Pe and the external-film resistance also contribute to the model but that as a first approximation modeling could be performed considering only the solid-phase resistance.

When the sensitivity calculations are performed on a system with both mass and energy effects, as seen in the adsorption of nitrogen on BPL, it is possible to demonstrate quantitatively that the mass transport effects have a greater impact on the system than to the energy transport effects. More importantly, this example shows how simultaneously calculated sensitivity data can accurately predict non-intuitive behavior and eliminate the need of estimating how one particular variable impacts the adsorption process. In this example, unique and unexpected breakthrough behavior occurs at the toe of the breakthrough curve as a result of coupled mass and energy transfer. The impact of subtle changes in key parameters on this non-intuitive behavior is accurately described by the sensitivity data.

The use of sensitivities can be readily applied to a variety of process variables and objective functions and is complimentary to direct optimization schemes. Sensitivity data were applied to determine the optimal layering of an adsorption bed, which is an important industrial problem that has received limited attention in the literature. In this case, the sensitivity calculations accurately predicted the optimum layering of the adsorption bed for recovery of methane from a process stream. The example presented illustrates one of many potential optimization schemes that could be performed using this type of data.

Table 5.3: System Input Parameters for PSA Cycle

Column Properties	
V_{in}	57.0 cm^3
V_{out}	109.0 cm^3
V_{bed}	160.8 cm^3
U_{packed}	0.093 kJ/(m^2 s K)
U_{empty}	0.009 kJ/(m^2 s K)
M_{bwc}	0.96 kg
M_{fec}	0.48 kg
M_{pec}	0.96 kg
R_{ci}	0.008 m
R_{co}	0.0107 m
L	0.80 m
c_{pw}	0.460 kJ/(kg K)
T_{amb}	323 K
P_{high}	250 kPa
P_{low}	6 kPa
P_{purge}	3 kPa
F_{feed}	1.02 SLPM
F_{prod}	0.25 SLPM
t_c	500 s

Table 5.4: System Parameters for PSA Layers

	Layer 1: 13X Zeolite	Layer 2: CMS
R_p	0.80×10^{-3} m	0.90×10^{-3} m
ρ_b	1130 kg/m^3	880.0 kg/m^3
$\epsilon^{'}$	0.54	0.46
c_{ps}	0.920 kJ/kg K	0.880 kJ/kg K
k_{CH4}	4.25 s^{-1}	2.7×10^{-5} s^{-1}
k_{N2}	4.22 s^{-1}	5.4×10^{-4} s^{-1}
k_{CO2}	6.12×10^{-3} s^{-1}	8.7×10^{-3} s^{-1}
λ_{CH4}	15.675 kJ/mol	38.947 kJ/mol
λ_{N2}	15.716 kJ/mol	15.930 kJ/mol
λ_{CO2}	54.729 kJ/mol	33.674 kJ/mol

References

[1] Biegler L.T., Jiang L., Fox V.G., (2004). Recent Advances in Simulation and Optimal Design of Pressure Swing Adsorption Systems. Sep. Purif. Reviews, 33, 1-39.

[2] Cavenati S., Grande C.A., Rodrigues A. E., (2004). Adsorption Equilibrium of Methane, Carbon Dioxide, and Nitrogen on Zeolite 13X at High Pressures. J. Chem. Eng. Data, 49, 1095-1101.

[3] Cavenati S., Grande C.A., Rodrigues A. E., (2005a). Separation of Methane and Nitrogen by Adsorption on Carbon Molecular Sieve. Sep. Sci. and Tech., 40, 2721-2743.

[4] Cavenati S., Grande C.A., Rodrigues A. E., (2005b). Layered Pressure Swing Adsorption for Methane Recovery from $CH_4/CO_2/N_2$ Streams. Adsorption, 11, 549-554.

[5] Cavenati S., Grande C.A., Rodrigues A. E., (2005c). Upgrade of Methane from Landfill Gas by Pressure Swing Adsorption. Energy and Fuels, 19, 2545-2555.

[6] Cavenati S., Grande C.A., and Rodrigues A.E., (2006). Separation of $CH_4/CO_2/N_2$ mixtures by layered pressure swing adsorption for upgrade of natural gas. Ind. Eng. Chem. Res., 61, 3893-3906.

[7] Chahbani M.H., Tondeur D., (2000). Mass Transfer Kinetics in Pressure Swing Adsorption. Sep. Purif. Technol., 20, 185-196.

[8] Chlendi M., Tondeur D., Rolland F., (1995). A Method to Obtain a Compact Representation of Process Performances from a Numerical Simulator: Example of Pressure Swing Adsorption for Pure Hydrogen Production. Gas Sep. Purif., 9, 125-135.

[9] Croft D.T., LeVan M.D., (1994a). Periodic States of Adsorption Cycles-I. Direct determination and Stability. Chem. Eng. Sci., 49, 1821-1829.

[10] Croft D.T., LeVan M.D., (1994b). Periodic States of Adsorption Cycles-II. Solution Spaces and Multiplicity. Chem. Eng. Sci., 49, 1831-1841.

[11] Crus P., Santos J.C., Magalhaes F.D., Mendes A., (2003). Cyclic Adsorption Separation Processes: Analysis Strategy and Optimization Procedure. Chem. Eng. Sci., 58, 3143-3158.

[12] Davis M.M. and LeVan M.D., (1989). Experiments on Optimization of Thermal Swing Adsorption. Ind. Eng. Chem. Res., 28, 778-785.

[13] Ding Y., LeVan M.D., (2001). Periodic States of Adsorption Cycles III. Convergence Acceleration for Direct Determination. Chem. Eng. Sci., 56, 5217-5230.

[14] Ding Y., Croft D.T., LeVan M.D.,(2002). Periodic States of Adsorption Cycles IV. Direct Optimization. Chem. Eng. Sci., 57, 4521-4531.

[15] Garbow B.S., Hillstrom K.E., More J.J., and Sorenson D.C., (1980). The MINIPACK Project Argonne National Laboratory.

[16] Glueckauf E., (1947). Theory of Chromatography. PartII. Chromatograms of a Single Solute. J. Chem. Soc., 1302-1308.

[17] Hartzog D.G., Sircar S., (1995). Sensitivity of PSA Process Performance to Input Variables. Adsorption, 1, 133-151.

[18] Jiang L., Biegler L.T., Fox V.G., (2003). Simulation and Optimization of Pressure-Swing Adsorption Systems for Air Separation. AIChE J., 49, 1140-1157.

[19] Jiang L., Fox V.G., Biegler L.T., (2004). Simulation and Optimal Design of Multiple-Bed Pressure Swing Adsorption Systems. AIChE J., 50, 2904-2917.

[20] Kumar R., (1994). Pressure Swing Adsorption Process: Performance Optimum and Adsorbent Selection. Ind. Eng. Chem. Res., 33, 1600-1605.

[21] Leis J.R., Kramer M.A., (1988). The Simultaneous Solution and Sensitivity Analysis of Systems Described by Ordinary Differential Equations. ACM Trans. Math. Soft., 14, 61-67.

[22] LeVan, M.D., Carta,G., Yon, C. M., (1997). Section 16: Adsorption and Ion Exchange, in: Green, D.W. & Maloney, J.O. (Eds.), Perry's Chemical Engineers' Handbook, 7th ed.; McGraw-Hill: New York.

[23] Li S., Petzold L., (1999). Design of New DSAPK for Sensitivity Analysis. Technical Report, Dept. of Computer Science, Technical Report UCSB.

[24] Li S., Petzold L., (2000). Software and Algorithms for Sensitivity Analysis of Large-Scale Differential-Algebraic Systems. J. Comp. Appl. Math., 125, 131-145.

[25] Mahle J.J., Friday D.K., and LeVan M.D., (1996). Pressure Swing Adsorption for Air Purification. 1. Temperature Cycling and Role of Weakly Adsorbed Carrier Gas. Ind. Eng. Chem. Res., 35, 2342-2354.

[26] Malek A., Farooq S., (1998). Hydrogen Purification from Refinery Fuel Gas by Pressure Swing Adsorption. AIChE J., 44, 1985.

[27] Mendes A.M.M., Costa C.A.V., Rodrigues A.E., (2000). Analysis of Nonisobaric Steps in Nonlinear Bicomponent Pressure Swing Adsorption Systems. Application to Air Separation. Ind. Eng. Chem. Res., 39, 138-145.

[28] Mendes A.M.M., Costa C.A.V., Rodrigues A.E., (2001). Oxygen Separation from Air by PSA: Modeling and Experimental Results Part I: Isothermal Operation. Sep. Purif. Technol., 24, 173-188.

[29] Qi N., LeVan M.D., (2005). Virial Excess mixing Coefficient Corrections for the Adsorbed Solution Theory. Ind. Eng. Chem. Res., 44, 3726-3732.

[30] Shim W.G., Lee J.W., Moon H., (2003). Equilibrium and Fixed-Bed Adsorption of n-Hexane on Activated Carbon. Sep. Sci. Technol., 38, 3905-3926.

[31] Sircar S., Kumar R., Anselmo K.J., (1983). Effects of Column Nonisothermality or Nonadiabticity on the Adsorption Breakthrough Curves. Ind. Eng. Chem. Process Des. Dev., 22, 10-15.

[32] Sircar S., (2005). Influence of Gas-Solid Heat Transfer on Rapid PSA. Adsorption, 11, 509-513.

[33] Sladek K.J., Gilliland E.R., and Baddour F.R., (1974). Diffusion of Surfaces. II. Correlation of Diffusivities of Physically and Chemically Adsorbed Species. Ind. Eng. Chem. Fundam., 13, 100-105.

[34] Waldron W.E., Sircar S., (2000). Parametric Study of a Pressure Swing Adsorption Process. Adsorption, 6, 179-188.

[35] Walton K.S., LeVan M.D., (2005). Effect of Energy Balance Approximations on Simulation of Fixed-Bed Adsorption. Ind. Eng. Che. Res., 44, 7474-7480.

[36] Wang, Y., LeVan M.D., (2007). Mixture Diffusion in Nanoporous Adsorbents: Development of Fickian Flux Relationship and Concentration-Swing Frequency Response Method. Industrial and Engineering Chemistry Research 46, 2141-2154.

[37] Wang Y., Sward B.K., and LeVan M.D., (2003). New Frequency Response Method for Measuring Adsorption Rates via Pressure Modulation: Application to Oxygen and Nitrogen in a Carbon Molecular Sieve. Ind. Eng. Chem. Res., 42, 4213-4222.

Notation

c = fluid-phase concentration, mol/m^3

c^* = fluid-phase concentration at particle surface, mol/m^3

c_{pw} = heat capacity of column wall, kJ/(kg K)

c_{ps} = heat capacity of adsorbent, kJ/(kg K)

c_{pf} = heat capacity of fluid phase, kJ/(kg K)

F_{feed} = feed flow rate, SLPM

F_{prod} = product flow rate, SLPM

g = parameter of interest

h_a = fluid-solid film heat transfer coefficient

h_f = fluid-phase enthalpy, kJ/mol

k_f = external film mass transfer coefficient, m/s

k_n = Glueckauf linear driving force coefficient, s^{-1}

L = bed length, m

M_{bwc} = mass bed wall center, kg

M_{fec} = mass feed end cap, kg

M_{pec} = mass product end cap, kg

m_w = mass of column wall, kg

n = adsorbed-phase concentration, mol/kg

n^* = solid-phase concentration at particle surface, mol/kg

Pe = Peclet number, $Pe = v^{ref}L/D$

P_{high} = adsorption pressure, kPa

P_{low} = desorption pressure, kPa

P_{purge} = blow down pressure, kPa

P_{prod} = product pressure, kPa

P_{feed} = feed pressure, kPa

R_p = particle radius, m

R_{ci} = inner column radius, m

R_{co} = outer column radius, m

T = temperature, K

T_{ref} = reference temperature, K

T_{amb} = ambient temperature, K

T_w = temperature of column wall, K

t = time, s

t_c = cycle time, s

t_p = duration of pulse, s

U_e = heat transfer coefficient empty parts of column, kJ/(m s K)

U_o = heat transfer coefficient to surroundings, kJ/(m s K)

U_p = heat transfer coefficient packed column, kJ/(m s K)

u_f = internal energy fluid-phase, J/mol

u_s = internal energy solid-phase, J/kg

v = interstitial velocity, m/s

V_{in} = inlet endcap volume, m^3

V_{out} = outlet endcap volume, m^3

V_{bed} = packed column volume, m^3

z = axial column length variable, m

Greek Letters

ϵ = void fraction of packing

ϵ' = total bed voidage (inside and outside particles)

λ = heat of adsorption, J/mol

ρ_b = bulk density kg/m^3

τ = dimensionless bed volumes

τ_o = dimensionless bed volumes of feed

ζ = dimensionless axial bed length variable

CHAPTER VI

CONCLUSIONS AND RECOMMENDATIONS

6.1 Conclusions

The first segment of the research found in chapters II and III details the development of a novel carbonaceous adsorbent material. The key results from chapter II are:

- A novel nanoporous carbon-silica composite material has been synthesized. The material has a high surface area (850 m^2/g), long range order, and a 5 Å pore size when measured via the Horvath-Kawazoe method.
- The material is unique when compared to traditional activated carbons because the material is derived via a templating technique and is not physically or chemically activated.
- CSC utilizes MCM-41 as a template to adsorb furfuryl alcohol that is then carbonized at high temperature.
- Carbon comprises approximately 40 wt% of CSC.
- CSC has a higher adsorption capacity for light hydrocarbons than nitrogen and carbon dioxide, which illustrates that the surface of the composite is carbonaceous.
- The adsorption properties of the novel material are consistent with the adsorption properties of carbogenic molecular sieves, which are also derived from furfuryl alcohol.
- The mesoporous channels of MCM-41 act in a similar fashion to mesopores formed in PEG modified PFA carbons.

- When the surface area of the material is examined on a per carbon basis the area of the material is approximately 2300 m^2/g.

The second portion of this work detailed the sensitivity of our novel CSC material to synthesis conditions. Several materials were produced under a variety of conditions and were extensively characterized. Key results from this chapter III are:

- CSC materials were synthesized using benzene, toluene, or methanol as the furfuryl alcohol solvent. Materials were also produced in which the carbonization sequence was performed at 5 atm, 1 atm, or under a vacuum.
- All of the materials are completely nanoporous, have high surface areas (650 m^2/g), long range order, and narrow pore size distributions centered near 12 Å when modeled using DFT.
- The HK model shows these materials all contain exclusively a 5 Å pore.
- Preparing the material under 5 atm of pressure significantly inhibited the development of both the surface area and porosity of the material.
- The material prepared under vacuum showed an increase in surface area relative to the materials prepared under pressure.
- A CSC material that utilized silica gel instead of MCM-41 was also synthesized and showed an increase in surface area relative to the parent silica gel.
- The pore size of the silica gel based CSC material as determined by DFT was centered near 12 Å but also contained some mesoporosity spanning from 30 to 130 Å. The mesoporosity in the sample was centered near 67 Å and is the result of partially filling of the large (>100 Å) silica gel mesopores.
- All of the materials contained approximately 35 wt% carbon. The material prepared under vacuum showed the least amount of carbon loading (33 wt%),

and the material carbonized at 5 atm and the CSC-Si control material showed the greatest carbon loading (42 wt%).

- The alpha plots for these materials all show nanoporous filling.
- All the materials readily adsorb ethane, but the material prepared under pressure showed the least amount of ethane adsorption.
- The results illustrate that it is possible to utilize synthesis conditions to control the physical characteristics of this material.

This work also detailed the application of concentration-swing frequency response to characterize mass transport phenomena in single adsorbent particles as discussed in chapter IV The key results from this work are:

- The adsorption kinetics of water adsorption in BPL activated carbon are best described by a surface diffusion model. The results show a clear minimum in the diffusivity accruing at approximately 0.5 P/P_o. The Darken relationship predicts the variation of diffusivity with loading only qualitatively.
- Previous studies assumed the LDF model adequately described the diffusion behavior of water in BPL activated carbon; however, these results show that nanopore diffusion is the appropriate model to describe the transport behavior.
- Both the nanopore diffusion and LDF models can be used to describe the diffusion of hexane in BPL activated carbon.
- The diffusion of water in Davison Grade 40 silica gel is best characterized by the LDF model.

The last segment of the work discussed the sensitivity of pulse inputs to fixed bed filters. The key results in this section include:

- The transport behavior for the adsorption of a low concentration pulse of hexane in BPL activated carbon the transport behavior is governed by the external film mass transfer resistance. Axial dispersion plays a more limited role in the adsorption of a pulse input, and the solid-phase linear driving force does not have an appreciable effect on the pulse output. It should be noted that this conclusion holds for the concentration range studied. It is reasonable that as the concentration in the fluid-phase is increased the surface of the adsorbent particle becomes saturated and the solid-phase driving force plays a more important role.

- The adsorption of nitrogen in CMS is impacted by the external film mass transfer resistance, the solid-phase mass transfer resistance, as well as axial dispersion. However, the effects of the solid-phase mass transfer resistance and axial dispersion are more limited relative to the external film resistance.

- Mass and energy effects are considered for the adsorption of nitrogen in BPL activated carbon. The results show that mass transfer resistances control the breakthrough of the pulse. Of the energy parameters considered, the packed column heat transfer coefficient has the greatest effect on both the outlet mole fraction and temperature.

- The sensitivity information is directly applied to optimize a layered bed with respect to product purity.

6.2 Recommendations

Nearly all aspects of this work have the potential to be extended. This material could easily be adapted to perform chemisorption by incorporating metals into the structure at particular locations. The metals that are commonly used in catalytically activate carbons, such as ASZM-TEDA, include copper, molybdenium, silver, and zinc, all of which can be controllably placed at specific location in CSC materials.

For example, metals can be placed inside the walls of the MCM-41 framework by including metals during the hydrothermal synthesis of the framework and can also be washed onto the surface of the MCM-41 framework prior to impregnation. These methods allow for the placement of metals in the walls as well as on the surface of MCM-41. Metals salts can also be placed in furfuryl alcohol to allow the metals to be evenly distributed in the carbon lining of CSC materials. Once carbonized, metals can also be washed onto the surface of the carbon-silica composite structure. The controlled placement of active metal sites in an adsorbent carbon would provide a significant advance in adsorption technology over current activated carbons, which incorporate metals into the carbon surface randomly.

The CSC material could be further modified by adding thermally degrading polymers into the PFA solution during impregnation. Polymers of varying molecular weights that degrade without leaving a residue could be used to increase the surface area of these materials. Because the materials are not activated via carbonization under pressure or vacuum, adding a thermally degrading polymer to the synthesis may activate the material.

Also, the sensitivity of these materials to the amount of alumina used to activate the adsorption of furfuryl alcohol in the pores of the material should be investigated. It may be possible to vary the carbon loading and adsorption properties of these materials by altering the ratio of alumina to silica. Using less alumina should decrease the carbon loading of the material and prevent complete pore filling, which may increase the surface area of the material by increasing the liberation of gaseous by-products generated during carbonization.

In regards to the CSFR studies, a wide variety of materials could be characterized to better understand their mass transport properties. The kinetics of the co-adsorption of multiple adsorbates, such as water and organics on activated carbon, has received only limited attention in the research literature. Furthermore, this system is well suited to examine the kinetics of novel materials.

Finally, the mathematical model presented can be readily adapted to model and optimize a wide variety of process situations. Optimization could be readily performed on multilayered beds, regeneration temperature, purge pressure, column diameter, or particle radius. Also, sensitivity analysis could be used to explore complex multi-component adsorption systems.